University of Southampton

Faculty of Engineering and Physical Sciences

Electronics and Computer Science

Optical Vortices and their Related Research in Engineering

by

Wangke Yu

ORCID ID https://orcid.org/0000-0002-2643-3010

Thesis for the degree of Doctor of Philosophy

October 2024

University of Southampton

Abstract

Faculty of Engineering and Physical Sciences

Electronics and Computer Science

Doctor of Philosophy

Optical Vortices and their Related Research in Engineering

by

Wangke Yu

Light beams characterised by a spiral front, or more generally, an optical field exhibiting a circulating current density, are termed optical vortices. This thesis investigates two types of optical vortices: monochromatic vortex beams under paraxial approximation and spatiotemporal vortices, and their related research in engineering.

Firstly, for vortex beams, we present a new geometric representation framework called the Total angular momentum-conserving Poincaré sphere (TAM-PS). A wide range of vortex beams can be efficiently characterised by this framework. Additionally, two kinds of braid clusters based on the TAM-PS are introduced, serving as a theoretical cornerstone for vortex beam applications. Furthermore, a method for analysing the orbital angular momentum (OAM) and total angular momentum (TAM) of an unknown vortex beam is introduced. This method aids in analysing the OAM or TAM of vortex beams generated by a meta-surface integrated micro-ring during its design phase based on simulation results. Additionally, a vortex beam reflection computation model is studied, examining the feasibility of using vortex beams as detection signals for light detection and ranging sensors to measure the orientation of reflecting surfaces. Secondly, two controversies regarding spatiotemporal optical vortices (STOVs) are studied: 1. The calculation of transverse OAM; 2. The phase distribution of STOVs in the t-x plane. Additionally, a special kind of STOV, termed the toroidal light pulse, is introduced, and exploratory work on the toroidal momentum for this pulse is presented.

Table of Contents

Table of Tables

Table of Figures

Table of Figures

Table of Figures

Table of Figures

Research Thesis: Declaration of Authorship

Print name: Wangke Yu

Title of thesis: Optical Vortices and their Related Research in Engineering

I declare that this thesis and the work presented in it are my own and has been generated by me as the result of my own original research.

I confirm that:

1. This work was done wholly or mainly while in candidature for a research degree at this University;
2. Where any part of this thesis has previously been submitted for a degree or any other qualification at this University or any other institution, this has been clearly stated;
3. Where I have consulted the published work of others, this is always clearly attributed;
4. Where I have quoted from the work of others, the source is always given. With the exception of such quotations, this thesis is entirely my own work;
5. I have acknowledged all main sources of help;
6. Where the thesis is based on work done by myself jointly with others, I have made clear exactly what was done by others and what I have contributed myself;
7. Parts of this work have been published as journal papers and conference contributions in the list of publications.
8. Chapter 3 involves collaborative research. The complex amplitude data of optical fields analysed in this part were provided by a collaborative group. Using the complex amplitude data they provided, I plotted the intensity distributions and polarization state distributions of these optical fields. The research methods used in this chapter, including the angular momentum spectrum obtained by analysing these fields, represent my personal contributions.

Signature: ..... Date:.....

List of Publications

Journal Publications

Modelling and Analysis of Vector and Vector Vortex Beams Reflection for Optical Sensing. / **Yu W,** Yan J.

In: Photonics, 2024; 11(8)

Asymmetric vortex beam emission from a metasurface-integrated microring with broken conjugate symmetry. / Huang, Jianzhi *; **Yu, Wangke ***; Pi, Hailong; Shen, Yijie; Yan, Jize; Fang, Xu.

In: Optics Express, Vol. 31, No. 25, 04.12.2023, p. 42549-42561.

Geometric representation of vector vortex beams: the total angular momentum-conserving Poincaré sphere and its braid clusters. / **Yu, Wangke**; Pi, Hailong; Taylor, Marika; Yan, Jize.

In: Photonics, Vol. 10, No. 11, 1276, 17.11.2023.

Coherent generation of arbitrary first-order Poincaré sphere beams on an Si chip. / Pi, Hailong; **Yu, Wangke**; Yan, Jize; Fang, Xu.

In: Optics Express, Vol. 30, No. 5, 18.02.2022, p. 7342-7355.

On-chip optical pulse train generation through the optomechanical oscillation. / Xu, Xiangming; Pi, Hailong; **Yu, Wangke**; Yan, Jize.

In: Optics Express, Vol. 29, No. 23, 05.11.2021, p. 38781-38795.

Conference Papers

Metasurface-integrated microring resonators for off-chip vortex beam generation. / Huang, Jianzhi; **Yu, Wangke**; Zheng, Zihang; Yan, Jize; Fang, Xu. Proceedings Volume 12773, Nanophotonics and Micro/Nano Optics IX. ed. / Zhiping Zhou; Kazumi Wada; Limin Tong. Vol. 12773 SPIE, 2023. 127730F.

Acknowledgements

I want to begin by expressing my deep appreciation to my supervisors, Professor Jize Yan, for the unwavering support and guidance provided during my dissertation study. Professor Yan supported me in freely exploring my research field and generously shared his professional knowledge and advice. His encouragement during times of self-doubt has been invaluable. I feel privileged and truly grateful for the opportunity to collaborate with him.

I would like to express my gratitude to the research team led by by Dr. Xu Fang for providing me with the complex amplitude data of the optical field generated by the meta-surface integrated micro-ring resonator. Based on their data, I was able to complete the analysis and study of the total angular momentum and orbital angular momentum of the optical field shown in Chapter 3.

I would like to extend my heartfelt thanks to Dr. Yijie Shen, Dr. David J. Thomson, Dr. Marika Taylor, and Dr. Junyu Ou for their invaluable support, insightful discussions, and collaborative efforts. Their extensive knowledge and experience have significantly contributed to the progress of my research. Special acknowledgment goes to Dr. Hailong Pi, whose assistance with numerical simulation and experiments has been indispensable.

I truly appreciate all the feedback and guidance provided by Professor Jun Yuan and Dr. Nema Abdelazim. Their insights have been incredibly valuable and have genuinely helped me improve this thesis.

I would like to thank my friends and coworkers: Chen Wei, Siyi Wang, Junbo Zhu, Yue Fan, Kai Zhang, Yang Xue, Lulu Zhang, Duo Zhang, Fernanda, Lasara, Kameriah, Yu Feng, Xiangming Xu, Shengqi Yin, Peng Li, Gaoce Han, Ravi, Shumeng Wang, Chuang Sun, Weilin Jin, Jiale Zeng, Jianzhi Huang, Zihang Zheng, Tongjun Zhang, Dongkai Gou, Siyu Chen, Yu Wang, and Wenjie Wang, among many others. Without them, my PhD journey would not have been so enjoyable.

I want to express my gratitude to my parents, grandfather, aunts, and cousins for their love, support, encouragement, and sacrifices. Every achievement I have made is also a result of their contributions.

In loving memory of my grandmother, Guilan Jia.

Definitions and Abbreviations

AM	Angular momentum.
SAM	Spin angular momentum. It is associated with the right- and left-circularly polarised light.
OAM	Orbital angular momentum. It is associated with twisted phase fronts of light.
Optical vortex	A light beam characterised by a spiral front, or more generally, an optical field exhibiting a circulating current density, is termed the optical vortex.
Paraxial approximation	In geometric optics, “paraxial” means the light is well-collimated, all light rays make only slight angles with the beam axis; In wave optics, the angular spectrum of paraxial beams primarily consists of plane waves, which propagate along the beam axis.
Transverse wave	The electric vector of a wave oscillates perpendicular to the direction of propagation.
Direction of propagation	The Poynting vector points in the direction of wave propagation.
Transverse	Motion or some quantities in a position or direction that is perpendicular to the direction of propagation.
Longitudinal	Motion or some quantities in a position or direction that is along the direction of propagation.
Vector nature of light	Light is an electromagnetic wave. Because the electric and magnetic fields of electromagnetic waves are vector quantities, light exhibits vector nature.
LG beam	Laguerre Gaussian beam, solutions to paraxial wave equation in cylindrical coordinates. And it carries well-defined OAM. For details, please check chapter 1.1.1.2
VB	Vector beam. Light beams have spatially variant states of polarization or inhomogeneous polarisation, but no phase vortices, are usually called vector beams. VBs carry no OAM

VVB ..... Vector vortex beam. Beams with both inhomogeneous polarisation and phase vortices are called vector vortex beams. VVBs carry OAM owing to their spiral phase fronts.

Monochromatic light ..... Only a single optical frequency is contained in the monochromatic light.

Polychromatic light ..... The antonym of monochromatic light which has a board range of optical frequencies.

Optical pulses ..... Optical pulses are flashes of light. Lasers are frequently used to generate very short optical pulses (laser pulses). They are transmitted in the form of laser beams which have highly directed energy.

Transverse OAM ..... Intrinsic OAM oriented transverse to its propagation direction. The vortices generated in space-time (also termed spatiotemporal optical vortices (STOV)) can carry the transverse OAM (also named spatiotemporal OAM (ST-OAM))

STOV ..... Spatiotemporal optical vortices. It is an optical vortex with phase and energy circulation in a spatiotemporal plane [45].

ST-OAM ..... Spatiotemporal orbital angular momentum

Optical sensing ..... In an optical sensing process, the device or hardware takes and transduces intensity distribution, power, polarisation states, etc., these physical properties of light into usable information. More specific definition of sensing is driven by application perspectives.

LiDAR ..... Light Detection and Ranging

TOF ..... Time of flight

AMCW ..... Amplitude-modulated continuous wave

FMCW ..... Frequency modulated continuous wave

DoF ..... Degrees of freedom

Chapter 1 Introduction

1.1 Structure of the Entire Thesis

This thesis begins with an overview of the entire work, along with a summary of optical vortices and angular momentum, providing the necessary background knowledge and introduction. Two types of optical vortices are investigated in this work: monochromatic vortex beams under the paraxial approximation and spatiotemporal vortices. Additionally, their related research in engineering is presented in the following chapters. Due to the two research objects (two types of the optical vortices) in this thesis, the following chapters can be classified into two categories: Chapters 2, 3 and 4 are classified into one category; Chapter 5 is classified separately.

In Chapter 1.2, the background knowledge involved in the thesis, including fundamental concepts and methodologies, is explained and detailed.

The vortex beam, associated with optical angular momentum (AM) [1,2,3], has been widely studied as a promising resource for optical manipulation [4]. Due to the variety of types of vortex beams [5], a method to characterise them efficiently is needed. Consequently, in Chapter 2, a geometric representation framework for vortex beams is presented, termed the total angular momentum-conserving Poincaré sphere (TAM-PS). Additionally, two types of TAM-PS braid clusters are introduced. Chapter 2 serves as a theoretical cornerstone for the application research of vortex beams. Based on this framework, a wide range of vortex beams can be characterised efficiently.

Micro-ring vortex beam emitters are one of the popular methods for vortex beam generation [6]. Researchers in this field call for a general method that can help numerically analyse the orbital angular momentum (OAM) or total angular momentum (TAM) of the generated vortex beams. Therefore, in Chapter 3, an approach to analysing vortex beams is introduced. This study facilitates the examination of OAM or TAM in vortex beams produced by a meta-surface integrated micro-ring, using simulation data during the design stage.

Vector beams and vector vortex beams (VVBs) are expected to be applied to light detection and ranging (LiDAR) sensors [7]. Under this context, the feasibility of using vector beams or VVBs as detection signals to determine the orientation of a reflecting surface is examined in Chapter 4. We present the modelling and analysis of vector beams and vector vortex beams for optical sensing applications. It develops a computational model that examines the reflection characteristics of vector beams (VB) and vector vortex beams (VVB).

Research on vortex beams carrying longitudinal OAM is growing rapidly and has been applied to diverse areas [8,9,10,11,12]. However, research on transverse OAM carried by optical pulses or wave packets is still in an emerging stage [13]. These optical pulses are spatiotemporal optical vortices (STOVs), a type of specially designed optical pulse that has become a popular research area in recent years [14]. Chapter 5 presents some theoretical studies of STOVs and transverse OAM, intending to provide useful insights for optical vortex research. This chapter is structured into two sections. The first section investigates the transverse OAM carried by STOV and their phase distribution. The second section, drawing inspiration from the definition of angular momentum, introduces and elaborates on a new physical quantity for an innovative type of optical pulse known as the “toroidal pulse”, which is provisionally referred to as “toroidal momentum”.

Chapter 6 provides the conclusion for the entire doctoral thesis. Additionally, discussions on the future developments and research prospects concerning optical vortices and optical angular momenta are included.

1.2 Fundamental Theories of Optical Vortices and Angular Momentum

A light beam, characterised by its spiral front, or more broadly, an optical field with a circulating current density, is known as an optical vortex. This phenomenon is linked to optical angular momentum (AM). For over three decades, optical vortices have been a crucial element of modern optics, leading to significant advancements and a wide range of applications [15].

1.2.1 Understanding Optical Angular Momentum and Its Associated Fields

1.2.1.1 Fundamentals of Optical Spin and Orbital Angular Momentum

After the foundational work by Poynting [16] and the initial experimental evidence provided by Beth [17], angular momentum has been recognized as a fundamental characteristic of light. Specifically, spin angular momentum (SAM) is generated by the circularly polarised state of a light beam. In 1992, Allen et al. initiated a new phase in optical AM research by reporting orbital angular momentum (OAM) in vortex beams [18], which was later experimentally confirmed by another research group [19]. From then on, the field of optical AM has evolved into a major area of scientific inquiry [20].

SAM is closely associated with the circular polarisation of light, where the positive ($\sigma = +1\hbar$) and negative helicities ($\sigma = -1\hbar$) correspond to right- and left-circularly polarised light, respectively.

Figure 1.1 [21] illustrates schematics of right- and left-circularly polarised light beams along with their respective SAM values.

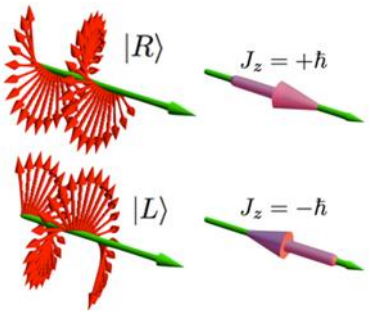

Figure 1.1 shows a schematic of two circularly polarised light beams along with their associated SAM [21]. The state of circular polarisation, either right or left, is determined by the direction of the polarisation field's rotation and the convention applied, specifically from the perspective of the source or the receiver. This figure adopts the viewpoint of the source. The symbol $|R\rangle$ represents the right-circularly polarised light beam, and the symbol $|L\rangle$ represents the left-circularly polarised light beam.

As for the OAM, it is generated by the circulation of momentum and phase, and it is independent of the light's polarisation. OAM can be classified into two types: longitudinal OAM and transverse OAM. This section assumes that the optical field is a monochromatic beam under paraxial approximation, referring specifically to longitudinal OAM. Transverse OAM, which pertains to optical pulses, will be discussed in section 1.1.4. In geometric optics, “paraxial” implies that the light is well-collimated, with all light rays making only slight angles with the beam axis. In wave optics, the angular spectrum of paraxial beams predominantly comprises plane waves that propagate along the beam axis.

Longitudinal OAM has been extensively studied and applied since it was closely linked to optical vortices, in particular, Laguerre Gaussian beams. The longitudinal OAM carried by monochromatic beams under paraxial approximation is intrinsic and oriented along the beam’s axis. “Intrinsic” indicates that the OAM is independent of the coordinate origin [22]. Unlike SAM, the value of intrinsic OAM can be any integer, including zero. Figure 1.2 [23] displays a diagram of vortex beams with various values of longitudinal OAM, denoted by the variable m.

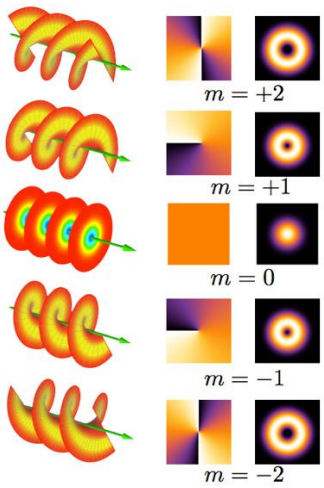

Figure 1.2 shows diagrams of monochromatic vortex beams under paraxial approximation with different longitudinal OAM. There are three columns. The first column to the third column displays diagrams of beams carrying different OAM, corresponding phase distributions, and intensity distributions in the transverse plane. The symbol m represents the value of the OAM [23].

Consequently, in optics, SAM and OAM are distinct quantities [24, 25]. In the following sections, the separation of SAM and OAM will be demonstrated.

We know the classical definition of angular momentum is [26]

$$\boldsymbol{J} = \int \boldsymbol{x} \times \boldsymbol{p}\, dv\,. \tag{1.1}$$

$\boldsymbol{x}$ represents the radial position and $\boldsymbol{p}$ represents the respective linear momentum density of the electromagnetic field. Then, Eq. (1.1) can be written as [27]

$$\boldsymbol{J} = \varepsilon_0 \int \boldsymbol{x} \times (\boldsymbol{E} \times \boldsymbol{B}) dv\,. \tag{1.2}$$

Introducing the vector potential $\boldsymbol{A}$, we have

$$\boldsymbol{E} \times \boldsymbol{B} = \boldsymbol{E} \times (\nabla \times \boldsymbol{A}) = \nabla \boldsymbol{A} \cdot \boldsymbol{E} - (\boldsymbol{E} \cdot \nabla)\boldsymbol{A}. \tag{1.3}$$

Substitute Eq. (1.3) into Eq. (1.2), we have,

$$\boldsymbol{J} = \varepsilon_0 \int \boldsymbol{x} \times (\nabla \boldsymbol{A} \cdot \boldsymbol{E}) dv - \varepsilon_0 \int \boldsymbol{x} \times [(\boldsymbol{E} \cdot \nabla)\boldsymbol{A}] dv\,. \tag{1.4}$$

$\nabla \boldsymbol{A}$ can be rewritten using index notation, and we are working under the Cartesian metric [28]

$$\nabla \boldsymbol{A} = \sum_{i,j} \frac{\partial A_j}{\partial x_i} \boldsymbol{e_i} \boldsymbol{e_j}\,. \tag{1.5}$$

The terms $\nabla \boldsymbol{A} \cdot \boldsymbol{E}$ and $(\boldsymbol{E} \cdot \nabla)\boldsymbol{A}$ can also be rewritten in the following forms:

$$\nabla \boldsymbol{A} \cdot \boldsymbol{E} = \sum_{i,j} \frac{\partial A_j}{\partial x_i} E_j \boldsymbol{e_i} . \tag{1.6}$$

$$(\boldsymbol{E} \cdot \nabla)\boldsymbol{A} = \sum_{i,j} E_j \frac{\partial A_i}{\partial x_j} \boldsymbol{e_i} . \tag{1.7}$$

Substitute Eq. (1.6) and (1.7) into Eq. (1.4) and use the Levi-Civita symbol $\epsilon_{i,j,k}$ to rewrite the cross- product terms: $\boldsymbol{x} \times (\nabla \boldsymbol{A} \cdot \boldsymbol{E})$ and $\boldsymbol{x} \times [(\boldsymbol{E} \cdot \nabla)\boldsymbol{A}]$. Then we have

$$\boldsymbol{x} \times (\nabla \boldsymbol{A} \cdot \boldsymbol{E}) = \sum_{i,j,k} \epsilon_{i,j,k} x_j (\nabla \boldsymbol{A} \cdot \boldsymbol{E})_k \boldsymbol{e_i} = \sum_{i,j,k} \epsilon_{i,j,k} x_j \left(\sum_p \frac{\partial A_p}{\partial x_k} E_p \right) \boldsymbol{e_i} =$$

$$\sum_p E_p \left(\sum_{i,j,k} \epsilon_{i,j,k} x_j \frac{\partial}{\partial x_k} \boldsymbol{e_i} \right) A_p = \sum_p E_p (\boldsymbol{x} \times \nabla) A_p . \tag{1.8}$$

$$\boldsymbol{x} \times [(\boldsymbol{E} \cdot \nabla)\boldsymbol{A}] = \sum_{i,j,k} \epsilon_{i,j,k} x_j \big((\boldsymbol{E} \cdot \nabla)\boldsymbol{A} \big)_k \boldsymbol{e_i} = \sum_{i,j,k} \epsilon_{i,j,k} x_j \left(\sum_p \frac{\partial A_k}{\partial x_p} E_p \right) \boldsymbol{e_i} =$$

$$\sum_{i,j,k,p} \epsilon_{i,j,k} x_j \frac{\partial A_k}{\partial x_p} E_p \boldsymbol{e_i} . \tag{1.9}$$

Rewrite Eq. (1.9) using the total differential

$$\sum_{i,j,k,p} \epsilon_{i,j,k} x_j \frac{\partial A_k}{\partial x_p} E_p \boldsymbol{e_i} = \sum_{i,j,k,p} \epsilon_{i,j,k} \frac{\partial \big(x_j A_k E_p \big)}{\partial x_p} \boldsymbol{e_i} - \sum_{i,j,k,p} \epsilon_{i,j,k} A_k E_p \frac{\partial x_j}{\partial x_p} \boldsymbol{e_i} -$$

$$\sum_{i,j,k,p} \epsilon_{i,j,k} x_j A_k \frac{\partial E_p}{\partial x_p} \boldsymbol{e_i} . \tag{1.10}$$

By analysing the three terms on the right side of Eq. (1.10) respectively, we get

$$\sum_{i,j,k,p} \epsilon_{i,j,k} \frac{\partial \big(x_j A_k E_p \big)}{\partial x_p} \boldsymbol{e_i} = \sum_p \frac{\partial}{\partial x_p} \left[E_p \sum_{i,j,k} \epsilon_{i,j,k} x_j A_k \boldsymbol{e_i} \right] = \sum_p \frac{\partial}{\partial x_p} \big[E_p (\boldsymbol{x} \times \boldsymbol{A}) \big] = \nabla \cdot [\boldsymbol{E} (\boldsymbol{x} \times \boldsymbol{A})] \tag{1.11}$$

$$\sum_{i,j,k,p} \epsilon_{i,j,k} A_k E_p \frac{\partial x_j}{\partial x_p} \boldsymbol{e_i} = \sum_{i,j,k} \epsilon_{i,j,k} \delta_{j,p} A_k E_p \boldsymbol{e_i} = \sum_{i,j,k} \epsilon_{i,j,k} A_k E_j \boldsymbol{e_i} = \boldsymbol{E} \times \boldsymbol{A} \tag{1.12}$$

$$\sum_{i,j,k,p} \epsilon_{i,j,k} x_j A_k \frac{\partial E_p}{\partial x_p} \boldsymbol{e_i} = \sum_{i,j,k} \epsilon_{i,j,k} x_j A_k \boldsymbol{e_i} (\nabla \cdot \boldsymbol{E}) = 0 \tag{1.13}$$

If these equations were studied in locations of space very far from the charge distribution ρ, then we could set the charge terms to be zero in Maxwell's equations. Therefore, $\nabla \cdot \boldsymbol{E} = 0$, and Eq. (1.13) equals 0. Substitute Eq. (1.8) and Eqs. (1.11–1.13) into Eq. (1.4), and we have

$$\boldsymbol{J} = \varepsilon_0 \int \boldsymbol{x} \times (\boldsymbol{E} \times \boldsymbol{B}) dv = \varepsilon_0 \int \left(\sum_p E_p (\boldsymbol{x} \times \nabla) A_p - \nabla \cdot [\boldsymbol{E}(\boldsymbol{x} \times \boldsymbol{A})] + \boldsymbol{E} \times \boldsymbol{A} \right) dv \tag{1.14}$$

The second term of Eq. (1.14) can be rewritten as $\int \nabla \cdot [\boldsymbol{E}(\boldsymbol{x} \times \boldsymbol{A})] dv = \oiint_{\Sigma} [\boldsymbol{E}(\boldsymbol{x} \times \boldsymbol{A})] \cdot d\boldsymbol{s}$ according to the Gauss' theorem. Then with the assumption that the optical field exists in a finite space but integrating in an infinite space we have $\oiint_{\Sigma} [\boldsymbol{E}(\boldsymbol{x} \times \boldsymbol{A})] \cdot d\boldsymbol{s} = 0$. Consequently, Eq. (1.14) can be rewritten as

$$\boldsymbol{J} = \varepsilon_0 \int \left(\sum_p E_p (\boldsymbol{x} \times \nabla) A_p + \boldsymbol{E} \times \boldsymbol{A} \right) dv = \boldsymbol{L} + \boldsymbol{S} \tag{1.15}$$

The first term of Eq. (1.15) is the orbital component ($\boldsymbol{L}$) associated with the OAM, and the second term is the spin component ($\boldsymbol{S}$) associated with the SAM [29].

1.2.1.2 Circularly Polarised Light Beams and Spin Angular Momentum (SAM)

Monochromatic light under paraxial approximation is a time-harmonic electromagnetic wave:

$$\boldsymbol{E} = -\frac{\partial \boldsymbol{A}}{\partial t} = -i\omega \boldsymbol{A}, \qquad \boldsymbol{A} = \frac{\boldsymbol{E}}{i\omega} \tag{1.16}$$

Substitute Eq. (1.16) into $\boldsymbol{E} \times \boldsymbol{A}$ and the time average of the spin angular momentum is

$$\boldsymbol{S}_{avg} = \frac{\varepsilon_0}{2\omega} \int Re\left(\boldsymbol{E}^* \cdot \frac{\boldsymbol{E}}{i} \right) dv \tag{1.17}$$

For simplicity, we assume the light is circularly polarised and propagates along the $\boldsymbol{z}$ direction:

$$\boldsymbol{E} = (\boldsymbol{e_x} \pm i\boldsymbol{e_y}) E_0 \tag{1.18}$$

Substitute Eq. (1.18) into Eq. (1.17), we have

$$\boldsymbol{S}_{avg} = \pm \boldsymbol{e_z} \frac{\varepsilon_0}{\omega} \int {E_0}^2 \, dv \tag{1.19}$$

The energy of the electromagnetic field is

$$w = \frac{1}{2} \int \left(\varepsilon_0 {E_0}^2 + \frac{1}{\mu_0} {B_0}^2 \right) dv = \int \varepsilon_0 {E_0}^2 \, dv \tag{1.20}$$

Substitute Eq. (1.20) into Eq. (1.19), we have

$$\boldsymbol{S}_{avg} = \pm \boldsymbol{e_z} \frac{w}{\omega} \tag{1.21}$$

Use the reduced Planck's constant to express w:

$$w = \hbar\omega \tag{1.22}$$

Finally, $\boldsymbol{S}_{avg}$ is

$$\boldsymbol{S}_{avg} = \pm \boldsymbol{e_z}\hbar \tag{1.23}$$

Therefore, the quantum number of SAM for circularly polarised beams is$+1$ or -1.

1.2.1.3 Laguerre-Gaussian Beams and Longitudinal Orbital Angular Momentum (OAM)

Light is an electromagnetic wave described by Maxwell's equations. Based on the assumption that light propagates in a linear, isotropic, homogeneous, and source-free space, a simplified version of Maxwell's equations, known as the Helmholtz equations, can be obtained:

$$(\nabla^2 + k^2)\begin{pmatrix}\boldsymbol{\mathcal{H}}\\ \boldsymbol{\mathcal{E}}\end{pmatrix} = 0 \tag{1.24}$$

Here, $\boldsymbol{\mathcal{E}}$ and $\boldsymbol{\mathcal{H}}$ are the spatially dependent parts of the electric and magnetic fields, i.e., $\boldsymbol{E} = Re[\boldsymbol{\mathcal{E}}\exp(-i\omega t)]$ and $\boldsymbol{H} = Re[\boldsymbol{\mathcal{H}}\exp(-i\omega t)]$. k is the overall wavenumber, given by $k = \omega/c$. To avoid inconsistencies between $\nabla \cdot \boldsymbol{E} = 0$ and the paraxial approximation to the electric field Helmholtz equation, as detailed by Lax et al. [30], we use the Helmholtz equation for the vector potential $\boldsymbol{A}$ shown in Eq. (1.25) to study the paraxial approximation to the Helmholtz equation [31].

$$\nabla^2\boldsymbol{\mathcal{A}} + k^2\boldsymbol{\mathcal{A}} = 0, \qquad \boldsymbol{A} = Re[\boldsymbol{\mathcal{A}}\exp(-i\omega t)] \tag{1.25}$$

We assume the optical field is uniformly polarised, meaning it has a constant polarisation vector of unit modulus. Consequently, the vectorial form of the Helmholtz equation can be transformed into the scalar wave equation, which is

$$\nabla^2 U + k^2 U = 0 \tag{1.26}$$

Based on the assumption of paraxial approximation and z is chosen as the direction of light propagation, we can consider the $U(\boldsymbol{r})$ as shown in Eq. (1.27) as the ansatz for a solution to the scalar Helmholtz equation Eq. (1.26) [32]

$$U(\boldsymbol{r}) = u(\boldsymbol{r})\exp(ikz) \tag{1.27}$$

Substitute Eq. (1.27) into Eq. (1.26), we have

$$\begin{gathered}\nabla^2 u(\boldsymbol{r})\exp(ikz)+k^2u(\boldsymbol{r})\exp(ikz)=0, \quad \Longrightarrow \\ \partial_x^2 U(\boldsymbol{r})+\partial_y^2 U(\boldsymbol{r})+\partial_z^2[u(\boldsymbol{r})\exp(ikz)]+k^2u(\boldsymbol{r})\exp(ikz)=0, \quad \Longrightarrow \\ \partial_x^2 U(\boldsymbol{r})+\partial_y^2 U(\boldsymbol{r})+\partial_z\{\partial_z[u(\boldsymbol{r})\exp(ikz)]\}+k^2u(\boldsymbol{r})\exp(ikz)=0, \quad \Longrightarrow \\ \partial_x^2 U(\boldsymbol{r})+\partial_y^2 U(\boldsymbol{r})+ikexp(ikz)\partial_z u(\boldsymbol{r})+\exp(ikz)\,\partial_z^2 u(\boldsymbol{r})-k^2\exp(ikz)\,u(\boldsymbol{r})+\cdots \\ ikexp(ikz)\partial_z u(\boldsymbol{r})+k^2u(\boldsymbol{r})\exp(ikz)=0, \quad \Longrightarrow \\ \partial_x^2 U(\boldsymbol{r})+\partial_y^2 U(\boldsymbol{r})+\exp(ikz)\,\partial_z^2 u(\boldsymbol{r})+2ikexp(ikz)\partial_z u(\boldsymbol{r})=0. \end{gathered} \tag{1.28}$$

After that, a partial differential equation for the amplitude distribution u can be obtained:

$$\partial_x^2 u+\partial_y^2 u+\partial_z^2 u+2ik\partial_z u=0. \tag{1.29}$$

Because the paraxial approximation which indicates the profile of the light beam changes very slowly along the propagation direction (z-direction), the term $\partial_z^2 u$ can be neglected in Eq. (1.29). Then, Eq. (1.29) can be rewritten as:

$$\partial_x^2 u+\partial_y^2 u+2ik\partial_z u=0. \tag{1.30}$$

Eq. (1.30) is known as the paraxial wave equation. By rewriting it in in cylindrical coordinates (ρ,φ,z), as shown in Eq. (1.31), we obtain one of its solutions, termed the Laguerre-Gaussian (LG) mode/beam.

$$\left(\frac{1}{\rho}\partial_\rho+\partial_\rho^2+\frac{1}{\rho^2}\partial_\varphi^2+2ik\partial_z\right)u_p^\ell=0. \tag{1.31}$$

Here ρ represents the radial coordinate and φ represents the azimuthal coordinate. Eq. (1.32) u_p^ℓ is the normalized form of the LG beam [32]:

$$u_p^\ell=LG_p^\ell(\rho,\varphi,z)=\frac{C_{\ell p}^{LG}}{\sqrt{w(z)}}\left(\frac{\rho\sqrt{2}}{w(z)}\right)^{|\ell|}e^{-\frac{\rho^2}{w^2(z)}}L_p^{|\ell|}\left(\frac{2\rho^2}{w^2(z)}\right)e^{-\frac{ik\rho^2 z}{2(z_R^2+z^2)}}e^{i\ell\varphi}e^{[-i(2p+|\ell|+1)\chi(z)]} \tag{1.32}$$

Here, ℓ, p and $w(z)$ represent azimuthal index, radial index, and beam width, respectively; The normalisation constant is denoted as $C_{\ell p}^{LG}=\sqrt{2^{|\ell|+1}p!/\pi(p+|l|)!}$; The Rayleigh range, $z_R=\frac{\pi w_0^2}{\lambda}$, serves as a measure for the focal region; The term $(2p+|\ell|+1)\chi(z)$ corresponds to the Gouy phase which characterises a phase shift of π that occurs across the focal region of any spherical converging wave, and this behaviour is evident from the function's form: $tan\chi(z)=z/z_R$.

Importantly, the phase factor $e^{i\ell\varphi}$ is responsible for well-defined OAM. It involves the dynamic rotation of light rays around the central axis of the beam, where ℓ is named the topological (TC) number, taking values of 0 or any integer [18]. Eq. (1.33) is the expression of the longitudinal OAM flux density $\rho_z(r,\varphi)$ in polar coordinates:

$$\rho_z(r,\varphi) = \boldsymbol{\Psi}^*(\boldsymbol{x} \times i\boldsymbol{\nabla}_{\boldsymbol{x}})\boldsymbol{\Psi} = \boldsymbol{\Psi}^*(r,\varphi)\frac{\partial}{\partial\varphi}\boldsymbol{\Psi}(r,\varphi) \tag{1.33}$$

Here, $\boldsymbol{x}$ represents the position operator; $i\boldsymbol{\nabla}_{\boldsymbol{x}}$ represents the linear momentum operator; $\boldsymbol{x} \times i\boldsymbol{\nabla}_{\boldsymbol{x}}$ defines the OAM operator; $\boldsymbol{\Psi}$ represents the field of vortex beams under paraxial approximation. Then, the quantum number (or topological charge) of the longitudinal OAM (TC_{OAM}) is:

$$TC_{OAM} = \frac{\iint \rho_z(r,\varphi) r dr d\varphi}{\iint \boldsymbol{\Psi}^*\boldsymbol{\Psi} r dr d\varphi} \tag{1.34}$$

Substitute Eq. (1.32) into Eq. (1.34), LG beams' TC_{OAM} equals ℓ . Additionally, these LG beams form an orthogonal set in the mode index p and ℓ when integrated over the full $\rho - \varphi$ plane:

$$\int_0^{2\pi} d\phi \int_0^{\infty} \rho d\rho \, u_{\ell,p}^{LG}(\rho,\varphi,z)\left[u_{m,q}^{LG}(\rho,\varphi,z)\right]^* = \delta_{\ell m}\delta_{pq} \tag{1.35}$$

The following Figure 1.3 [32] is the intensity profiles of LG beams. Panel (a) has mode indices $\ell = 1$, $p = 0$; panel (b) has mode indices $\ell = 5$, $p = 0$; panel (c) has mode indices $\ell = 2$, $p = 1$; panel (d) has mode indices $\ell = 2$, $p = 2$.

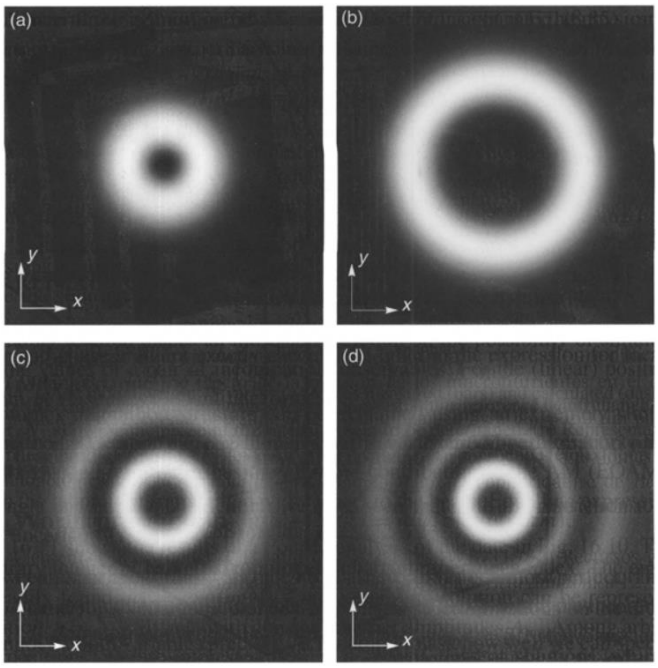

Figure 1.3 The intensity distribution of LG beams with different modes in transverse plane ($x - y$ plane); Panel (a) has mode indices $\ell = 1$, $p = 0$; panel (b) has mode indices $\ell = 5$, $p = 0$; panel (c) has mode indices $\ell = 2$, $p = 1$; panel (d) has mode indices $\ell = 2$, $p = 2$ [32].

1.2.2 Vector Beams and Vector Vortex Beams

Polarisation is vector nature of light. There are two types of polarization states. The first type is independent of the spatial position of the transverse plane of the beam which is also named homogeneous polarisation states. Examples include linear, elliptical, and circular polarisation. The second type consists of light beams with spatially variant states of polarisation, such as cylindrical vector (CV) beams, which are cylindrically symmetric in polarisation. This category includes radially polarised beams, azimuthally polarised beams, and CV beams with hybrid polarisation states [33]. Additionally, “lemon” and “star” polarised beams also belong to vector beams. And due to topological structures caused by the beams’ dislocation, the beams are named “lemon” or “star” [34].

Vector beams (VB) and in particular vector vortex beams (VVB) are natural solutions to the full vector wave equation [35]. More commonly, they are represented as the superposition of orthogonal scalar fields with orthogonal polarisation states [36], as shown in Eq. (1.36)

$$|VB\rangle = \psi_R^{\ell_R}\left|R_p^{\ell_R}\right\rangle + \psi_L^{\ell_L}\left|L_p^{\ell_L}\right\rangle, \tag{1.36}$$

$$\left|R^{\ell_R}\right\rangle = \frac{1}{\sqrt{2}} e^{i\ell_R\varphi}\left(\hat{e}_x - i\hat{e}_y\right),$$

$$\left|L^{\ell_L}\right\rangle = \frac{1}{\sqrt{2}} e^{i\ell_L\varphi}\left(\hat{e}_x + i\hat{e}_y\right),$$

$$\psi_R^{\ell_R} = sin\,(\beta/2)\,,$$

$$\psi_L^{\ell_L} = cos\,(\beta/2)\,e^{+i\phi}.$$

We use the notation $|VB\rangle$ to represent a vector beam. The symbols $\left|R^{\ell_R}\right\rangle$ and $\left|L^{\ell_L}\right\rangle$represent a pair of orthogonal eigenstates. Specifically, these eigenstates are right-circularly and left-circularly polarised LG beams with OAM quantified as $\ell_R\hbar$, $\ell_L\hbar$, respectively. The symbols $\psi_R^{\ell_R}$, $\psi_L^{\ell_L}$ represent the coefficients of these two eigenstates, which are defined by relative intensity (variables $\beta \in [0,\pi]$) and relative phase ($\phi \in [0,2\pi]$). In following, several types of VBs which are the research objects in Chapter 4 will be introduced.

In this thesis, to avoid ambiguity, light beams with spatially variant states of polarisation or inhomogeneous polarisation, but without phase vortices, are usually called vector beams. Beams with both inhomogeneous polarisation and phase vortices are called vector vortex beams. Vector beams carry no OAM, whereas VVBs carry OAM due to their spiral phase fronts [5]

- Radially polarised beam

In Eq. (1.36), if $\ell_R = 1, \ell_L = -1$, and $\phi = 0$, the radially polarised beam is defined. Figure 1.4 shows a diagram for the intensity and polarisation distribution of the radially polarised beams. The colormap from blue to white to red represents increasing intensity. The intensity has been normalised by the maximum. Since the OAM modes carried by the eigenstates are not zero, the intensity distributions have doughnut shapes, with vanishing intensity at the centre; The size of the lines represents polarisation states of that area. To make the diagram clearer, the size of the line is set to be proportional to the intensity of that area; consequently, the polarization state at the centre of the images is a small point. This also applies to the diagrams of field distribution demonstrated in the following sections. Because the direction of polarisation is along the radial direction, this light is named radially polarised beam.

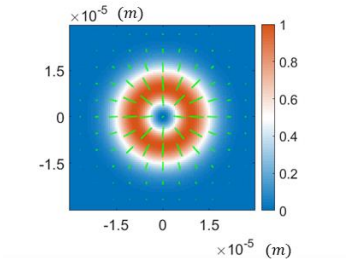

Figure 1.4 shows a diagram of intensity and polarisation distribution of the radially polarised light beam in its cross section. The colormap from blue to white to red indicates increasing intensity. The intensity has been normalised by the maximum.

- Azimuthally polarised beam

In Eq. (1.36), if $\ell_R = 1, \ell_L = -1$, and $\phi = \pi$, the azimuthally polarised beam is defined. Figure 1.5 shows a diagram of the intensity and polarisation distribution of the azimuthally polarised beams. Because the direction of polarisation is along the azimuthal direction, this light is termed azimuthally polarised beam.

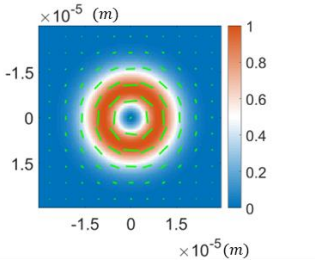

Figure 1.5 shows a diagram of intensity and polarisation distribution of the azimuthally polarised light in the beam's cross section. The colormap from blue to white to red indicates increasing intensity. The intensity has been normalised by the maximum.

- Vector beams with hybrid states of polarisation and two types of VVBs

In Eq. (1.36), if the moduli of ℓ_R and ℓ_L are larger than 1, and $\phi = 0$, the vector beams with hybrid states of polarisation beam are defined. Figure 1.6 shows diagrams of the intensity and polarisation distribution of three types of these beams. And if $\ell_R = -1, \ell_L = -2$, and $\phi = 0$; the "lemon" polarised vortex beam is defined; if $\ell_R = 1, \ell_L = 2$, and $\phi = 0$, the "star" polarised vortex beam is defined. Figure 1.7 shows diagrams of the intensity and polarisation distribution of the two types of VVBs.

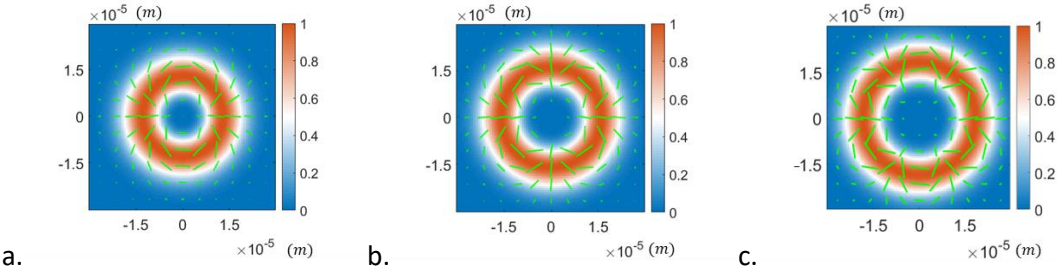

a. b. c.

Figure 1.6 shows diagrams of intensity and polarisation distribution of the three types of vector beams with hybrid states of polarisation in beams' cross section. The corresponding light's eigenstates of panel (a), (b) and (c), are: $(\ell_R = 2, \ell_L = -2, \phi = 0)$; $(\ell_R = 3, \ell_L = -3, \phi = 0)$; $(\ell_R = 4, \ell_L = -4, \phi = 0)$, respectively. The colormap from blue to white to red indicates increasing intensity. The intensity has been normalised by the maximum.

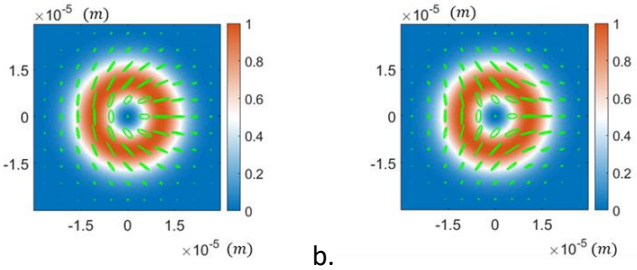

a. b.

Figure 1.7 shows diagrams of the intensity and polarisation distribution of the "lemon" and "star" polarised VVB in their cross section. The colormap from blue to white to red indicates increasing of the intensity. The corresponding light's eigenstates of panel (a) and (b) are: $(\ell_R = -1, \ell_L = -2, \phi = 0)$; $(\ell_R = 1, \ell_L = 2, \phi = 0)$, respectively.

1.2.3 Optical Pulses and Spatiotemporal Angular Momentum

1.2.3.1 Optical Pulses

Optical pulses (also termed wave packets or pulsed beams) are flashes of light [37]. Lasers are frequently used to generate very short optical pulses. These pulses are transmitted in the form of pulsed beams that have highly directed energy. Optical pulses can be ultrashort due to the tremendously high optical frequencies. Generally, the spatial and temporal factors of the optical pulse, or their equivalents in the Fourier domain, are separated [38]:

$$E(x,y,z,t) = E_{xyz}(x,y,z)E_t(t) \qquad \propto \qquad \exp(ik_0 z)\exp(i\omega_0 t) \qquad (1.37)$$

After the Fourier transform to t, the electric field E will be

$$\tilde{E}(x,y,z,\omega) = E_{xyz}(x,y,z)\tilde{E}_t(\omega) \qquad \propto \qquad \exp(ik_0 z)\,\delta(\omega-\omega_0) \qquad (1.38)$$

After the Fourier transform to x, y, z , we have,

$$\hat{E}(k_x,k_y,k_z,t) = \hat{E}_{xyz}(k_x,k_y,k_z)E_t(t) \qquad \propto \qquad \delta(k_x)\delta(k_y)\delta(k_z-k_0)\exp(i\omega_0 t) \quad (1.39)$$

After the Fourier transform to both time and space, we have,

$$\mathfrak{E}(k_x,k_y,k_z,\omega) = \hat{E}_{xyz}(k_x,k_y,k_z)\tilde{E}_t(\omega) \qquad \propto \qquad \delta(k_x)\delta(k_y)\delta(k_z-k_0)\,\delta(\omega-\omega_0) \quad (1.40)$$

k_x, k_y, k_z are the $x-, y-, z-$ components of the wave vector $\boldsymbol{k}$; ω is the frequency; ω_0 represents the central frequency, and $k_0 = \omega_0/c$ is the corresponding overall wavenumber.

It should be noted that, sometimes, the spatial and temporal factors of the optical pulse might not be separated [39]. In the study of optical pulses, the spectral representation on the surface of the light cone is a useful tool that provides physical intuition to help research the pulses' structure and behaviour. We start with the dispersion relationship (Eq. (1.41)) firstly [40],

$$k_x^2 + k_y^2 + k_z^2 = \left(\frac{\omega}{c}\right)^2 \qquad (1.41)$$

Eq. (1.41) mathematically corresponds to a 4D hyper cone. To visualise it in 3D space, the assumption that the optical field is cylindrically symmetric is applied. Indeed, most of the time, researchers are interested in cylindrically symmetric optical fields, so this assumption is reasonable. Under this assumption, Eq. (1.41) can be rewritten as

$$k_r^2 + k_z^2 = \left(\frac{\omega}{c}\right)^2, \qquad (1.42)$$

where $k_r = \sqrt{k_x^2 + k_y^2}$, and $k_r \geq 0$. After that, the dispersion relationship Eq. (1.42) can be visualised in 3D space defined by $\left\{k_r, k_z, \frac{\omega}{c}\right\}$.

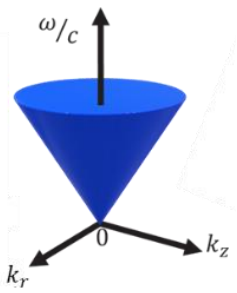

Figure 1.8 shows a diagram of the spatiotemporal spectral representation on the surface of light-cone in a 3D space defined by $\left\{k_r, k_z, \frac{\omega}{c}\right\}$.

Usually, a pulsed beam (optical pulse/ wave packets) is given in terms of a slowly varying envelope $\psi(x, y, z, t)$ and a carrier term $\exp(ik_0 z - i\omega_0 t)$. The envelope $\psi(x, y, z; t)$ can be expressed by the angular spectrum:

$$\psi(x, y, z; t) = \iiint dk_x dk_y d(\omega - \omega_0)\, \tilde{\psi}\left(k_x, k_y, (\omega - \omega_0)\right) \mathrm{e}^{\mathrm{i}\{xk_x + yk_y + z(k_z - k_0) - (\omega - \omega_0)t\}}, \quad (1.43)$$

where $\tilde{\psi}\left(k_x, k_y, (\omega - \omega_0)\right)$ is the Fourier spectrum of $\psi(x, y, 0; t)$. Based on the assumption that the optical field is cylindrically symmetric, we can rewrite the above equations in polar coordinates. Consequently, the following relations hold in both Fourier space and physical space, as shown in Eq. (1.44) and Eq. (1.45).

$$k_r = \sqrt{k_x^2 + k_y^2};\ \phi = \arctan\left(\frac{k_y}{k_x}\right);\ k_x = k_r sin\phi;\ k_y = k_r cos\phi \quad (1.44)$$

$$r = \sqrt{x^2 + y^2};\ \varphi = \arctan\left(\frac{y}{x}\right);\ x = rsin\varphi;\ y = rcos\varphi \quad (1.45)$$

Then, rewriting Eq. (1.43) in polar coordinates, we have

$$\psi(x, y, z; t) = \iiint k_r dk_r d\phi d(\omega - \omega_0)\, \tilde{\psi}\left(k_r, \phi, (\omega - \omega_0)\right) e^{i[rk_r cos(\varphi - \phi) + z(k_z - k_0) - (\omega - \omega_0)t]},$$
$$\phi \in [-\pi, \pi], k_r \in [0, \infty), \omega - \omega_0 \in \left[-\frac{\Delta\omega}{2}, +\frac{\Delta\omega}{2}\right], \quad (1.46)$$

where $\Delta\omega$ represents the frequency spectral width of the pulse. Bessel beams are the simplest monochromatic solutions to wave equations [41] and their azimuthal, radial, and axial parts are all separated. Then, $\tilde{\psi}\left(k_r, \phi, (\omega - \omega_0)\right)$ can be given in the form of separated radial and azimuthal parts:

$$\tilde{\psi}\left(k_r, \phi, (\omega - \omega_0)\right) = \frac{1}{2\pi} \sum_{\ell=-\infty}^{+\infty} e^{i\ell\phi} \widetilde{\psi_\ell}\left(k_r, (\omega - \omega_0)\right) \quad (1.47)$$

The corresponding envelope of the wave packet in real space is

$$\psi(r,\varphi,z;t)=\sum_{\ell=-\infty}^{+\infty}e^{i\ell\varphi}\iint k_r dk_r d(\omega-\omega_0)J_\ell(rk_r)\widetilde{\psi_\ell}\big(k_r,(\omega-\omega_0)\big)e^{i[z(k_z-k_0)-(\omega-\omega_0)t]}, \quad (1.48)$$

where $J_\ell(\xi)$ is the Bessel function of the first kind. This is the approach to studying the optical pulse. One thing worth noting is that there is an azimuthal phase factor $e^{i\ell\varphi}$ in Bessel beams. This phase factor is the same as that in LG modes, which indicates that the Bessel beam can carry OAM as well [32]. However, unlike LG beams, which are solutions to the paraxial wave equation, Bessel beams are exact solutions to the full Helmholtz equation.

1.2.3.2 Transverse Angular Momentum and Spatiotemporal Optical Vortices

The monochromatic vortex beam under paraxial approximation (i.e., LG beam) is usually used to refer to optical OAM [42]. More precisely, this OAM is longitudinal OAM, which is collinear with the momentum of the vortex beam, and its projection on the beam axis is quantised. The study and application of the vortex beam have been actively pursued [43, 44]. Consequently, one naturally inquires: Is there any optical field that can carry intrinsic OAM oriented transversely to its propagation direction? The answer is: Yes. Spatiotemporal optical vortices (STOV), which are optical vortices with phase and energy circulation in a spatiotemporal plane [45], can carry transverse OAM (also named spatiotemporal OAM (ST-OAM)) [41,46,47].

In 2012, Konstantin Yu. Bliokh et al. provided an exhaustive introduction to transverse OAM [41], which expanded the concept of intrinsic OAM and optical vortices to polychromatic states in space-time. This work was done based on the assumption that polarisation states can be neglected. The visualisation of the spatiotemporal characteristics of the transversely moving Bessel pulsed beam is displayed in Figure 1.9. Panel (a) shows its spectrum depicted on the surface of the light cone in the $(\omega,\ k_x,\ k_y)$ space, demonstrating the creation of a vortex loop when projected onto the$(\omega,\ k_y)$ plane. Panel (b) illustrates the transversely moving Bessel pulsed beam's real-space intensity and phase distribution evolution in the (t, y) plane, with varying propagation position [41].

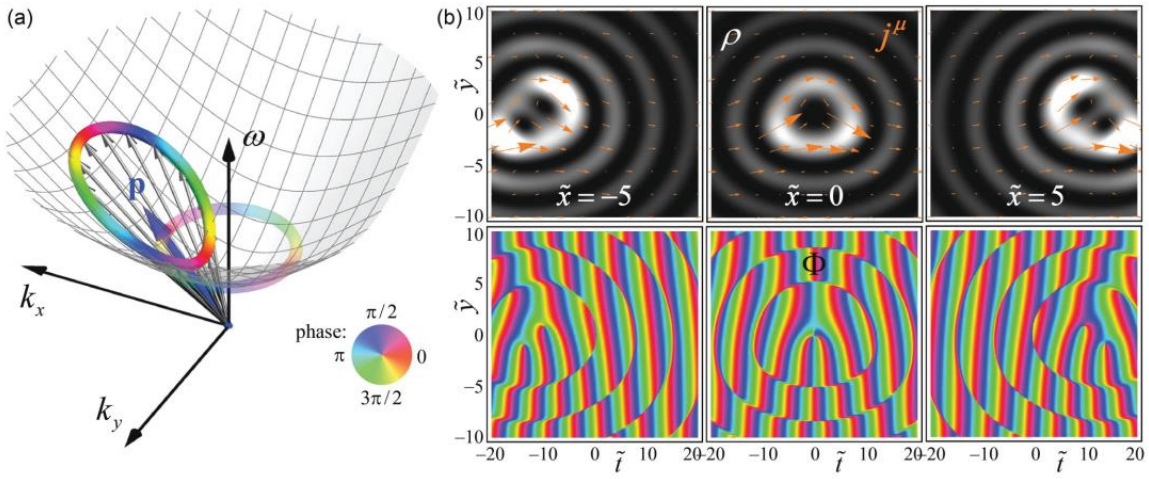

Figure 1.9 (a) shows a spatiotemporal spectrum for a transversely moving Bessel pulsed beam, represented on the surface of the light cone within the $(\omega,\ k_x,\ k_y)$ space, revealing the formation of a vortex loop when projected onto the $(\omega,\ k_y)$ plane. The colormap at the bottom right corner of the spectrum depicts the phase dislocation. (b) shows a schematic of the spatiotemporal characteristics of the transversely moving Bessel pulsed beam. Real-space evolution is presented through distributions in the (t, y) plane at different positions, and the corresponding phase distributions are shown below [41].

Recently, there have been significant advances in experimental research [48, 49, 50] focusing on STOVs that carry transverse OAM. The emergence of these pulses is expected to bring forth innovative geometries and functionalities to vortex states, expanding their applications into the field of spatiotemporal dynamics and ultrafast processes. Figure 1.10 shows the 3D profile of a spatiotemporal optical vortex carrying transverse OAM [51].

Following the method for studying optical pulses shown in section 1.2.3.1, the expression of the STOV carrying transverse OAM in polar coordinates of x-z domain can be obtained:

$$\begin{aligned}\Psi(r,\phi;t) &= \iiint dk_r d\varphi d\Delta\omega\, k_r \frac{1}{2\pi}\sum_{\ell=-\infty}^{\infty} \tilde{\psi}(k_r;\Delta\omega)\, e^{i\ell\varphi} e^{ik_r r cos(\phi-\varphi)} e^{-ik_0 r cos\phi} e^{-i\Delta\omega t} \\ &= \sum_{\ell=-\infty}^{\infty} e^{i\ell\phi} e^{-ik_0 r cos\phi} \iint dk_r d\Delta\omega\, k_r\, \tilde{\psi}(k_r;\Delta\omega) J_\ell(k_r r) e^{-i\Delta\omega t}\end{aligned} \tag{1.49}$$

Eq. (1.49) will be elaborated and explained in detail in Chapter 5. Please refer to section 5.2. The formula for the quantum number (or topological charge (TC)) of the transverse OAM ($tOAM$) is shown in Eq. (1.50) [51].

$$TC\ of\ tOAM = \frac{\int \boldsymbol{r} \times Im[\Psi^* \nabla \Psi] dV}{\int \Psi^* \Psi\, dV} = \ell \tag{1.50}$$

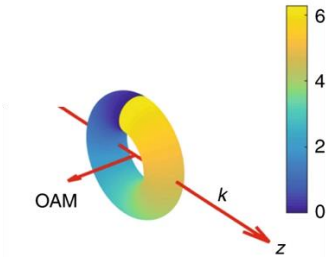

Figure 1.10 depicts the 3D profile of a STOV carrying transverse OAM. The colour bar shows the phase [51].

1.2.4 Optical Sensing

Light has rich physical properties that can be measured, for example: obtaining light power with a power meter [52]; measuring polarisation states with polarimeters [53]; generating 2D maps of intensity distribution of light with imagers [54]; and determining the spectral composition of light with a spectrometer [55]. In an optical sensing process, the device or hardware captures and transduces physical properties of light into usable information. Most of the time, the definition of optical sensing is driven by application perspectives, and there are no uniform descriptions of it.

Optical sensing plays a crucial role in various areas like consumer electronics, industrial sensing, and automotive applications. These scenarios include 3D biometric security [56], industrial measurement [57] and detection applications [58], as well as autonomous driving and light detection and ranging (LiDAR) sensor [59], among others. A variety of sensing technologies can be used in sensing processes, such as structured light [60, 61], time-of-flight [62, 63, 64,65], and self-mixing interference [66, 67, 68].

The LiDAR sensor is used to determine distances by directing a laser at an object or surface and measuring the time it takes for the reflected light to return to the receiver. It can be categorized into the two schemes: pulsed time of flight (TOF) [69, 70] and amplitude-modulated continuous wave (AMCW) TOF [71, 72]. Additionally, another sensing scheme named frequency-modulated continuous wave (FMCW) is also commonly used in LiDAR. By analysing the beat signal between the emitted and reflected frequency-modulated optical signals, both the distance and the velocity of a moving object can be measured [73, 74].

Chapter 2 Geometric Representation of Vector Vortex Beams: The Total Angular Momentum-Conserving Poincaré Sphere and Its Braid Clusters

This chapter presents the total angular momentum-conserving Poincaré sphere (TAM-C PS), which offers a novel framework for efficiently characterising a wide range of vector vortex beams (VVB). Unlike other types of Poincaré spheres, the TAM-C PS achieves a better balance between generality and validity while also providing a clearer physical interpretation. By linking the poles of different spheres, the study also introduces two distinct categories of TAM-C PS braid clusters, enabling the representation of various Poincaré spheres within a unified framework. The Poincaré spheres family includes the classical, higher-order, hybrid-order, Poincaré sphere with orbital angular momentum, and TAM-C PS. This is the first clear and unified approach to expressing multiple Poincaré spheres within a single framework. The TAM-C PS and its braid clusters can be employed to guide the generation of targeted VVB, offer a geometric description for optical field evolutions, and calculate the geometric phase of optical cyclic evolution.

2.1 Introduction

Light is composed of many photons that are absorbed and emitted by atomic systems as electromagnetic radiation. This property classifies light as an electromagnetic wave [75]. An electromagnetic wave can be defined and described by a vector field, which contains two degrees of freedom (DoF): spatial DoF and a polarisation DoF [76]. In recent years, both DoF have garnered significant attention and have been studied and applied in various fields. For instance, polarisation DoF have found applications in tight focusing of light beams [77], particle acceleration [78], vectoral Doppler metrology for detecting universal motion vectors [79], nonlinear optics [80], and classical entanglement [81]. The spatial DoF of light can be controlled by manipulating the OAM. This has led to what we now refer to as structured light [82]. Structured light has been applied in areas such as imaging and microscopy [83], optical trapping [84-85], and quantum computing [86], to name a few. By controlling these two DoF of light, we can generate a variety of more complex optical fields. A concise method to characterise and describe these complex optical fields is highly desired. The Poincaré sphere is a powerful and practical tool, providing a descriptive framework for these complex optical fields, characterising their physical properties, and finding broad applications in engineering.

The Poincaré sphere as a representation within the optical context of Bloch spheres shown in Figure 2.1 [87]. Different polarisation states of optical fields can be identified and represented using this framework. The right and left circular polarisation states define its north and south poles, creating a pair of orthogonal eigenstates [88]. Any additional pure-state field can be superposed by employing complex linear combinations of these two fundamental basis vectors. This implies that four real numbers are needed to describe such a pure-state field [88]. However, only the relative phase between the two orthogonal bases has physical significance. Therefore, three real numbers are sufficient to characterise these pure-state fields, leading to the construction of a three-dimensional Poincaré sphere. The relative phases of orthogonal bases are represented by two angles, β and φ, which are mapped to the polar and the azimuthal angle of the Poincaré sphere, respectively. Consequently, different polarisation states of light beams can be mapped onto the Poincaré sphere, providing a geometric model that offers an intuitive and insightful representation framework for complex optical fields' polarisations, leading to several applications [89]. By defining the Stokes parameters S_0, S_1, S_2, S_3, we can geometrically project arbitrary pure states, as represented in Figure 2.1, onto the Poincaré sphere. The parameter S_0 represents the normalised optical field intensity, and it is reflected in the Poincaré sphere as the sphere's radius. The three parameters S_1^t, S_2^t and S_3^t are the unit sphere coordinates defining three mutually orthogonal axes for the Poincaré spheres. Subsequently, any pure-state field can be mapped onto a sphere. The Stokes parameters I, Q, U, and V offer an alternative representation of the polarisation state, which proves experimentally convenient as each parameter corresponds to a sum or difference of measurable intensities.

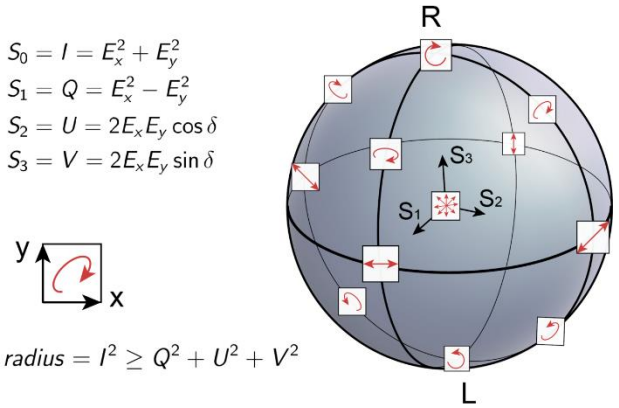

Figure 2.1 shows a schematic of the Poincaré spheres [87].

The classical Poincaré sphere (Classical-PS) was introduced in 1892 as a representation within the optical context of Bloch spheres. Various polarisation states of light fields can be clearly characterised on it [88]. Its north and south poles are defined as left and right circular polarisations, which form an orthogonal basis. Any other pure-state field can be constructed

through complex linear combinations of these two basis vectors. However, the Classical-PS cannot describe higher-order solutions of Maxwell's vector wave equation.

In 2011, Giovanni et al. developed a new type of Poincaré sphere called the higher-order Poincaré sphere (HOPS) by extending the complex Jones vector basis of plane-wave polarisation [90]; Unlike the eigenmodes corresponding to the two poles of the Classical-PS, HOPS introduces orbital states of equal magnitude but opposite handedness in its expressions. It should be noted that different OAM states are orthogonal to each other, making OAM states a complete orthogonal basis, allowing any light field to be decomposed on this basis. Therefore, the introduction of OAM still ensures the orthogonality of the eigenmodes. In this way, the introduction of spatial DoF is achieved, and a special type of light beam, the cylindrical vector beam, can be characterised within the framework of the Poincaré sphere.

In 2015, Yi et al. introduced the hybrid-order Poincaré sphere (HyOPS), which shares a similar definition with HOPS [91]; Unlike HOPS, HyOPS allows arbitrary selection of the state value and sign of OAM. The green dashed lines in Figure 2.2 illustrate this modified definition. This makes HyOPS a more generalised Poincaré sphere, capable of expressing VVB.

A brief overview of the development process of Poincaré spheres is provided in Figure 2.2 (a–c), depicting Classical-PS, HOPS, and HyOPS, respectively. The dashed lines connecting the spheres represent the evolutionary progression of the definition of each generation of Poincaré spheres relative to the Classical-PS. It should be noted that HOPS has two types, as shown in subgraphs 2.2 (b1) and (b2). Subgraph 2.2 (b1) illustrates the case where the handedness of OAM and SAM is identical, whereas subgraph 2.2 (b2) depicts the scenario where their handedness is opposite. Consequently, the polarisations of the optical fields represented by the spheres in subgraphs 2.2 (b1) and (b2) are different. Subgraph (c2) represents an ill-defined HyOPS, which will be discussed in the next subsection.

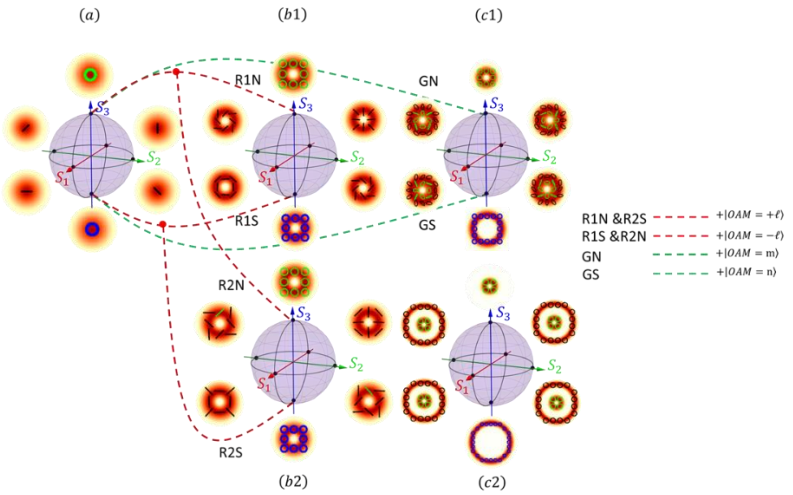

Figure 2.2 This diagram serves as a schematic representation of the evolutionary development process of Poincaré spheres. It illustrates the progression of Poincaré spheres from left to right, beginning with the classical Poincaré sphere (Classical-PS); the higher-order Poincaré sphere (HOPS) for the first and second types; and the hybrid-order Poincaré sphere (HyOPS). The dotted line represents the changes in the eigenstate definition of the new-generation Poincaré spheres compared to Classical-PS, as elaborated upon in the introduction. In the legend, "R" and "G" represent red and green, respectively; "N" and "S" mean the north and south poles of the spheres. (a) Classical-PS. (b1) HOPS for the first type, where the SAM and OAM have the same handedness. (b2) HOPS for the second type, where the SAM and OAM have opposite handedness. (c1) HyOPS. (c2) The ill-defined HyOPS.

By extending the complex Jones vector basis of plane-wave polarisation, the introduction of spatial DoF to Poincaré spheres is achieved. However, HOPS do not incorporate an important type of light beam: VVB, into the Poincaré sphere framework.

Compared to HOPS, the HyOPS allows arbitrary selection of the state value and sign of OAM. Consequently, VVB can be expressed in the Poincaré sphere framework, making HyOPS a more generalised Poincaré sphere. However, it should be noted that some HyOPS are ill-defined. This issue arises from the geometric mismatch of the eigenmode, leading to a contradiction: the optical fields represented based on the definition of eigenstates by HyOPS sometimes do not satisfy the definition of Stokes parameters, as shown in subgraph 2.2 (c2). It can be observed that the radii of the eigenmodes corresponding to the two poles of the sphere are significantly different. Because the beam radius (defined at the point of maximum intensity, relative to the beam centre) is directly proportional to the magnitude of the TC, $|\ell|$. (Corresponding to the modulus of the OAM eigenvalue), i.e.,$r_{max} \propto |\ell|$. Therefore, the geometric size of beams carrying different OAM values will differ, especially when there is a substantial difference between the TC values carried by the two eigenmodes. This significant size mismatch in the eigenstates results in

the outcome shown in subfigure 2.2 (c2), which is inconsistent with the definition of Stokes parameters.

Consequently, it is evident that the existing frameworks for representing VVB based on Poincaré spheres are not sufficiently comprehensive. Furthermore, the multitude of Poincaré sphere representation frameworks lacks an integrated system, making it challenging for researchers to immediately grasp due to the diverse and intricate definitions and their respective scopes. HOPS and HyOPS, also known as higher-order Poincaré spheres, introduce spatial DoF. The eigenmodes of these higher-order Poincaré spheres, defined simply by incorporating OAM based on demand, lack consideration from a more fundamental physical perspective.

2.2 Method

In this work, vortex beams are monochromatic paraxial approximated. This refers to a class of well-collimated beams in which [92]. Within this context, the quantum number for total angular momentum (TAM: t) can be expressed as the sum of the quantum numbers for spin angular momentum (SAM: σ) and orbital angular momentum (OAM: ℓ) [93]. However, it's important to clarify that the value of the TAM cannot always be straightforwardly defined as the sum of the value of SAM and OAM. This is particularly true in cases involving tight focusing, where these two types of angular momentum may not be distinctly separable within an optical field [94, 95]. Nevertheless, for monochromatic beams under paraxial approximation, these two inherently different forms of angular momenta can be well-distinguished: SAM is defined by the dynamic rotation of electric and magnetic fields around the direction of propagation and is described by a characteristic phase factor $e^{i\sigma\Phi}$, where σ is the spin quantum number, taking values of +1 or -1; OAM is defined by the dynamic rotation of light rays around the central axis of the beam and is described by a characteristic phase factor $e^{i\ell\varphi}$, where ℓ is the topological charge (TC) number, taking values of 0 or any integer. It is worth noting that SAM and OAM are related to the circular polarisation of the electric field and the helical wave front of the beam [96], respectively, in the case of paraxial beams. Furthermore, both azimuthal angles ϕ and φ are defined in the transverse plane (e.g., x-y plane) orthogonal to the direction of light propagation (e.g., z-direction), with their values ranging from $[0, 2\pi]$. Thus, the definitions of these two azimuthal angles are equivalent, allowing the phase factor of the vortex beams to be expressed as $e^{i(\sigma+\ell)\Phi}$. Consequently, the value of TAM is given by $(\sigma + \ell)\hbar$ per photon. This conclusion can also be verified using group theory, where infinitesimal operators provide the starting point for defining the corresponding groups. SAM characterises the intrinsic polarisation DoF, while OAM characterises the orbital DoF [97]. Since these two quantities are generated in different spaces, their commutation relation can be expressed as [98]

$$[\boldsymbol{S}, \boldsymbol{L}] = 0. \tag{2.1}$$

When operators $\hat{S}$ and $\hat{L}$ act together on one system, the corresponding action of the infinitesimal rotation can be expressed as

$$\begin{aligned}&\left[1 - i\left(\frac{\boldsymbol{S}\cdot\hat{\boldsymbol{n}}}{\hbar}\right)d\phi\right] \otimes \left[1 - i\left(\frac{\boldsymbol{L}\cdot\hat{\boldsymbol{n}}}{\hbar}\right)d\phi\right] \\ &= 1 - \frac{i(\boldsymbol{S}\otimes 1 + 1\otimes\boldsymbol{L})\cdot\hat{\boldsymbol{n}}d\phi}{\hbar}.\end{aligned} \tag{2.2}$$

Then the TAM can be defined as

$$\boldsymbol{J} \equiv \boldsymbol{S}\otimes 1 + 1\otimes\boldsymbol{L}. \tag{2.3}$$

The 1 of $\boldsymbol{S}\otimes 1$ in Eq. (2.3) represents a unit position operator in orbital space, and that of $1\otimes\boldsymbol{L}$ represents a unit operator in spin space. Eq. (2.3) can be expressed in a more concise form as

$$\boldsymbol{J} \equiv \boldsymbol{S} + \boldsymbol{L}. \tag{2.4}$$

Consequently, the value of the vortex beam's TAM is $t = (\sigma + \ell)\hbar$. An arbitrary pure state can be built through the complex linear combination of two eigenstates, represented as the North and South poles on the Poincaré sphere. Accordingly, the mathematical expression for a vortex beam under paraxial approximation corresponding to a point on the TAM-C PS is formulated as follows:

$$|\psi_t\rangle = \psi_N^{\ell_N}\left|N_P^{\ell_N}\right\rangle + \psi_S^{\ell_S}\left|S_P^{\ell_S}\right\rangle, \tag{2.5}$$

$$\left|N_P^{\ell_N}\right\rangle = \frac{1}{\sqrt{2}}e^{-i\ell_N\varphi}\left(\hat{e}_x - i\hat{e}_y\right),$$

$$\left|S_P^{\ell_S}\right\rangle = \frac{1}{\sqrt{2}}e^{-i\ell_S\varphi}\left(\hat{e}_x + i\hat{e}_y\right),$$

$$\psi_N^{\ell_N} = sin\,(\beta/2)\,,$$

$$\psi_S^{\ell_S} = cos\,(\beta/2)\,e^{+i\phi}.$$

We use the notation $|\psi_t\rangle$ to represent a monochromatic beam under paraxial approximation corresponding to a point with TAM $= t\hbar$ on the TAM-C PS. The symbols $\left|N_P^{\ell_N}\right\rangle$ and $\left|S_P^{\ell_S}\right\rangle$ represent a pair of eigenstates located on the North and South poles of the TAM-C PS, respectively. Specifically, these eigenstates represent right-circularly and left-circularly polarised vortex beams with OAM quantified as $\ell_N\hbar$, $\ell_S\hbar$, respectively. The symbols $\psi_N^{\ell_N}$, $\psi_N^{\ell_S}$ represent the coefficients of these two eigenstates, which are defined by relative intensity (variables $\beta \in [0, \pi]$) and relative phase ($\phi \in [0, 2\pi]$).

Based on the requirement of TAM conservation: The TAM (denoted as $t\hbar$) of light beams corresponding to points on the same spherical surface should be the same. The polarisation state

at the North pole is designated as right-handed circular polarisation ($\sigma = +1$), while the state at the South pole is established as left-handed circular polarisation ($\sigma = -1$). As a result, the TC of the OAM at the North pole is $\ell_N = t - 1$, and at the South pole, it is $\ell_s = t + 1$. The OAM at the South pole is greater than that at the North pole by $2\hbar$.

By defining the Stokes parameters, we can geometrically project arbitrary pure states, as represented by Eq. (2.5), onto the TAM-C PS. The Stokes parameters for the TAM-C PS are specified as outlined in Eq. (2.6) - (2.9) [99].:

$$S_0 = \left|\left\langle N_P^{\ell_N} \middle| \psi_t \right\rangle\right|^2 + \left|\left\langle S_P^{\ell_S} \middle| \psi_t \right\rangle\right|^2 = \left|\psi_N^{\ell_N}\right|^2 + \left|\psi_S^{\ell_S}\right|^2 = 1, \tag{2.6}$$

$$S_1 = 2Re(\left\langle N_P^{\ell_N} \middle| \psi_t \right\rangle^* \left\langle S_P^{\ell_S} \middle| \psi_t \right\rangle) = sin\,\beta\, cos\,\phi\,, \tag{2.7}$$

$$S_2 = 2Im(\left\langle N_P^{\ell_N} \middle| \psi_t \right\rangle^* \left\langle S_P^{\ell_S} \middle| \psi_t \right\rangle) = sin\,\beta\, sin\,\phi\,, \tag{2.8}$$

$$S_3 = \left|\left\langle N_P^{\ell_N} \middle| \psi_t \right\rangle\right|^2 - \left|\left\langle S_P^{\ell_S} \middle| \psi_t \right\rangle\right|^2 = cos\,\beta\,. \tag{2.9}$$

The parameter S_0 represents the normalised optical field intensity, and it is reflected in the TAM-C PS as the sphere's radius. By examining the expressions for S_1, $S_2$and S_3 (Eq. (2.7) -(2,9)), we can see that these three parameters are precisely the expressions for the unit sphere coordinates. Therefore, using the parameters S_1, $S_2$and S_3, we define three mutually orthogonal axes for the TAM-C PS. Subsequently, any pure-state field can be mapped onto the sphere.

2.3 Results

2.3.1 Total Angular Momentum-Conserving Poincaré Sphere and Its Properties

In the previous section, we defined the Stokes parameters of TAM-C PS. With the help of S1, S2, and S3, we can establish a three-dimensional coordinate system illustrated in Figure 2.3, which also shows a TAM-C PS with TAM $= 5\hbar$. The intensity and polarisation distributions of pure states in all figures are the results of numerical calculations performed using MATLAB. The axes coloured in red, green, and blue correspond to S_1, $S_2$and S_3 respectively; the sphere's radius is defined by S_0. Additionally, Figure 2.3 displays the intensity and polarisation distribution of four types of beams. These beams are represented by two pairs of antipodal points on the sphere's equator. Variations in intensity are illustrated through gradations in colour, while the polarisation attributes of the fields are conveyed by the form and orientation of lines. Because of the conservation of TAM, for the sphere depicted in Figure 2.3, eigenmodes corresponding to its North pole ($\left|N_{\ell_N}\right\rangle$)) have SAM and OAM values of $\sigma = +1$, $\ell = +4$, respectively, while those

corresponding to its South pole ($|S_{\ell_S}\rangle$) have SAM and OAM values of $\sigma = -1$ and $\ell = +6$, respectively.

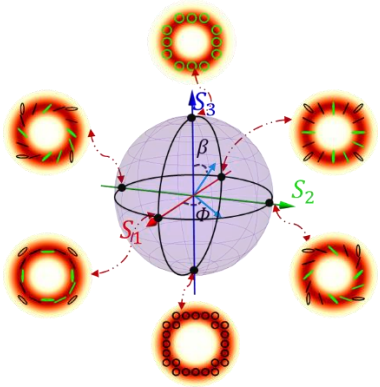

Figure 2.3 shows a schematic for the total angular momentum-conserving Poincaré sphere (TAM-C PS) with TAM$= +5\hbar$. Beams represented by the poles are circularly polarised vortex beams and those depicted by points on the equator are cylindrically polarised vortex beams, a specific category of VVB.

According to Eq. (2.5), VVB represented on the equator ($\beta = \pi/2$) exhibit cylindrical polarisation characteristics with SAM=$0\hbar$ and OAM=$5\hbar$. Additionally, points not on the two poles and equator correspond to elliptically polarised vortex beams with TAM=$5\hbar$. This is a direct consequence of TAM conservation. Using MATLAB, we computed the wavefront phase, intensity, and polarisation distribution of a specific equatorial light field represented by the TAM-C PS through the superposition of eigenstates, as shown in Figure 2.4.

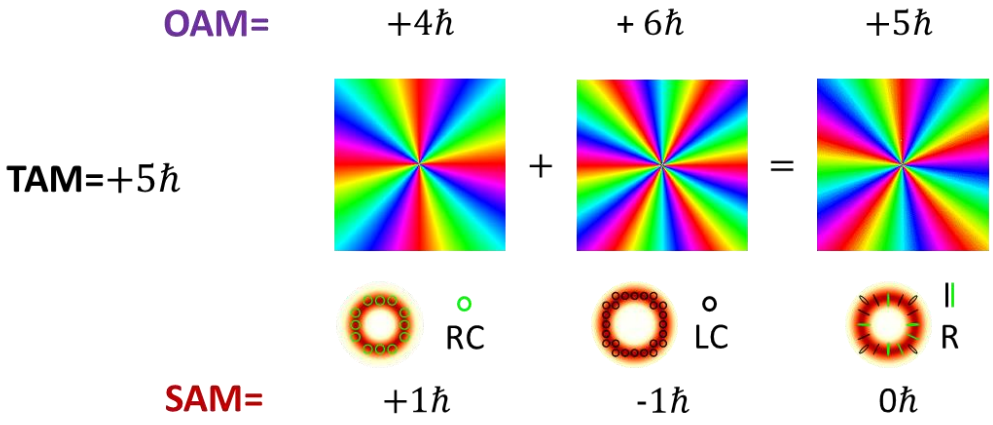

Figure 2.4 illustrates the eigenstates superposition process on the TAM-C with TAM = $5\hbar$ based on MATLAB computational results. In this example, $\beta = \pi/2$ and $\phi = \pi$. The phase distributions of the wavefront of two eigenstates and the resulting beam are placed at the top of the image; the intensity and polarisation distribution of the two eigenstates and the resulting beam are placed at the bottom of the image. Circular lines represent circular polarisation states, with green indicating right-circular

polarisation (RC) and black indicating left-circular polarisation (LC); the green and black lines indicate the radially polarised state (R) of the resulting beam.

From Figure 2.4, we can observe that the wavefront phase of the resulting beam repeats 5 times, indicating that the beam possesses an OAM with a value of $5\hbar$. The calculated result matches the prediction of OAM=$5\hbar$ based on Eq. (2.5). At the bottom of Figure 2.4, the red doughnut shape represents the intensity distribution, and the green and black lines indicate the polarisation state of the resulting beam which matches our expected radial polarisation state.

2.3.2 Total Angular Momentum-Conserving Poincaré Sphere Clusters

This part presents the structure and properties of TAM-C PS braid clusters. Noether's theorem states that each conservation law corresponds to a fundamental symmetry (invariance) within the field of physics, with the conservation of angular momentum being associated with rotational symmetry in a system [100]. This implies that each TAM-C PS we build inherently represents a rotationally symmetric system. By connecting spheres with different TAM values, we can describe the non-conservation of TAM or non-rotationally symmetric systems. This inspires the idea of using two TAM-C PSs to represent Classical-PS, HOPS, and PS-OAM spheres. Figure 2.5 shows how Classical-PS, HOPS, and PS-OAM can be represented by two TAM-C PSs.

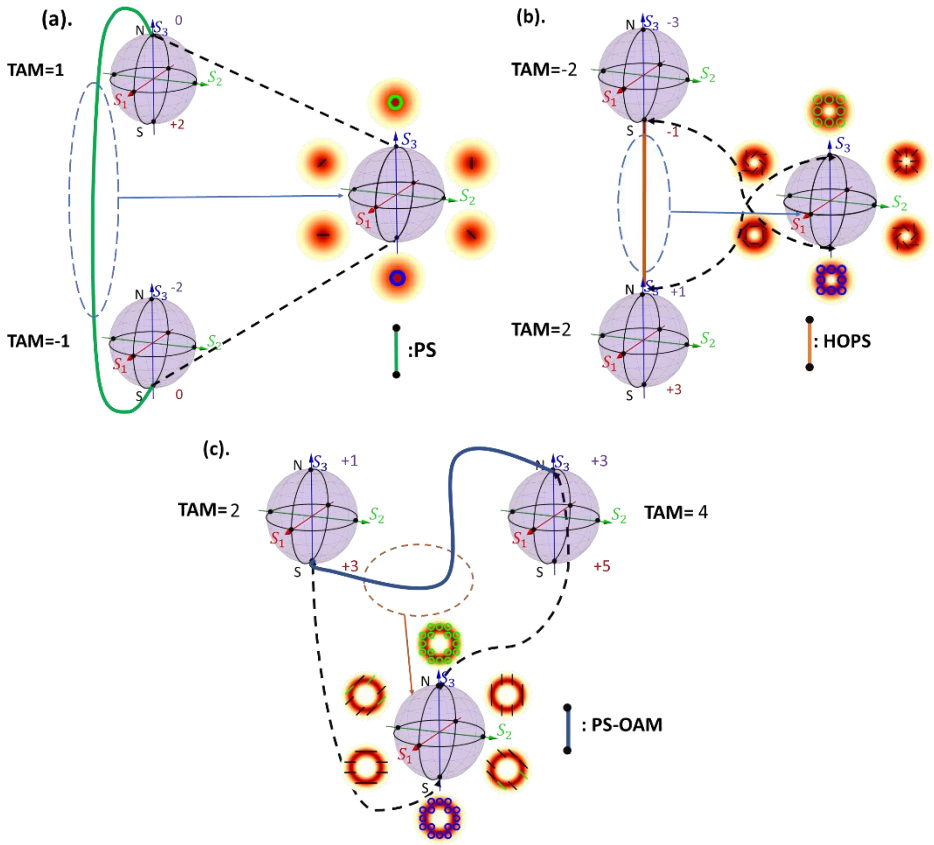

Figure 2.5 A schematic diagram illustrates how Classical-PS, HOPS, and PS-OAM can be represented by two TAM-C PSs. In particular, (a) The Classical-PS can be built from

two TAM-C PSs with TAM$= +1\hbar$ and TAM$= -1\hbar$; (b) The HOPS ($|\ell| = 1$) can be represented by two TAM-C PSs with TAM$= -2\hbar$ and TAM$= +2\hbar$; (c) The PS-OAM ($|\ell| = 2$) can be represented by two TAM-C PSs with TAM$= +2\hbar$ and TAM$= +4\hbar$. In all cases, the South pole and North pole of the TAM-C PSs correspond to left-circularly polarisation ($\sigma = -1$) and right-circularly polarisation ($\sigma = +1$), respectively. The numbers near the two poles indicate the OAM values. It is worth noting that HyOPS was not included in this cluster, as all spheres in the cluster belonged to the HyOPS family.

Based on the definitions and properties of the existing Poincaré spheres: Classical-PS has no OAM DoF, the HOPS requires opposite-signed OAM at its two poles, and the PS-OAM requires identical OAM at its two poles. We can redefine them by connecting the North pole of one TAM-C PS to the South pole of another, thereby establishing a new set of poles. This approach allows for the characterisation of Classical-PS, HOPS, and PS-OAM within the framework of TAM-C PS, as illustrated in Figure 2.5. It is important to note that HyOPS does not need to be re-built because all Poincaré spheres discussed in this paper fall under the category of HyOPS. Based on these conclusions, we built a braid cluster that can contain the Poincaré spheres mentioned in this study. Figures 2.6 (a) and 2.6 (b) are two types of braid clusters. Because there are two categories of HOPS due to the different definitions of their values of OAM of their eigenstates (as explained in the introduction), to comprehensively cover all possible cases, we built these two clusters. The values of TAM can be divided into three types: TAM$= 0\hbar$, $> 0\hbar$ and $< 0\hbar$. Therefore, we classify TAM-C PS into three types. The arrangement of these three types of spheres is shown in Figure 2.6.

Table 2.1 A table of angular momentum (AM) carried by the eigenstates of different types of Poincaré Spheres (PS); “N” and “S”: the eigenstates represented by the North and South Poles on the sphere; SAM: the spin angular momentum related to circular polarization states (+1: right; -1: left); OAM: the orbital angular momentum (L, L_N, L_S, and J: they can be taken as 0 or any integer). TAM, total angular momentum (TAM=SAM+OAM); Because HyOPS allows for the selection of any value of OAM, the notations “L_N” and “L_S” represent the arbitrary value of the OAM of the eigenstate; For TAM-PS, optical fields represented by points on it have the same value of TAM, so we use the symbol “J” to represent the value of TAM of optical fields represented by a TAM-PS.

AM \ PS		Classical PS	HOPS		PS-OAM	HyOPS	TAM-PS
SAM	N	+1	+1		+1	+1	+1
	S	-1	-1		-1	-1	-1
OAM	N	0	+L	-L	L	L_N	J-1
	S	0	-L	+L	L	L_S	J+1
TAM	N	+1	+L+1	-L+1	L+1	L_N+1	J
	S	-1	-L-1	+L-1	L-1	L_S-1	J

Panel (a) and panel (b) of Figure 2.6 illustrate two types of TAM-C PS braid clusters. In panel (a), the spheres with TAM $> 0\hbar$ are placed at the top of the image; spheres with TAM $< 0\hbar$ are positioned at the bottom, and spheres with TAM $= 0\hbar$ are placed slightly to the left in the middle of the two types of spheres. In contrast, in panel (b), the second type of cluster inverts the relative positions of spheres with TAM $> 0\hbar$ and TAM $< 0\hbar$. The green, orange, and dark blue lines in the figure represent Classical-PS, HOPS, and PS-OAM, respectively.

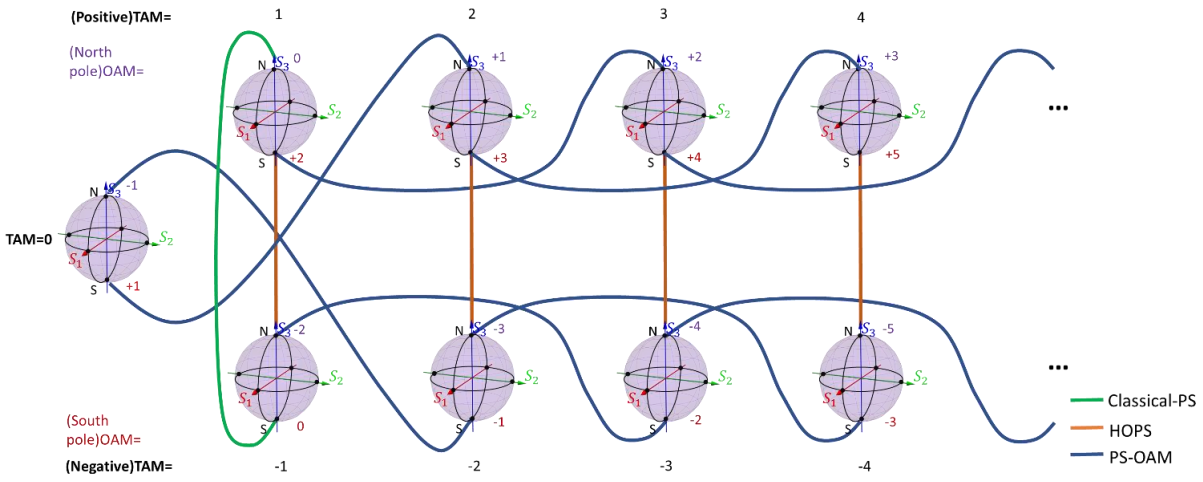

(a)

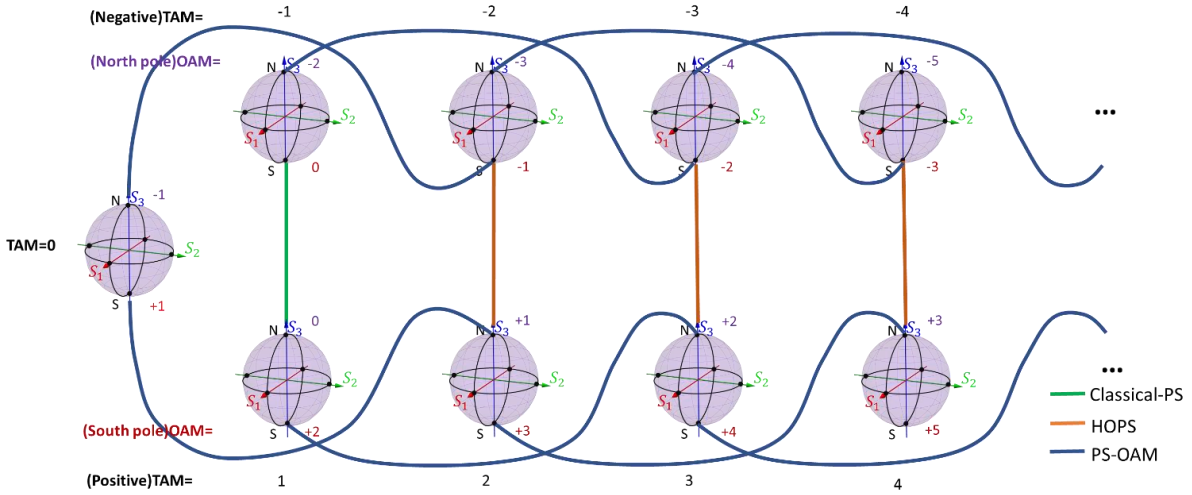

(b)

Figure 2.6 (a) shows the TAM-C PS braid cluster for the first type. The spheres with TAM $> 0\hbar$ are placed in the top row, the sphere with TAM $< 0\hbar$ is placed in the bottom row, and the TAM $= 0\hbar$ sphere is located between the two rows. The TAM values are indicated by black numbers. The North pole of the sphere, labelled N, corresponds to a circularly polarised vortex beam $\sigma = +1$, and the value of the OAM is indicated by purple numbers. The South pole of the sphere, labelled S, corresponds to a circularly polarised vortex beam $\sigma = -1$, and the value of the OAM is indicated by red numbers; (b) illustrates the TAM-C PS braid cluster for the second type. The spheres with TAM $< 0\hbar$ are placed in the top row, the sphere with TAM $> 0\hbar$ is placed in the bottom row, and the TAM $= 0\hbar$ sphere is located between the two rows. The TAM values are indicated by black numbers. The North pole of the sphere, labelled N, corresponds to a circularly polarised beam $\sigma = +1$, and the value of the OAM is indicated by purple numbers. The South pole of the sphere, labelled S, corresponds to a circularly polarised vortex beam $\sigma = -1$, and the value of the OAM is indicated by red numbers.

2.4 Discussion

The followings are some important features of the TAM-C PS and its braid clusters:

1. On one TAM-C PS, the value of OAM of the beam represented by its North pole is always $2\hbar$ less than that of the beam represented by its South pole.
2. In panel (a) of Figure 2.6, all HOPS belong to the second category. Notably, the TAM-C PS sphere with TAM$= 0\hbar$ is equivalent to the HOPS with poles carrying $|1\hbar|$ OAM.
3. In panel (b) of Figure 2.6, nearly all HOPS belong to the first category, except for the TAM-C PS with TAM$= 0\hbar$ (which, as mentioned in the last point, is equivalent to the second category of HOPS with poles carrying $|1\hbar|$ OAM).
4. The PS-OAM sphere is built by linking the North pole of one TAM-C PS with the South pole of another sphere, both having the same OAM value. This implies that the orbital states of the two eigenmodes represented by the North and South poles of the PS-OAM sphere are not orthogonal. Despite the non-orthogonality of the orbital states, the polarisation states of the two poles remain orthogonal to each other. Therefore, the PS-OAM sphere can be considered as a special type of Classical-PS with a specific OAM state.
5. Panel (a) and panel (b) of Figure 2.7 illustrate two types of light beam evolution paths within the braid clusters. In panel (a), the black line depicts a closed path starting from the North pole, passing through the South pole, and returning to the North pole. This closed path can be further reduced to the collection of blue lines and eventually to a single point. In contrast, the solid line in panel (b) cannot be reduced to a single point like the closed curve in panel (a). Inspired by this geometric property, we attempt to find its corresponding physical significance. These two types of paths represent two distinct evolution processes. The first type (panel (a)) corresponds to the TAM conservation process of a rotationally symmetric system, as the entire optical field evolution process occurs on the same TAM-C PS. Through calculation, it can be shown that the geometric phase associated with this cyclic evolution process is always zero (details of the calculation will be presented later). In contrast, the second type of optical field evolution path represents the TAM non-conservation process, corresponding to a rotational symmetry-breaking system, and the geometric phase generated by this process is generally non-zero.

When a pure state $\psi(\boldsymbol{R})$ undergoes a cyclic optical evolution within the parameter space $\boldsymbol{R}$, returning to its initial state, an additional phase (geometric phase) emerges in addition to the dynamic phase. This geometric phase is given by the equation [101], [102]:

$$\chi(C) = -\iint_C d\boldsymbol{S} \cdot \boldsymbol{V}(\boldsymbol{R}) \tag{2.10}$$

$\boldsymbol{V}(\boldsymbol{R})$ is the Berry curvature, defined as:

$$\boldsymbol{V}(\boldsymbol{R}) = -\nabla_{\boldsymbol{R}} \times \boldsymbol{A}_n(\boldsymbol{R}) \tag{2.11}$$

$\boldsymbol{A}_n(\boldsymbol{R})$ is named the Berry connection, as given in [102]:

$$\boldsymbol{A}_n(\boldsymbol{R}) = i\langle\psi(\boldsymbol{R})|\nabla_{\boldsymbol{R}}|\psi(\boldsymbol{R})\rangle \tag{2.12}$$

Where $\psi(\boldsymbol{R})$ is the pure-state which is represented by a point on the TAM-C PS. And Eq. (2.13) is the expression for $\psi(\boldsymbol{R})$ in polar coordinates:

$$\psi(\boldsymbol{R}) = \frac{1}{\sqrt{2}} sin\frac{\beta}{2} e^{-i\left[\frac{\Phi}{2}(\ell_N+1)\right]}\left(\hat{e}_r - j\hat{e}_\varphi\right) + \frac{1}{\sqrt{2}} cos\frac{\beta}{2} e^{-i\left[\frac{\Phi}{2}(\ell_S-1)\right]}\left(\hat{e}_r + j\hat{e}_\varphi\right) \tag{2.13}$$

where $(\hat{e}_r, \hat{e}_\varphi)$ is a set of orthogonal unit vectors for states of polarisation in polar coordinates. The transformation relationship between the two bases $(\hat{e}_r, \hat{e}_\varphi)$ and $(\hat{e}_x, \hat{e}_y)$ is:

$$\hat{e}_x = \cos\varphi\, \hat{e}_r - \sin\varphi\, \hat{e}_\varphi \tag{2.14}$$

$$\hat{e}_y = \sin\varphi\, \hat{e}_r + \cos\varphi\, \hat{e}_\varphi$$

And then, we have

$$\hat{e}_x + i\hat{e}_y = \cos\varphi\, \hat{e}_r - \sin\varphi\, \hat{e}_\varphi + i\sin\varphi\, \hat{e}_r + i\cos\varphi\, \hat{e}_\varphi = e^{i\varphi}\left(\hat{e}_r + j\hat{e}_\varphi\right) \tag{2.15}$$

$$\hat{e}_x - i\hat{e}_y = \cos\varphi\, \hat{e}_r - \sin\varphi\, \hat{e}_\varphi - i\sin\varphi\, \hat{e}_r - i\cos\varphi\, \hat{e}_\varphi = e^{-i\varphi}(\hat{e}_r - j\hat{e}_\varphi)$$

the relation of $\varphi \rightarrow \Phi/2$ is a consequence of transformation between the physical SU (2) space of the light beam and the topological SO (3) space of the Poincaré sphere. Notations β and Φ denote the polar and azimuthal angles of the Poincaré sphere, respectively.

The Berry connection $\boldsymbol{A}_n(\boldsymbol{R})$ has three components in spherical coordinates, which are $\boldsymbol{A}_\rho$, $\boldsymbol{A}_\beta$, and $\boldsymbol{A}_\Phi$. By substituting Eq. (2.13) into Eq. (2.12), the expressions of these three components can be obtained, as shown below:

$$\boldsymbol{A}_\rho = i\langle\psi(\boldsymbol{R})\big|\partial_\rho\big|\psi(\boldsymbol{R})\rangle = 0 \tag{2.16}$$

$$\boldsymbol{A}_\beta = \frac{i\langle\psi(\boldsymbol{R})\big|\partial_\beta\big|\psi(\boldsymbol{R})\rangle}{\rho} = \frac{1}{2} sin\frac{\beta}{2} cos\frac{\beta}{2}\langle N|N\rangle - \frac{1}{2} sin\frac{\beta}{2} cos\frac{\beta}{2}\langle S|S\rangle = 0$$

$$\boldsymbol{A}_\Phi = \frac{i\langle\psi(\boldsymbol{R})|\partial_\Phi|\psi(\boldsymbol{R})\rangle}{\rho sin\beta} = \frac{1}{4\rho sin\beta}[(1 - cos\beta)(\ell_N + 1) + (1 + \cos\beta)(\ell_S - 1)].$$

Then, by substituting Eq. (2.16) into Eq. (2.11), we can obtain the Berry curvature:

$$\boldsymbol{V}(\boldsymbol{R}) = -\nabla_{\boldsymbol{R}} \times \boldsymbol{A}_n(\boldsymbol{R}) = \boldsymbol{V}_\rho(\boldsymbol{R}) = \frac{\ell_N - \ell_S + 2}{4\rho^2} \tag{2.17}$$

After that, by substituting the Eq. (2.17) into Eq. (2.10), the geometric phase $\chi(C)$ can be calculated:

$$\chi(C) = -\iint_c d\boldsymbol{S} \cdot \boldsymbol{V}(\boldsymbol{R}) = -\frac{\ell_N - \ell_S + 2}{4\rho^2}\Omega \tag{2.18}$$

Here, Ω represents the surface area enclosed by the circuit c on the TAM-C PS. This equation illustrates that the geometric phase is directly proportional to the variation in $(\ell_N - \ell_S + 2)$. Because $(\ell_N - \ell_S + 2)$ equals 0 on the same TAM-C PS (this property has been discussed in the method), both the Berry curvature and the geometric phase become null.

In terms of the breadth of the definitions, HyOPS represents the most generalised form of Poincaré spheres. However, despite this, HyOPS itself has some limitations: it contains some poorly defined cases (as detailed in the introduction), and due to its overly generalised nature, it combines various Poincaré spheres into a single entity, obscuring the distinct characteristics and application premises of individual Poincaré spheres, making it challenging for users to intuitively grasp their differences. Hence, the TAM-C PSs can be regarded as an effective classification method for the HyOPS family. This approach not only filters out poorly defined HyOPS but also provides a concise and intuitive way, i.e., TAM-C PS braid cluster to characterise relationships among different Poincaré spheres. And these braid clusters can help us identify the topological symmetries of a given system and determine the relationships between light fields within the system or between them and light fields in other systems. Consequently, this cluster can be used to geometrically describe the evolution of various VVB. The TAM-C PSs serve as powerful and useful tools in optical research and engineering.

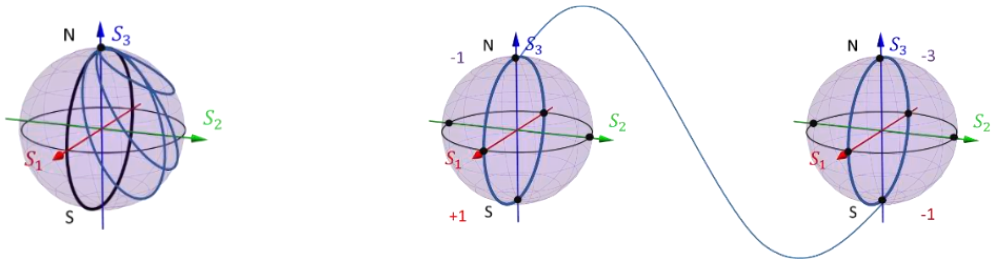

(**a**) (**b**)

Figure 2.7 (a) A schematic diagram for TAM conservation process; (b) A schematic diagram for TAM non-conservation process.

2.5 Conclusion

This study introduces the concept of the conservation of total angular momentum within the framework of the Poincaré sphere, leading to a new type of Poincaré sphere known as the total angular momentum-conserving Poincaré sphere (TAM-C PS). By linking the poles of different TAM-C PSs, we create two categories of TAM-C PS braid clusters. The TAM-C PS and its braid clusters offer a comprehensive framework for the representation and characterisation of these beams, and they can serve as a guide to generate the targeted VVBs as well. Compared to other types of Poincaré spheres, the TAM-C PS achieves a more balanced compromise between generality and practical application.

The TAM-C PS braid clusters include various types of Poincaré spheres, such as the classical Poincaré sphere, higher-order Poincaré sphere, hybrid-order Poincaré sphere, and Poincaré sphere with orbital angular momentum. This approach provides an intuitive and clear representation of the relationships between these different types of spheres. The braid cluster methodology holds significant practical value, including geometrically describing the evolution of optical fields, and calculating the geometric phase for cyclic evolution. The TAM-C PS and its associated braid clusters contribute valuable insights to the field of optics.

Chapter 3 A Method for Analysing Angular Momentum in Monochromatic Vortex Beams under Paraxial Approximation

Please note this chapter is based on collaborative research. The complex amplitude data of optical fields analysed in this part were provided by a collaborative group. Based on the complex amplitude data provided by them, I plotted the intensity distributions and polarisation state distributions of these optical fields. The research methods used in the chapter and the AM spectrum obtained by analysing these fields based on the method are my personal work.

In the research area of meta-surface integrated micro-rings, during the device design and simulation phase, analysing the OAM mode based on simulated results of resultant fields is an unresolved issue. In this chapter, under paraxial approximation, a method for analysing the value of OAM in scalar vortex beams and that of TAM in VVBs is presented. In addition, this work is also expected to be applied to some optical sensing scenarios, such as identifying detecting signals (i.e., vortex beams) from noises by OAM modes, and deducing information about objects interacting with the vortex beam based on changes in OAM modes of signals [11].

3.1 Introduction

The study of analysing OAM modes in scalar vortex beams can be divided into two categories: (1) Orbital angular momentum mode sorting; (2) OAM decomposition based on Fourier transformation.

1. Orbital angular momentum mode sorting

a) Hologram

When exposed to the output from a laser or single-mode fibre, a specially designed hologram generates a first-order diffracted beam with a helical phase structure. Conversely, when the setup is used in reverse, it enables the coupling of light in a specific OAM state into the fibre, effectively acting as a mode detector [103, 104]. However, such a hologram can only test one state at a time. To examine multiple potential states, a sequence of holograms is required, which diminishes the advantage of the extensive OAM state space. While more complex holograms can test multiple states simultaneously, their efficiency is generally limited to the reciprocal of the number of states [105].

b) Interference of the beam with a plane wave

Determining the OAM state of light beams can be achieved by analysing the interference with a plane wave and counting the number of spiral fringes in the resultant pattern [106, 107]. Another method involves utilizing the diffraction pattern behind specific apertures to confirm the OAM state of incoming light beams [108]. It's important to note that all these approaches require a considerable number of photons to be in the same mode to generate a well-defined pattern.

c) Rotational Doppler effect

The inherent symmetry in helically phased beams results in a frequency shift when these beams are rotated around their axis [109]. Each mode of OAM induces a distinct frequency sideband [110], presenting a potential method for the OAM measurement [111]. However, the technical challenge arises from the difficulty in accurately measuring the frequency shift. To overcome this challenge, a static beam rotation is used [112]. While this approach mitigates some issues, the technical demands remain considerable, especially for integration into larger systems.

d) Conformal transformation

This approach converts the helical phase structure of a vortex beam into a linear phase gradient. This transformation is achieved using either spatial light modulators (SLMs) [113] or specially designed elements [114, 115]. The resulting linear spread in the beam profile aids in the spatial dispersion of OAM states, distinguishing them based on their topological charges.

e) Sending different OAM modes to different output ports [116]

Researchers suggest a modular process for OAM mode sorting. In this method, each module is designed to receive multiple input OAM modes, output only one specific state, and redirect all other states unaltered for subsequent processing.

2. OAM decomposition based on Fourier transformation

The OAM of LG beams, associated with the azimuthal details of optical fields, can be correlated with angular position through a Fourier relationship, similar to the connection between linear momentum and linear position [117, 118]. Given the 2π periodicity of the angular variable, the relationship takes the form of a Fourier series, resulting in discrete values for the angular momentum, as expressed by [117].

$$\psi_l = \frac{1}{\sqrt{2}} \int_{-\pi}^{+\pi} d\phi \Psi(\phi) \exp(-il\phi) \tag{3.1}$$

$$\Psi(\phi) = \frac{1}{\sqrt{2}} \sum_{-\infty}^{+\infty} \psi_l \exp(il\phi) \tag{3.2}$$

Here ψ_l represents the OAM distribution and $\Psi(\phi)$ is the angular distribution. Eq. (3.2) indicates that an arbitrary angular distribution can be regarded as a coherent combination of different OAM modes.

In 2017, Giuseppe Vallone published an article titled “Role of beam waist in Laguerre–Gauss expansion of vortex beams” [119]. The important conclusion of this paper is that only LG modes with the same beam waist satisfy the orthogonal relation. In the same year, another study [120] introduced decomposing an optical field into Laguerre-Gaussian (LG) modes for optical image processing. Subsequently, a paper titled "Laguerre-Gaussian Mode Expansion for Arbitrary Optical Fields Using a Subspace Projection Method" [121] presented a general method of LG mode expansion for an arbitrary field. It is found that the local frequency distribution of the LG function consists of two parts, the quasi-periodic part and the chirped part. The effective space-bandwidth product of the LG function is defined as the product of the spatial width and frequency domain width of the quasi-periodic part. Based on this space-bandwidth product definition, the criteria for determining the beam waist parameter and the truncation order of the LG series expansion are given. The scheme is tested for the representation of the off-axis Hermite–Gaussian mode, showing that their method is highly accurate. Recently, Ma et al. [122] proposed a systematic scheme for efficient LG mode expansion, incorporating an optimized beam waist for all LG components.

Research on the generation methods of vortex beams is of great significance for studying the properties and applications of optical vortex and AM. Optical micro-ring resonators have garnered considerable attention in recent years due to several merits: their small size makes them easy to integrate; their simple structure facilitates fabrication; and when combined with the mode-support characteristics of bus waveguides, they can generate cylindrically polarised vortex beams [123], to name a few. These attributes have led to their widespread application in optical field manipulation, as shown in various works [124,125,126].

These ultrathin layers consist of artificial nanostructures that provide precise control over light propagation [127]. Integration with Si photonics platforms has facilitated the manipulation and transformation of optical modes confined in Si waveguides [128,129]. By using circulating whispering gallery modes (WGMs), it is possible to shape the wavefront of the output light [130, 131, 132, 133]. The following Figure 3.1 is the schematic of micro-ring OAM laser [125].

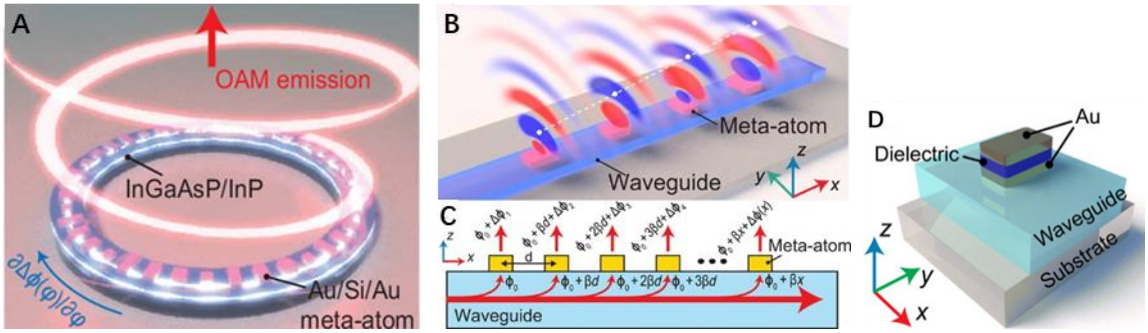

Figure 3.1 Panel (A) [125] depicts a micro-ring OAM laser facilitated by a guided wave-driven meta-surface. The unidirectional phase modulation provided by the meta-surface breaks the degeneracy of the counterclockwise and clockwise whispering gallery modes within the micro-ring resonator, resulting in selective OAM radiation. Panel (B) [125] presents a schematic diagram for a guided wave-driven meta-surface. The phase of the light extracted from a guided wave by each meta-atom can be individually tuned. An array of meta-atoms on the waveguide works together to form specific wavefronts and perform various functions, such as beam deflection and focusing. Panel (C) [125] illustrates the formation of the extracted wave's wavefront. The total phase shift of the extracted wave at coordinate x consists of two components: the phase accumulation βx from the guided wave propagation and the abrupt phase change $\Delta\phi(x)$ induced by the meta-atom. Panel (D) [125] shows a schematic of a metal/dielectric/metal sandwich-structured meta-atom positioned on top of a photonic integrated waveguide.

Panel (A) of Figure 3. 1 illustrates a schematic of a micro-ring OAM laser. This laser utilizes an InGaAsP/InP multi-quantum-well (MQW) micro-ring resonator. Each meta-surface supercell is composed of four meta-atoms with Au/Si/Au sandwich structures. These supercells are periodically patterned on top of the micro-ring. The meta-atoms are positioned 140 nm away from the centre of the waveguide to ensure optimal spatial overlap with the WGM.

The total phase shift of the extracted wave from the driven meta-surfaces is contributed by two factors: (1) the propagation phase accumulation (βx), and (2) the abrupt and spatially variant phase shift denoted by the symbol $\Delta\phi(x)$ as shown in panel (C). Therefore, the phase distribution of the extracted wave can be expressed as follows [125]

$$\phi(x) = \Delta\phi(x) + \beta x \tag{3.3}$$

To achieve full wavefront control, it is essential to induce a phase shift of at least 2π through meta-atoms. Consequently, the authors designed a nano-bar antenna with a metal-dielectric-metal structure (specifically Au/SiO2/Au in this reference) as shown in panel (D). The bottom gold cuboid is excited by the evanescent tail of a guided wave, inducing an electric dipole. A

counteracting dipole is induced in the top gold cuboid. However, the electric dipoles in the top and bottom gold cuboids do not entirely cancel each other out, leading to a net electric dipole resonance. This results in an abrupt phase shift of approximately 2π in the transmitted wave.

The micro-ring resonator inherently supports two degenerate whispering gallery modes (WGMs): a clockwise (CW) mode and a counterclockwise (CCW) mode, each carrying high-order orbital angular momentum (OAM) [134]. When these degenerate WGMs interact with a meta-surface on the micro-ring that introduces a unidirectional phase gradient $\partial\phi/\partial\varphi$ (where φ is the azimuthal angle), the radiated light from the CW and CCW modes will acquire additional but opposite momenta. One of the radiation modes cannot propagates in free space because its wave vector too large, while the other can be radiated into free space with a well-defined OAM order, resulting in the radiation of either the CCW or CW mode. Suppose we aim to extract the CCW mode to form OAM emission in free space. The propagation constant of the mth-order CCW WGM is given by $\beta_{CCW} = \frac{2\pi n_m}{\lambda} = M/R$, where n_m is the modal index and R is the radius of the micro-ring. A guided wave-driven meta-surface is placed on the micro-ring to induce a phase gradient equivalent to a wave number $k_{ms} = -\frac{2\pi}{\Lambda}$, where Λ is the length of the supercell composed of a set of meta-atoms. The azimuthal phase dependence of the OAM emission can be expressed as $\phi_{OAM}(\varphi) = \ell\varphi$. Due to momentum conservation, the following condition must be satisfied [134].

$$\ell\varphi = \phi_{OAM} = \phi_{CCW} + \phi_{ms} = \beta_{CCW}R\varphi - \frac{2\pi R}{\Lambda}\varphi \tag{3.4}$$

The guided wave-driven meta-surface is positioned on the micro-ring to create a phase gradient. Given that the total number of meta-surface supercells on the micro-ring is $N = \frac{2\pi R}{\Lambda}$, a well-defined topological charge from Eq. (3.4) can be driven [134]:

$$\ell = M - N \tag{3.5}$$

In practical scenarios, generated vortex beams often carry OAM with multiple modes rather than just one. The research group I collaborate with has presented research on asymmetric vortex beam emission in a meta-surface-integrated micro-ring. The micro-ring they designed can generate different OAM-carrying beams by manipulating the wavelength of the light source. Figure 3.2 (a) and (b) illustrate the simulated and theoretical intensity and distribution of the beam generated by a meta-surface integrated micro-ring with OAM of $\ell = -9$. The term "theoretical" here means that, according to the principle of the meta-surface micro-ring resonator as previously mentioned, especially Eq. (3.4) and Eq. (3.5), the device can be designed to generate a target optical field carrying a certain mode OAM.

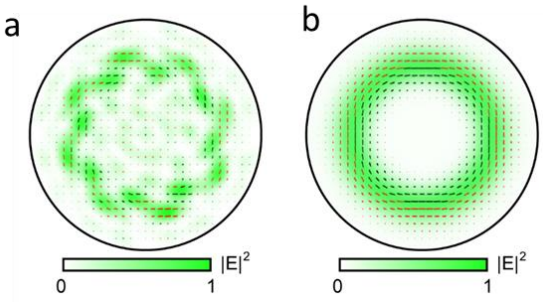

Figure 3.2 Panel (a) and panel (b) illustrate the simulated and theoretical intensity and distribution of the optical field generated by meta-surface integrated micro-ring resonator with OAM of $\ell = -9$.

Comparing above two subgraphs, it becomes evident that the two are not entirely consistent. This discrepancy arises from the fact that the purity of the OAM of $\ell = -9$ carried by the meta-surface integrated micro-ring generated beam is not 100%. To determine the purity of OAM of beams generated by a designed device, researchers often need to fabricate the device and test it. The testing methods frequently involve analysing the interference patterns of the fundamental Gaussian mode and the generated beams [135]. By counting the number and direction of interference fringes, researchers can determine the value and handedness of angular momentum.

Currently, a comprehensive approach based on simulation results to analyse the angular momentum in vortex beams is lacking. In collaboration with a research group, I aimed to develop a general method based on numerically analysing the angular momentum of light beams using simulation results from the micro-rings they designed. With this method, the analysis of the value of OAM or the values of TAM of the beam generated by these micro-ring resonators can be achieved during the device design and simulation phase, eliminating the need for device fabrication and testing to verify device performance. This significantly saves time, labour, and financial costs while enhancing the efficiency of device design and development.

3.2 Method

3.2.1 Analysis of Orbital Angular Momentum in Scalar Vortex Beams

A complete orthogonal basis of Laguerre-Gaussian (LG) modes has been introduced in Chapter 1. By utilizing LG modes, it becomes possible to express and describe arbitrary scalar monochromatic beams under paraxial approximation by Eq. (3.6) [121, 136].

$$\Psi(r,\phi) = \sum_{p,\ell} C_p^{\ell}\ LG_p^{\ell}(r,\phi) \tag{3.6}$$

where, the parameter C_p^ℓ represents the OAM spectra of the complex amplitude distributed on the r-ϕ plane. By using the following 2D integrals, the C_p^ℓ can be calculated:

$$C_p^\ell = \int_0^\infty r dr \int_0^{2\pi} [LG_p^\ell(r,\phi)]^* \Psi(r,\phi)\, d\phi \tag{3.7}$$

Due to the conjugate of $LG_p^\ell(r,\phi)$, the field components with the longitudinal OAM relevant term $e^{i\ell\phi}$ will be extracted ($(e^{i\ell\phi})^* e^{i\ell\phi} = e^0 = 1$). According to Eq. (3.6) and Eq. (3.7), the process of the OAM analysis can be divided into two main steps. Firstly, I integrate the term $[e^{i\ell\phi}]^* \Psi(r,\phi)$ in the azimuthal direction, obtaining the radial component ($\Psi(r)$) of the $\Psi(r,\phi)$. Secondly, I multiply it with the LG bases' radial components ($LG_p^\ell(r)$), allowing the complex amplitude C_p^ℓ to be calculated. Figures 3.3 and 3.4 display the calculation details in matrices, showing how to numerically analyse the OAM modes when the transverse complex field information $\Psi(r,\phi)$ has been gathered. The first step is detailed in Figure 3.3. By integrating the dot product of the conjugate matrix of the azimuthal phase factor and $\Psi(r,\phi)$ with respect to the azimuthal angle, the radial component $\Psi(r)$ can be calculated. These components are arranged in corresponding rows according to the values of OAM from smallest to largest. Figure 3.4 illustrates the second step in determining the OAM spectra C_p^ℓ. In this step, we need to extract the radial field information corresponding to the OAM of interest from the matrix $\Psi(r)$ computed in the previous step. Since the radial field information in each row corresponds to one mode of OAM, extracting the radial field information from a specific row is equivalent to extracting the field information carrying a specific OAM mode. By multiplying the extracted radial field component information associated with a certain OAM mode by the radial distribution of the corresponding OAM mode in the LG orthogonal bases, the OAM spectra C_p^ℓ can be obtained.

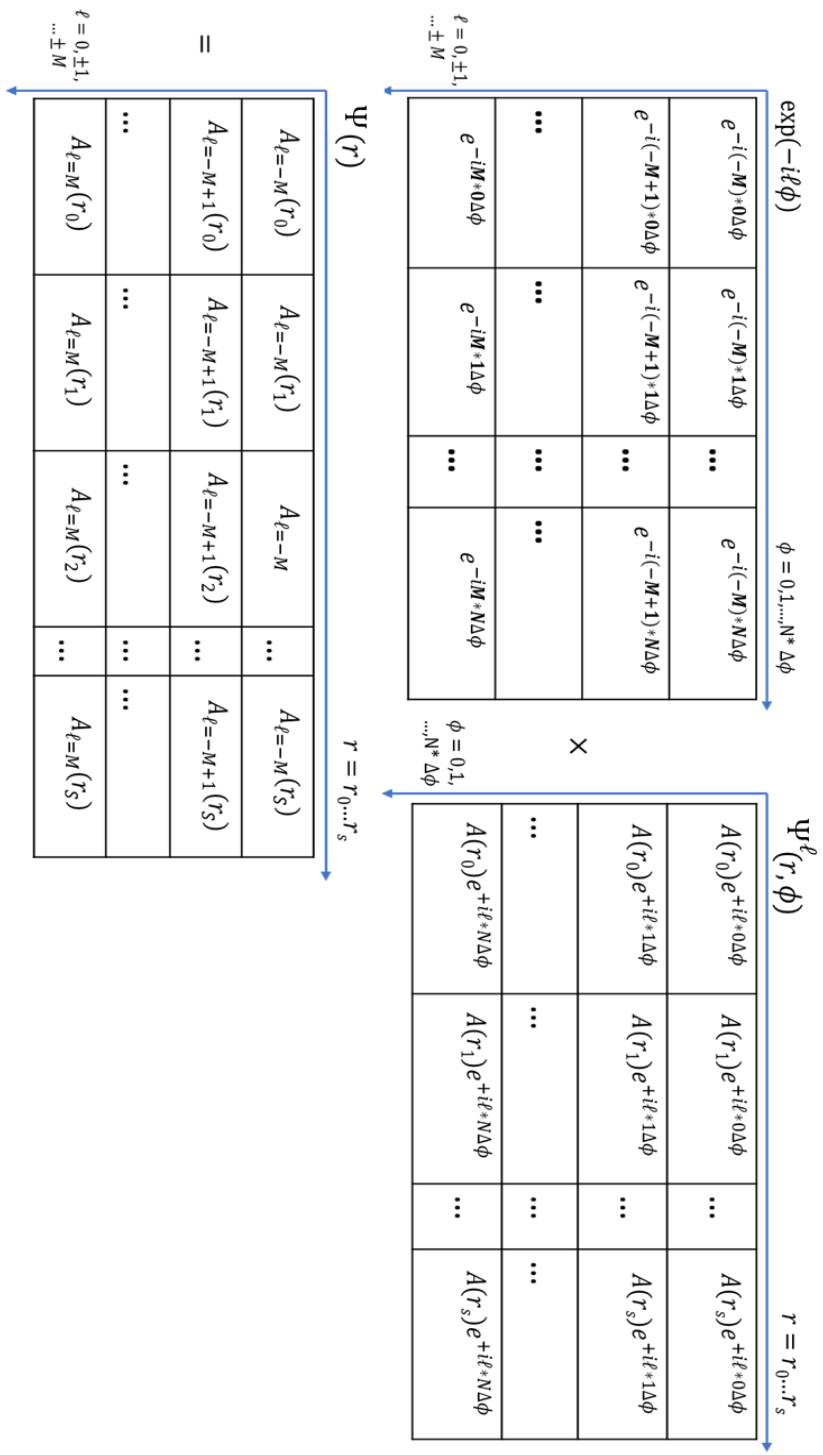

Figure 3.3 displays the process of the first step of OAM mode analysing. By this step, the distribution of the optical field varying in the r direction ($\Psi(r)$) can be obtained.

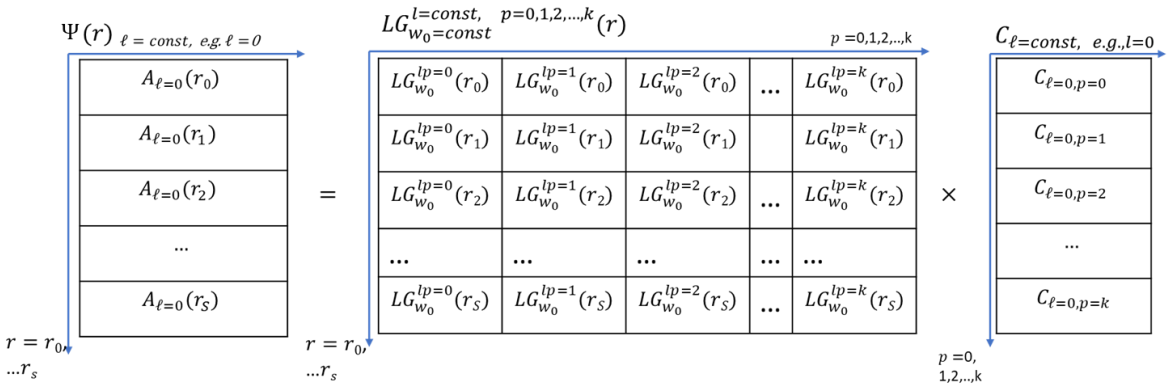

Figure 3.4 shows the second step to calculate the OAM spectra C_p^ℓ. By multiplying the extracted radial field component information associated with a certain OAM mode by the radial distribution of the corresponding OAM mode in the LG orthogonal bases, the OAM spectra C_p^ℓ can be obtained.

3.2.1.1 Transformation of Coordinates

It should be noted that the resultant simulated field is always expressed in Cartesian coordinates in some simulation software. By using the command ("cart2pol") provided by MATLAB, it is easy to convert the coordinates (x, y) to (r, ϕ). However, there is an issue in this process: the coordinate conversion merely rewrites the coordinates (x, y) as (r, ϕ), and the converted "$\Psi(r, \phi)$" is still arranged in the mesh defined in Cartesian coordinates. However, $\Psi(r, \phi)$ should be rearranged according to the increasing values of r and ϕ , as shown in Figure 3.5. This step is very important.

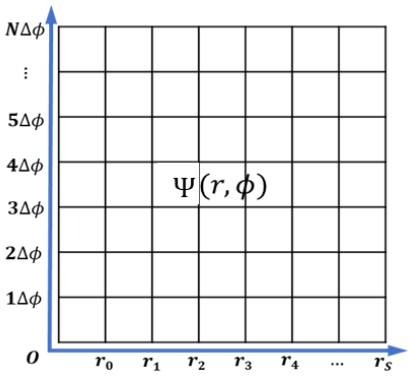

Figure 3.5 The schematic diagram for the rearranged $\Psi(r, \phi)$.

3.2.1.2 Optimizing Beam Width for OAM Analysis

Before the OAM analysis for arbitrary monochromatic vortex beams under paraxial approximation, the parameter "beam width" of LG-mode bases should be initialized. The choice of the beam width for the LG bases depends on the spot size of the vortex beam being analysed. There are two ways to define the radius of spot sizes:

1) The radius of the LG vortex beam is defined as the distance from the beam centre to the points where maximum intensity is found. In this context, ℓ represents the topological charge (TC) of the LG beam; w(z) is the transverse beam size; w_0 is the beam radius at z=0; and z_R is the Rayleigh range of the Gaussian envelope [137].

$$r = r(I_{max}) = \sqrt{\frac{|\ell|}{2}} \cdot \mathrm{w(z)},$$
$$\mathrm{w(z)} = w_0 \sqrt{1 + \left(\frac{z}{z_R}\right)} \tag{3.8}$$

2) Mean-squared spot width: The radius of the spot size for our generated optical fields is determined by the square root of the mean-squared width. [138]

$$w^2 = \frac{\int_0^{2\pi} \int_0^{\infty} r^2 I(\rho, \varphi, z) \rho d\rho d\varphi}{\int_0^{2\pi} \int_0^{\infty} I(\rho, \varphi, z) \rho d\rho d\varphi} \tag{3.9}$$

The first definition, expressed by Eq. (3.8), is typically used for fields with intensity distributions identical to those of LG beams, characterised by a perfect donut shape. Conversely, the second method (Eq. (3.9)) offers greater versatility and flexibility compared to Eq. (3.8). The vortex beams we prepared for analysis, as illustrated in panel (a) of Figure 3.2, do not exactly match the intensity distribution of a perfect LG beam. Therefore, in this work, I adopt the mean-squared spot width method to define the beam width of the LG basis, based on the characteristics of the simulated field.

3.2.2 Analysis of Total Angular Momentum in Vector Vortex Beams

Due to the structural and mode-supporting characteristics of meta-surface integrated micro-rings, beams generated by them often fall under the category of VVBs. A VVB is a type of optical field in which polarization and spatial mode are non-separable [34], indicating that it cannot be treated as a scalar field. However, by utilizing the Total Angular Momentum-Conserving Poincaré Sphere (TAM-C PS) introduced in Chapter 2, we can determine the TAM spectra of VVBs. The optical fields corresponding to the north and south poles of the TAM-C PS represent eigenmodes, which are right- and left-circularly polarized vortex beams. The procedure for analysing TAM of VVBs is as follows:

Step 1. Analyse states of polarisation of optical fields using Stokes parameters. Every monochromatic wave is, by definition, necessarily polarised [100]. The Stokes parameters provide an alternative description of the polarisation state which is experimentally convenient because

each parameter corresponds to a sum or difference of measurable intensities of optical fields. And according to the Stokes parameters, the components, left- and right- circular polarisation states (termed “L” and “R”), of the VVB can be measured.

Step 2. Analyse the value of OAM for VVB’s left and right circular polarisation states. If a VVB under analysis is dominated by a TAM component which is $t\hbar$, the spectral plot should exhibit prominent peaks at $t+1$ and $t-1$. The peak at $t+1$ represents the OAM value of its eigenstate, left-circularly polarised vortex beam. And the peak at $t-1$ represents the OAM value of the other eigenstate, right-circularly polarised vortex beam.

3.3 Results

3.3.1 OAM Spectra of Scalar Vortex Beams from Meta-Surface Integrated Micro-ring Resonators

The resultant vortex beam generated by the micro-ring is mainly s-polarised in spherical coordinates (i.e., the polarisation state aligns with the azimuthal direction). Therefore, we can only analyse the s-polarised component of the vortex beam. Since only one component of the resultant field is analysed. The OAM analysis to the s-polarised component of the resultant field simplifies to a scalar case. Using the method introduced in the previous section, we can obtain the OAM spectra shown in Figure 3.6. The data for the resultant field is provided by our colleagues. The following subfigures show the OAM analysis spectra of the vortex beam generated by resonators with OAM design values of -7, -8, and -9, from left to right.

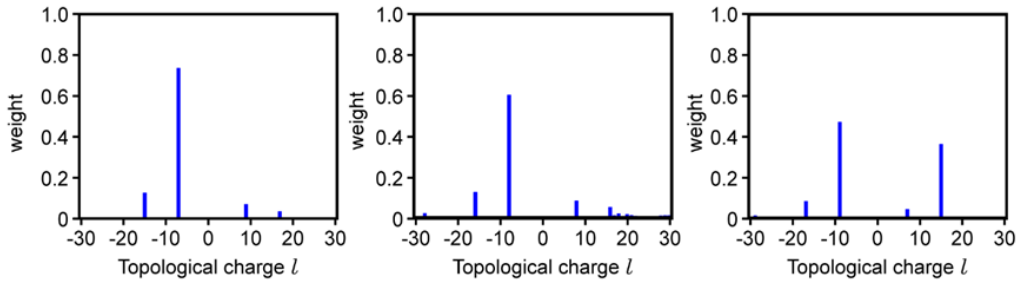

Figure 3.6 The OAM spectra of the of the vortex beam generated by a meta-surface integrated micro-ring resonator with different target modes of OAM (from left to right, topological charges are -7, -8 and -9, respectively).

In Figure 3.6, the OAM value corresponding to the highest bar represents the theoretical design value of the OAM mode of the meta-surface integrated micro-ring resonator. I noticed multiple bars in each spectrum, indicating that there is actually multiple OAM modes present in these

resultant optical fields. Therefore, the intensity distribution shown in panel (a) in Figure 3.2 is not completely consistent with panel (b).

3.3.2 TAM Spectra of Vector Vortex Beams from Meta-Surface Integrated Micro-ring Resonators

This section shows the TAM analysing results for VVBs generated by the micro-ring resonator designed by our collaborators. By varying wavelengths, VVB carrying different TAM are generated. The information for each analysed VVB is labelled in the legend at the upper corner of each image. This legend includes the wavelength information of the analysed beam (in nanometres, rounded to two decimal places, e.g., 162713 means λ=1627.13nm); "N" indicates the counterclockwise handedness of TAM, corresponding to the symbol "−" in the topological charge of TAM; Symbols "R" and "L" stand for right-circularly, and left-circularly polarised components, respectively.

There are two plots of spectra for each VVB, as the VVB is mapped to two eigenstates of TAM-C PS. One spectrum shows the OAM value of an eigenstate of VVBs. The eigenstates of VVBs are the right-circularly polarised vortex beam and the left-circularly polarised vortex beam.

We use the symbol "t" to represent the value of TAM of a VVB. Each spectral plot exhibits a prominent peak at $t+1$ or $t-1$. The peak at $t+1$ represents the OAM value of the VVB's one eigenstate, left-circularly polarised vortex beam. The peak at $t-1$ represents the OAM value of the other eigenstate, right-circularly polarised vortex beam. Figure 3.7 consists of 6 images, and 2 images (e.g. "A1" and "A2") are a set. Each set are TAM spectra for a VVB generated by the micro-ring resonator. There are three sets of VVBs with target value of TAM of these VVB are -7, -8 and -9, respectively.

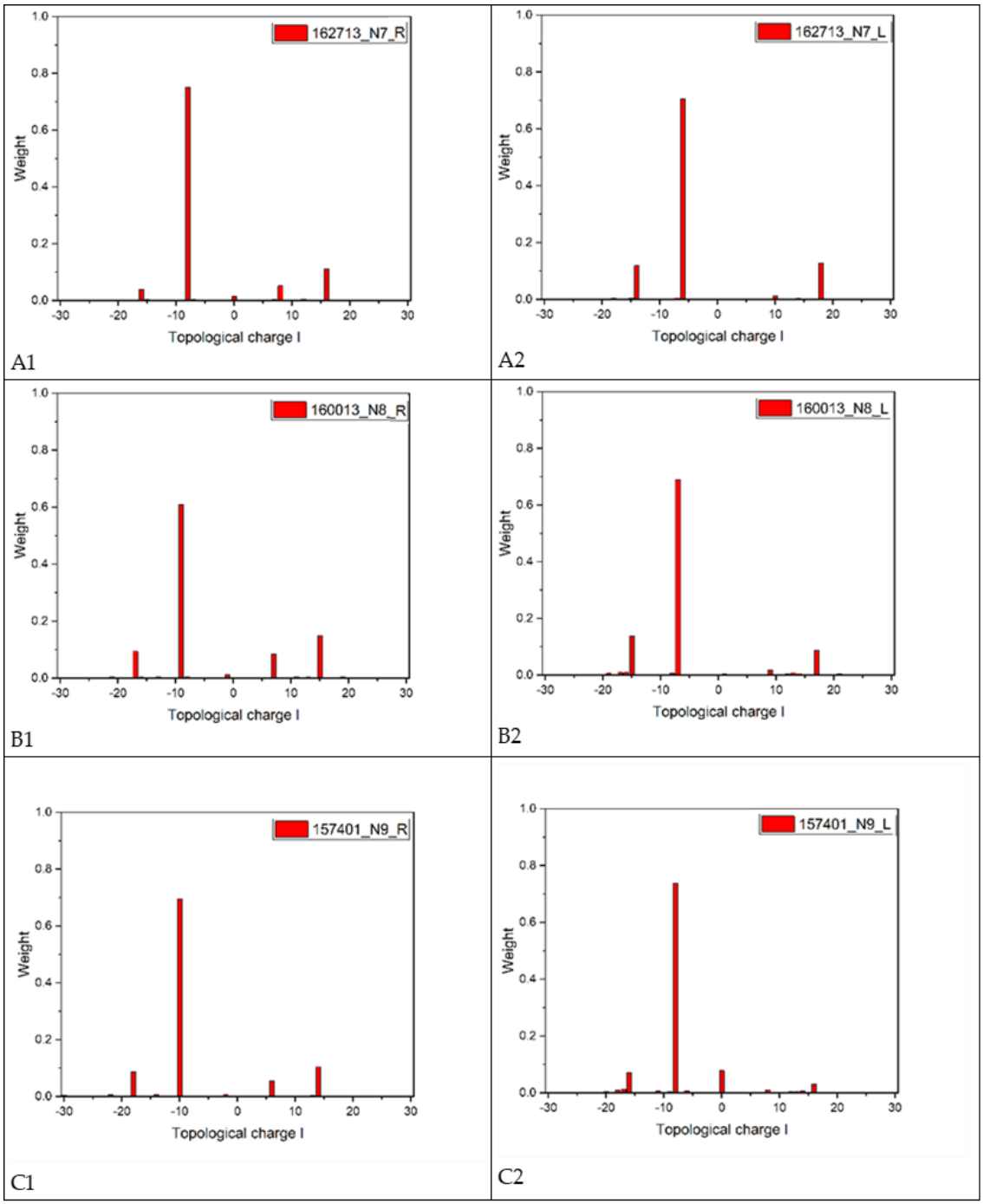

Figure 3.7 Set (A) TAM spectra of VVB with a target mode of TAM of -7. (A1) This spectrum represents the value of OAM of the VVB's eigenstate that is the right-circularly polarised vortex beam. (A2) This spectrum represents the value of OAM of the VVB's eigenstate that is the left-circularly polarised vortex beam; Set (B) TAM spectra of VVB with a target mode of TAM of -8. (B1) This spectrum represents the value of OAM of the VVB's eigenstate that is the right-circularly polarised vortex beam. (B2) This spectrum represents the value of OAM of the VVB's eigenstate that is the left-circularly polarised vortex beam; Set (C) TAM spectra of VVB with a target mode of TAM of -9. (C1) This spectrum represents the value of OAM of the VVB's eigenstate

that is the right-circularly polarised vortex beam. (C2) This spectrum represents the value of OAM of the VVB's eigenstate that is the left-circularly polarised vortex beam; The legend at the upper corner of each image includes the wavelength information of the analysed beam (in nanometres, rounded to two decimal places, e.g., 162713 means λ=1627.13nm); N indicates the counterclockwise handedness of AM, corresponding to the symbol "—" in the topological charge of TAM; "R" and "L" stand for two eigenstates of VVBs, which are right-circularly and left-circularly polarised vortex beam, respectively.

3.4 Conclusion

Using Fourier transform, the theory of TAM-C PS provided in Chapter 2, and the fact that Laguerre–Gaussian modes are a set of complete orthogonal bases, we establish a method for analysing the value of OAM in scalar vortex beams and TAM in VVBs. This approach has assisted our collaborators in analysing the OAM and TAM of vortex beams generated by their meta-surface integrated micro-ring resonators during the design and simulation phases. This means we do not have to physically fabricate and test the device in the early stages of research to ensure that the resonator design can generate vortex beams with the target OAM or TAM, which can save a significant amount of time, effort, and money. Additionally, this work is expected to be applied to some optical sensing scenarios, such as identifying and detecting signals (i.e., vortex beams) from noise by OAM modes and deducing information about objects interacting with the vortex beam based on changes in OAM modes of signals.

Chapter 4 Modelling and Analysis of Vector and Vector Vortex Beams Reflection for Optical Sensing

Light Detection and Ranging (LiDAR) sensors can precisely determine object distances using the pulsed time of flight (TOF) or amplitude-modulated continuous wave (AMCW) TOF methods and velocity using the frequency-modulated continuous wave (FMCW) approach. In this chapter, we focus on modelling and analysing the reflection of vector beams and vector vortex beams (VVBs) for optical sensing in LiDAR applications. Unlike traditional TOF and FMCW methods, this novel approach uses vector beams and VVBs as detection signals to measure the orientation of reflecting surfaces. A key component of this sensing scheme is understanding the relationship between the characteristics of the reflected optical fields and the orientation of the reflecting surface. To this end, we develop a computational model for the reflection of vector beams and VVBs. This model allows us to investigate critical aspects of the reflected field, such as intensity distribution, intensity centroid offset, reflectance, and the variation of the intensity range measured along the azimuthal direction. By thoroughly analysing these characteristics, we aim to enhance the functionality of LiDAR sensors in detecting the orientation of reflecting surfaces.

4.1 Introduction

LiDAR is a method used to determine distances by directing a laser at an object or surface and measuring the time it takes for the reflected light to return to the receiver, and it can be categorised into two schemes: pulsed time of flight (TOF) [69,70] and amplitude-modulated continuous wave (AMCW) TOF [71, 72]. Additionally, another sensing scheme called frequency-modulated continuous wave (FMCW) is also commonly used in LiDAR. By analysing the beat signal between the emitted and reflected frequency-modulated optical signals, both the distance and the velocity of a moving object can be measured [73,74]. LiDAR finds extensive applications across various scenarios: terrestrial and mobile environments [139]; environmental monitoring and conservation [140]; archaeology and cultural heritage preservation [141,142], and autonomous vehicles and transportation [143], to mention a few [144]. Lasers with wavelengths in the range of 600–1000 nm are widely employed for non-scientific purposes. To ensure safety for individuals on the ground, a popular alternative involves using 1550 nm lasers, which are considered eye-safe even at relatively high-power levels, as this wavelength is not strongly absorbed by the eye. However, there is a trade-off, as the current detector technology for these wavelengths is less advanced. Consequently, these lasers are typically used at longer ranges with lower accuracies. Additionally, these lasers find applications in military contexts because the 1550 nm wavelength is

not visible in night vision goggles, in contrast to shorter 1000 nm infrared laser [145]. Therefore, researchers in LiDAR technology often prioritise the wavelength of the laser. Recently, the robustness of VVBs propagating through highly aberrated systems has been investigated, revealing that the inhomogeneous nature of polarisation persists even as the medium undergoes changes [146]. This approach opens avenues for the versatile application of vectorially structured light, even in non-ideal optical systems, proving crucial for applications such as imaging and optical communication across noisy channels. However, the research area concerning the use of vector beams, particularly VVB, in LiDAR has not yet been thoroughly investigated. The reflection of vector beams and VVB is worth studying as they represent a special type of structured light combining two degrees of freedom (DoF) of light: polarisation DoF and spatial DoF. This unique combination enables them to be mapped onto TAM-C Poincaré spheres [147]. These beams can provide more information in optical sensing. For example, the use of beams carrying OAM to achieve lateral motion detection has been demonstrated in previous research [148]; vectorial Doppler metrology for particles was realised in another study [149]; and photonic Hall effects involving optical angular momenta is also a popular research area [150]. Recently, a sensor that can detect changes in the refractive index of biological samples based on the photonic spin Hall effect has been proposed [151]. In recent years, a group of researchers were the first to study the transverse and Goos–Hänchen shifts of spatiotemporal optical vortices reflected/refracted at planar interfaces [152].

Methods for studying the reflection and refraction of a paraxial optical beam at a plane interface, which separates two dielectric media without absorption, have been developed in [153,154]. The incident beam has a finite spatial frequency spectral distribution under the assumption of the paraxial approximation, which is somewhat more complex compared to the ray model for light. The angular spectrum method is an effective approach for obtaining the spatial frequency spectra of incident light beams. In this study [155], the reflection and transmission characteristics of a LG beam from uniaxial anisotropic multilayered media are analysed using the angular spectrum expansion. Additionally, the angular spectrum method has been applied in the investigation of the photonic spin Hall effect [156]. All the works are studied under the assumption of paraxial beams; however, this work [157] goes beyond the paraxial regime, providing analytical expressions for the partially reflected field of LG beams. It is necessary to introduce spherical coordinates to conveniently use the S/P-wave to describe the polarisation states of the incident beam [158]. Subsequently, the ratios of reflected light to the incident light can be obtained with the help of the Fresnel equation.

In this work, we develop a computation model for the reflection process of VBs and VVBs and then examine the feasibility of using these beams as the detection signal for the LiDAR sensor to

measure the orientation of reflecting surfaces. This approach introduces a new sensing scheme for LiDAR.

4.2 Method

4.2.1 Expressions of a Well-Collimated Incident Beam

Figure 4.1 illustrates a schematic for a beam that has undergone a Fourier transform. In this study, under the condition that the incident beam is well-collimated, its angular spectra can be approximated as a narrow expansion around a central wavevector $\boldsymbol{k}_c$ ($|\boldsymbol{k}_c| = 2\pi/\lambda$, λ represents the wavelength) which is depicted by a black ray. The non-central wavevectors ($\boldsymbol{k}$) can be expressed as the vector addition of the beam's central wavevector and a small orthogonal deflection ($\boldsymbol{\Delta}$) [159]. Here, $\boldsymbol{\mu}$ and $\boldsymbol{\nu}$ are a set of orthogonal unit vectors along the direction of in-plane and out-of-plane incidence, respectively. Consequently, we have the followings:

$$\boldsymbol{k} = \boldsymbol{k}_c + \boldsymbol{\Delta} \backsimeq \boldsymbol{k}_c + a\boldsymbol{\mu} + b\boldsymbol{\nu} \tag{4.1}$$

$$|\boldsymbol{\Delta}| \ll |\boldsymbol{k_c}| = \frac{\boldsymbol{2\pi}}{\boldsymbol{\lambda}} \tag{4.2}$$

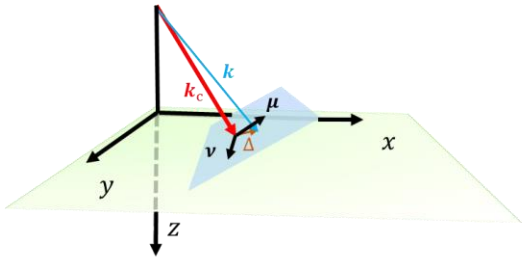

Figure 4.1 shows a schematic for a paraxial approximation beam performed a Fourier transform; $\boldsymbol{k_c}$ is its central wavevector (represented by a red ray). The non-central wave vector can be expressed as the vector addition of beam's central wavevector $\boldsymbol{k_c}$ and a small orthogonal deflection $\boldsymbol{\Delta}$ (depicted by a brown ray). $\boldsymbol{\mu}$ and $\boldsymbol{\nu}$ are a set of orthogonal unit vectors along the direction of in and out of the plane of incidence, respectively.

4.2.2 Frames of Reference and Coordinates in the Reflection Process of Light Beams

In the reflection process, two frames of reference are involved: the frame of the beam and the frame of the lab. These are represented by yellow beam-like shapes and a blue rectangle, respectively, as shown in Figure 4.2. Four types of coordinates are established on each frame. The incident beam coordinates are depicted by three blue rays labelled "$x_{\mathrm{b_{inc}}}^{centre}$", "$y$" and "$z_{\mathrm{b_{inc}}}^{centre}$"; the reflected beam coordinates are shown by three red rays labelled; the Cartesian lab

coordinates are represented by three black rays labelled "X_{lab}", "y" and "Z_{lab}"; and the spherical lab coordinates are depicted by three green rays labelled "$\hat{r}$", "$\hat{\varphi}$" and "θ".

The two beam coordinates are mirror images of each other. The origin of the Cartesian lab coordinates is set at the incident point on the interface, which is defined as the intersection point between the central wave vector of the incident beam and the reflection interface. The central wave vector of the incident beam and the normal to the reflection interface lie within the x-z plane. The direction perpendicular to this plane is defined as the $\hat{y}$-direction.

In addition, the spherical coordinate system within the laboratory frame is necessary for the study because of the followings: 1. It allows for a convenient representation of the transform between non-central wave vectors and the central wave vector. 2. The electric field components E_{φ} and E_{θ} in the spherical coordinate correspond to the s and p polarisation states in the Fresnel equation. Consequently, building the laboratory spherical coordinate system will facilitate computations.

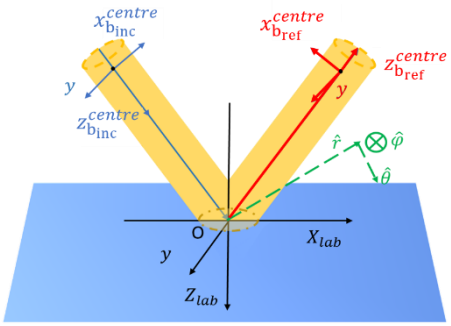

Figure 4.2 shows a schematic of two frames of reference (frames of lab and beam) and four coordinate systems (incident and reflected beam coordinates; Cartesian lab coordinates, and spherical lab coordinates) involved in the reflection process.

By rewriting the small orthogonal deflection (**Δ**) in the incident beam coordinates, we have the following:

$$\boldsymbol{\Delta} \backsimeq a\boldsymbol{\mu} + b\boldsymbol{\nu} = |\boldsymbol{k}_c|\left(\zeta \hat{x}_{b_{inc}} + \eta \hat{y}\right). \tag{4.3}$$

The angular spectrum method is commonly employed to obtain the spatial spectra of the incident beam [160]. To better understand the role of the angular spectrum method in the study, it is essential to review the concepts of plane waves and the angular spectrum method. Figure 4.3 is a schematic diagram of plane waves propagating in free space:

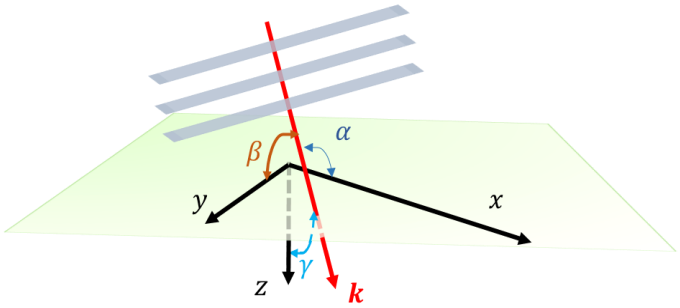

Figure 4.3 The plane wave (represented by three grey planes) propagating along the direction of its wavevector $\boldsymbol{k}$ (represented by a bright red ray). α, β, and γ are the angles between the plane wavevector $\boldsymbol{k}$ and the x, y, z axes, respectively.

The complex field expression of the plane wave in Cartesian coordinates is the following:

$$U(x,y,z) = Ae^{ik(xcos\alpha+ycos\beta+zcos\gamma)} \tag{4.4}$$

k is the wavenumber and α, β, γ are the angles between the plane wave vector $\boldsymbol{k}$ and x, y, z axes, respectively. The relationship between the three angles is the following:

$$cos^2\alpha + cos^2\beta + cos^2\gamma = 1 \tag{4.5}$$

This relationship indicates that there are only two independent variables. Consequently, Eq. (4.4) can be rewritten as follows:

$$U(x,y,z) = Ae^{ik(xcos\alpha+ycos\beta)}\, e^{ikz\sqrt{1-cos^2\alpha-cos^2\beta}} \tag{4.6}$$

In Fourier optics, Eq. (4.5) is frequently rewritten as follows (λ is wavelength) [161]:

$$F_x^2 + F_y^2 + F_z^2 = \frac{1}{\lambda^2} \tag{4.7}$$

Hence, $cos\alpha = \lambda F_x$; $cos\beta = \lambda F_y$.

Consequently, in the beam coordinate system, the non-central wave vectors, or the orthogonal deflection ($\boldsymbol{\Delta}$) as demonstrated in Eq. (4.3), can be reformulated as follows:

$$\left|\boldsymbol{k}_{x_{b_{inc}}}^{non_{central}}\right| = \left|\boldsymbol{k}_{x_{b_{inc}}}\right| = |a\boldsymbol{\mu}| = |\boldsymbol{k}_c|\zeta = |\boldsymbol{k}_c|cos\alpha, \tag{4.8}$$

$$\left|\boldsymbol{k}_{y}^{non_{central}}\right| = \left|\boldsymbol{k}_{y}\right| = |b\boldsymbol{\nu}| = |\boldsymbol{k}_c|\eta = |\boldsymbol{k}_c|cos\beta. \tag{4.9}$$

Moreover, we can find the following:

$$\zeta = cos\alpha, \tag{4.10}$$

$$\eta = cos\beta. \tag{4.11}$$

4.2.3 Calculation of Reflected Optical Fields on Dielectric Materials

It is natural to study the spatial spectra of the incident light beam in the incident beam coordinates. However, using the frame of the lab with spherical coordinates is more convenient for calculating the ratios of reflected light to incident light using the Fresnel equation. Eq. (4.12) illustrates the transformation of the incident light beam's spectra from beam coordinates to the lab spherical coordinates.

$$\left|\tilde{E}\right\rangle_b^{inc} = \widehat{R_y}(\theta_i)\widehat{R_{Z_{lab}}}(\phi_i)\widehat{R_y}\left(-\vartheta_{inc}^{central}\right)\left|\tilde{E}\right\rangle_b^{inc} \tag{4.12}$$

The symbol $\vartheta_{inc}^{central}$ represents the magnitude of angle between the central wave vector and the normal to the reflection surface. To determine the angles of incidence for non-central wave vectors, the relationships between non-central and central wave vectors must first be clarified. These relationships involve the angles ϕ_i and θ_i. Eq. (4.13) and Eq. (4.14) provide the expressions for these angles [158], and Figure 4.4 is the schematic illustrating them.

$$\phi_i \backsimeq \tan(\phi_i) = \frac{b|\boldsymbol{\nu}|}{|\boldsymbol{k}_c| sin(\vartheta_{inc}^{central})} = \frac{\eta|\boldsymbol{k}_c|}{|\boldsymbol{k}_c| sin(\vartheta_{inc}^{central})} = \frac{\cos\beta}{sin(\vartheta_{inc}^{central})} \tag{4.13}$$

$$\theta_i = \vartheta_{inc}^{central} + \theta_{def} \backsimeq \vartheta_{inc}^{central} + \tan(\theta_{def}) = \vartheta_{inc}^{central} + \frac{a|\boldsymbol{\mu}|}{|\boldsymbol{k}_c|} = \vartheta_{inc}^{central} + \frac{\zeta|\boldsymbol{k}_c|}{|\boldsymbol{k}_c|} = \vartheta_{inc}^{central} + \cos\alpha \tag{4.14}$$

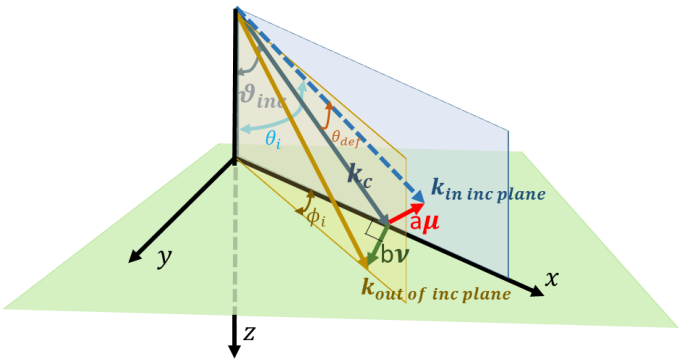

Figure 4.4 The schematic for ϕ_i and θ_i. The $\boldsymbol{k}_{in\ inc\ plane}$ (light blue dashed ray) represents the non-central wave vector within the incident plane defined by central wavevector $\boldsymbol{k}_c$ (dark blue ray); The $\boldsymbol{k}_{out\ inc\ plane}$ (brown ray) represents the non-central wave vector lies outside of the incident plane; The $a\boldsymbol{\mu}$ (red ray) and $b\boldsymbol{\nu}$ (dark green ray) are a set of orthogonal deflections along the direction of in and out of plane of incidence, respectively. The symbol $\vartheta_{inc}^{central}$ represents the magnitude of the angle of central wave incidence. Moreover, θ_{def} is the angle between $\boldsymbol{k}_c$ and $\boldsymbol{k}_{in\ inc\ plane}$.

When the transfer matrix [156, 158] (T^r, shown in Eq. (4.15)) is clear, the ratios of reflected light to the incident light can be calculated. The spectra of the reflected beam ($\left|\tilde{E}\right\rangle_b^{ref}$) is the following:

$$\left|\tilde{E}\right\rangle_b^{ref} = T^r\left|\tilde{E}\right\rangle_b^{inc} = F^r\widehat{R_y}(\theta_i)\widehat{R_{Z_{lab}}}(\phi_i)\widehat{R_y}\left(-\vartheta_{inc}^{central}\right)\left|\tilde{E}\right\rangle_b^{inc}, \tag{4.15}$$

$$T^r = F^r\widehat{R_y}(\theta_i)\widehat{R_{Z_{lab}}}(\phi_i)\widehat{R_y}\left(-\vartheta_{inc}^{central}\right) = F^r\begin{vmatrix} 1 & \eta\cot\vartheta_{inc}^{central} \\ -\eta\cot\vartheta_{inc}^{central} & 1 \end{vmatrix}.$$

F^r is the Fresnel Jones matrix [158] shown in Eq. (4.16). The symbols r_p and r_s represent the Fresnel coefficients associated with the polarisation components parallel (r_p) and orthogonal (r_s) to the plane of incidence, respectively. Using Taylor series expansion for spectral components around the central wave vector ($\boldsymbol{k}_c$) and focusing solely on the initial expansion term, we can formulate the Fresnel Jones matrix [156, 158]

$$F^r = \begin{bmatrix} r_p\left(\vartheta_{inc}^{central}\right)\left(1+\zeta\dfrac{\partial r_p(\theta_i)}{\partial\theta_i}\right) & 0 \\ 0 & r_s\left(\vartheta_{inc}^{central}\right)\left(1+\zeta\dfrac{\partial r_s(\theta_i)}{\partial\theta_i}\right) \end{bmatrix}. \tag{4.16}$$

Therefore, the transfer matrix can be further elaborated as follows:

$$T^r = \begin{bmatrix} r_p(\vartheta_{inc}^{central})\left(1+\zeta\dfrac{\partial r_p(\theta_i)}{\partial\theta_i}\right) & r_p(\vartheta_{inc}^{central})\eta\cot\vartheta_{inc}^{central} \\ -r_p(\vartheta_{inc}^{central})\eta\cot\vartheta_{inc}^{central} & r_s(\vartheta_{inc}^{central})\left(1+\zeta\dfrac{\partial r_s(\theta_i)}{\partial\theta_i}\right) \end{bmatrix}. \tag{4.17}$$

Where ε represents the relative dielectric constant of the reflecting surface and expressions of $r_p(\vartheta)$ and $r_s(\vartheta)$ are the following:

$$r_p(\vartheta) = \frac{\varepsilon cos\vartheta - \sqrt{\varepsilon - \sin^2\vartheta}}{\varepsilon cos\vartheta + \sqrt{\varepsilon - \sin^2\vartheta}}, \tag{4.18}$$

$$r_s(\vartheta) = \frac{cos\vartheta - \sqrt{\varepsilon - \sin^2\vartheta}}{cos\vartheta + \sqrt{\varepsilon - \sin^2\vartheta}}. \tag{4.19}$$

4.3 Results

A computational model for vector beams and VVBs reflection is developed by MATLAB. The parameters for the setup of the simulation are as follows: wavelength: 532nm; beam width of fundamental mode (the distance from the centre to points where the maximum intensity is found [162]): 13μm; frame of the figure: 30μm × 30μm (drawing dimensions of optical fields); pixel array: 1024 × 1024 (the optical field distribution image features 1024 pixels in each of the horizontal and vertical directions).

4.3.1 Intensity and Polarisation Distribution of the Incident Beam and of the Reflected Beam at the Brewster Angle

Vector beams and in particular, VVBs are natural solutions to the full vector wave equation [163], and more commonly, they are represented as the superposition of orthogonal scalar fields, which have orthogonal polarization states [164]. As shown in Eq. (4.20).

$$|VL\rangle = \psi_R^{\ell_R}\left|R_p^{\ell_R}\right\rangle + \psi_L^{\ell_L}\left|L_p^{\ell_L}\right\rangle, \tag{4.20}$$

$$\left|R_p^{\ell_N}\right\rangle = \frac{1}{\sqrt{2}}e^{-i\ell_R\varphi}\left(\hat{e}_x - i\hat{e}_y\right),$$

$$\left|L_p^{\ell_S}\right\rangle = \frac{1}{\sqrt{2}}e^{-i\ell_L\varphi}\left(\hat{e}_x + i\hat{e}_y\right),$$

$$\psi_R^{\ell_R} = sin\,(\beta/2)\,,$$

$$\psi_L^{\ell_L} = cos\,(\beta/2)\,e^{+i\phi}.$$

We use the notation $|VL\rangle$ to represent a vector beam. The symbols $\left|R_p^{\ell_R}\right\rangle$ and $\left|L_p^{\ell_L}\right\rangle$ represent a pair of orthogonal eigenstates. Specifically, these eigenstates are right-circularly and left-circularly polarised LG beams, with OAM quantified as $\ell_R\hbar$, $\ell_L\hbar$, respectively. The symbols $\psi_R^{\ell_R}$, $\psi_L^{\ell_L}$ represent the coefficients of these two eigenstates, which are defined by relative intensity (variables $\beta \in [0,\pi]$) and relative phase ($\phi \in [0,2\pi]$). In the following text, six types of vector beams and VVBs, which are the research objects in this work, will be introduced.

In this work, to avoid ambiguity, light beams with spatially variant or inhomogeneous polarisation but no phase vortices are referred to as vector beams. Beams with both inhomogeneous polarisation and phase vortices are called VVB. Vector beams carry no OAM, whereas VVBs carry OAM due to their spiral phase fronts [165].

There are six different types of incident beams studied: radially polarised beam, three kinds of vector beams with hybrid polarisation states, “lemon” polarised, and “star” polarised vortex beams. These incident beams can be expressed by the superposition of two eigenstates [166, 167, 168]:

a. Radially polarised beams ($|\Psi^{R_{1st}}\rangle,\ \ell_R = 1, \ell_L = -1, \phi = 0$):

b. Vector beam with hybrid states of polarisation ($|\Psi^{R_{2nd}}\rangle,\ \ell_R = 2, \ell_L = -2, \phi = 0$):

c. Vector beam with hybrid states of polarisation ($|\Psi^{R_{3rd}}\rangle,\ \ell_R = 3, \ell_L = -3, \phi = 0$)

d. Vector beam with hybrid states of polarisation ($|\Psi^{R_{4th}}\rangle,\ \ell_R = 4, \ell_L = -4, \phi = 0$)

e. “Lemon” polarised vortex beams ($\left|\Psi^{lemon}\right\rangle,\ \ell_R = -1, \ell_L = -2, \phi = 0$):

f. “Star” polarised vortex beams ($|\psi^{star}\rangle,\ \ell_R = 1, \ell_L = 2, \phi = 0$):

The Brewster angle is an important property for dielectric materials. In this study, the reflection surface is set as the glass, and its Brewster angle of glass is around 56.6° [169]. When the angle of the incidence is equal to the material’s Brewster angle, only S-wave component is reflected [99] The polarisation state of the S-wave is orthogonal to the plane of incidence. Figure 4.5 shows the intensity and polarisation distribution of six types of beams mentioned earlier. Because the OAM modes carried by eigenstates of these beams are not zero, their intensity distributions exhibit doughnut shapes, with vanishing intensity at the centre. The size of the lines, which represent the polarisation states of that area, is proportional to the intensity of that area. Consequently, the polarisation states at the centre of the images are depicted by small points. The colormap from blue to white to red indicates increasing intensity. There are two columns in the figure: the first column shows the intensity and polarisation distributions of the six kinds of incident beams, and the second column displays those of their reflected beams when the incident angle is at the Brewster angle (56.6°).

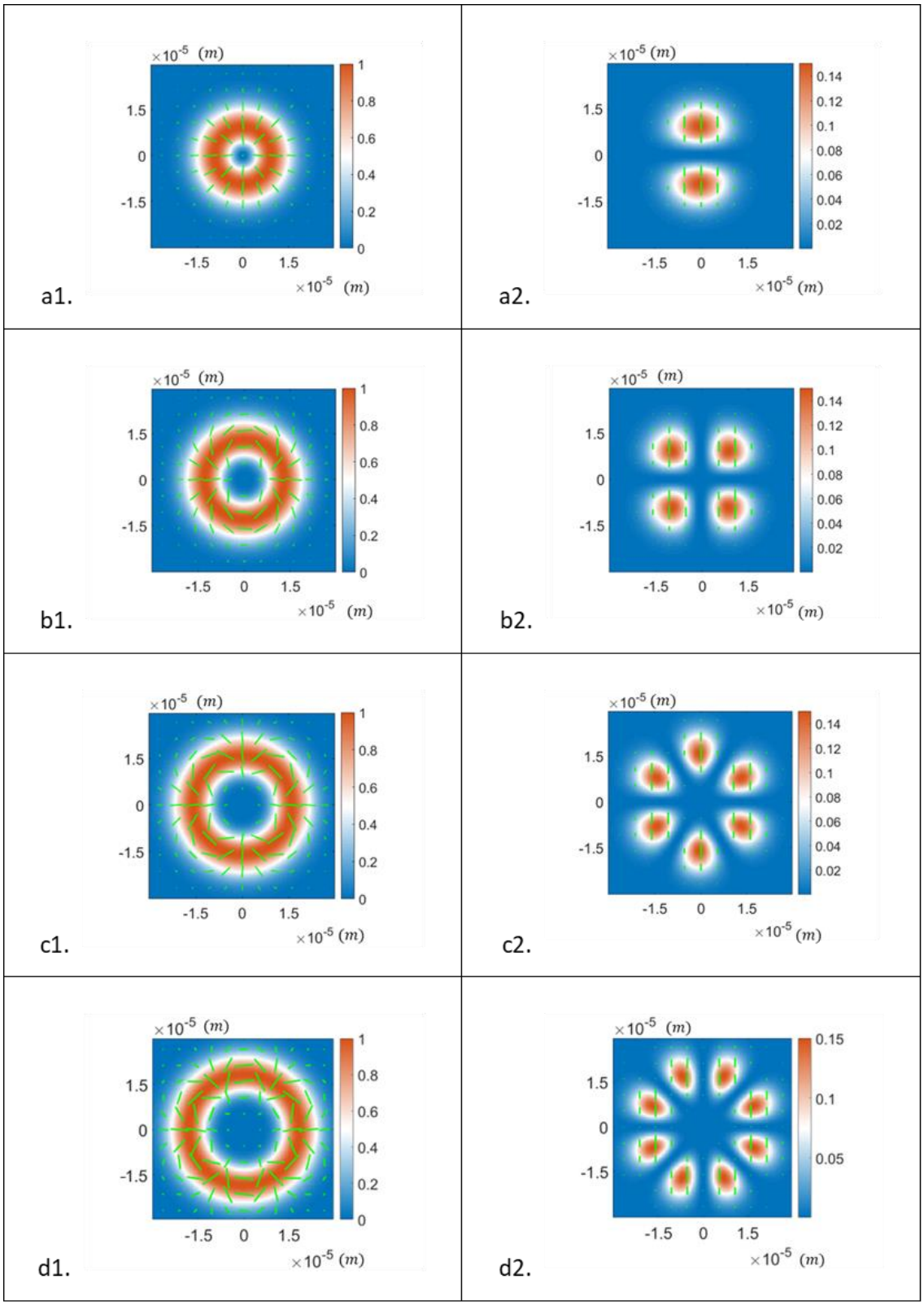
a1.
a2.
b1.
b2.
c1.
c2.
d1.
d2.
×10^-5 (m)
1.5
0
-1.5
0.8
0.6
0.4
0.2
0.14
0.12
0.1
0.08
0.06
0.04
0.02
0.15
0.05

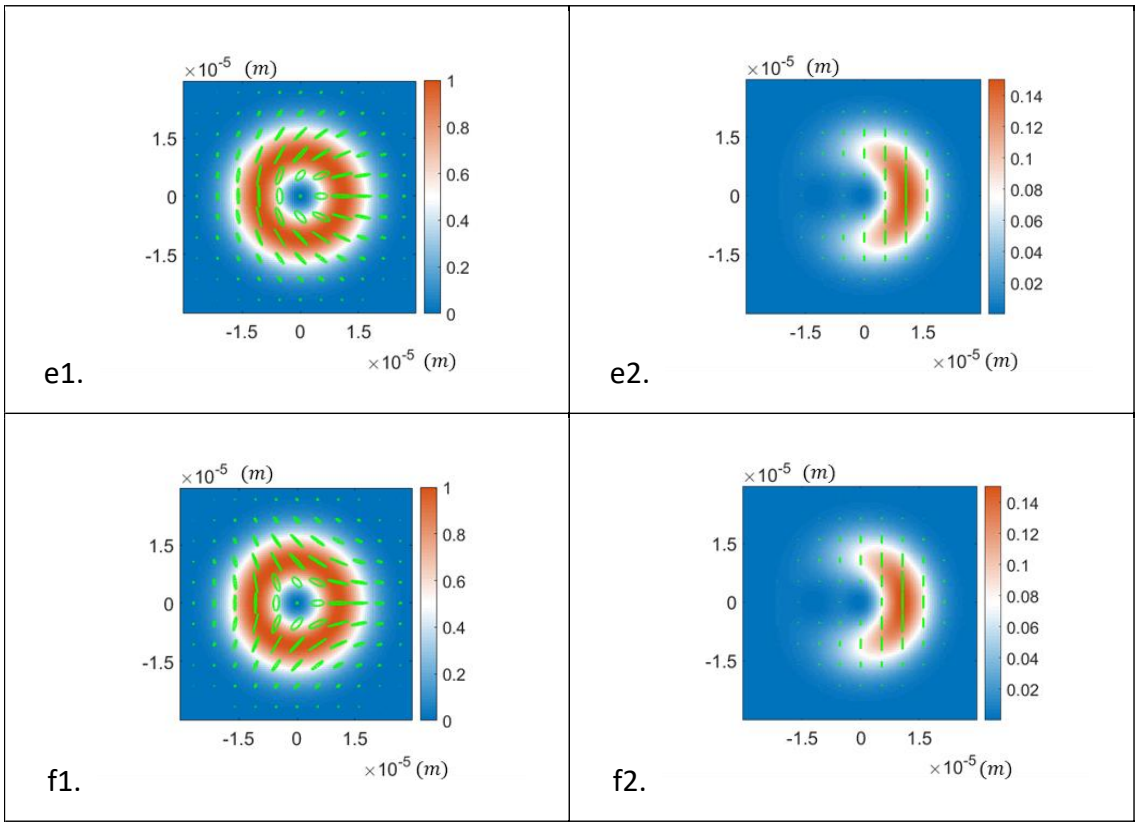

Figure 4.5 The first column shows the intensity and polarisation distribution of the incident beams. From (a1) to (f1) are the radially polarised beam, three types of VBs with hybrid states of polarisation ($|\Psi^{R_{2nd}}\rangle$, $|\Psi^{R_{3rd}}\rangle$ and $|\Psi^{R_{4th}}\rangle$, respectively), the "lemon"-polarised vortex beam, and the "star"-polarised vortex beam, respectively. The second column (from (a2) to (f2)) displays the intensity and polarisation distribution of the beams reflected on a glass surface when the incident angle is the Brewster angle (e.g., light shown in panel (a2) is the reflected field of the light shown in panel (a1)). Since the OAM modes carried by the above beams are not zero, their intensity distributions have doughnut shapes, with vanishing intensity at the centre. The size of the lines (representing polarisation states of that area) in the images is proportional to the intensity of that area; consequently, the polarisation states at the centre of the images are small points. The colormap from blue to white to red indicates increasing intensity.

4.3.2 Intensity Distribution of the Incident Beam and the Optical Field Reflected at the Brewster Angle in Azimuthal and Radial Coordinates (φ, r)

The reflected field, plotted in azimuthal and radial coordinates (φ, r), is studied. This approach provides us with another perspective to analyse the reflected field at different incident angles. The first column in Figure 4.6 displays the intensity distribution of the six kinds of incident beams plotted in a new coordinate system: azimuth ($-\pi \sim +\pi$) and radial coordinates (0~30 μm). The

intensity is normalised. It can be observed that the intensity distributions of these six incident beams exhibit symmetry along the azimuthal direction. The intensity distributions of these beams at the Brewster angle are also examined, and the results are shown in the second column of Figure 4.6. The colormap from dark blue to dark red indicates increasing intensity.

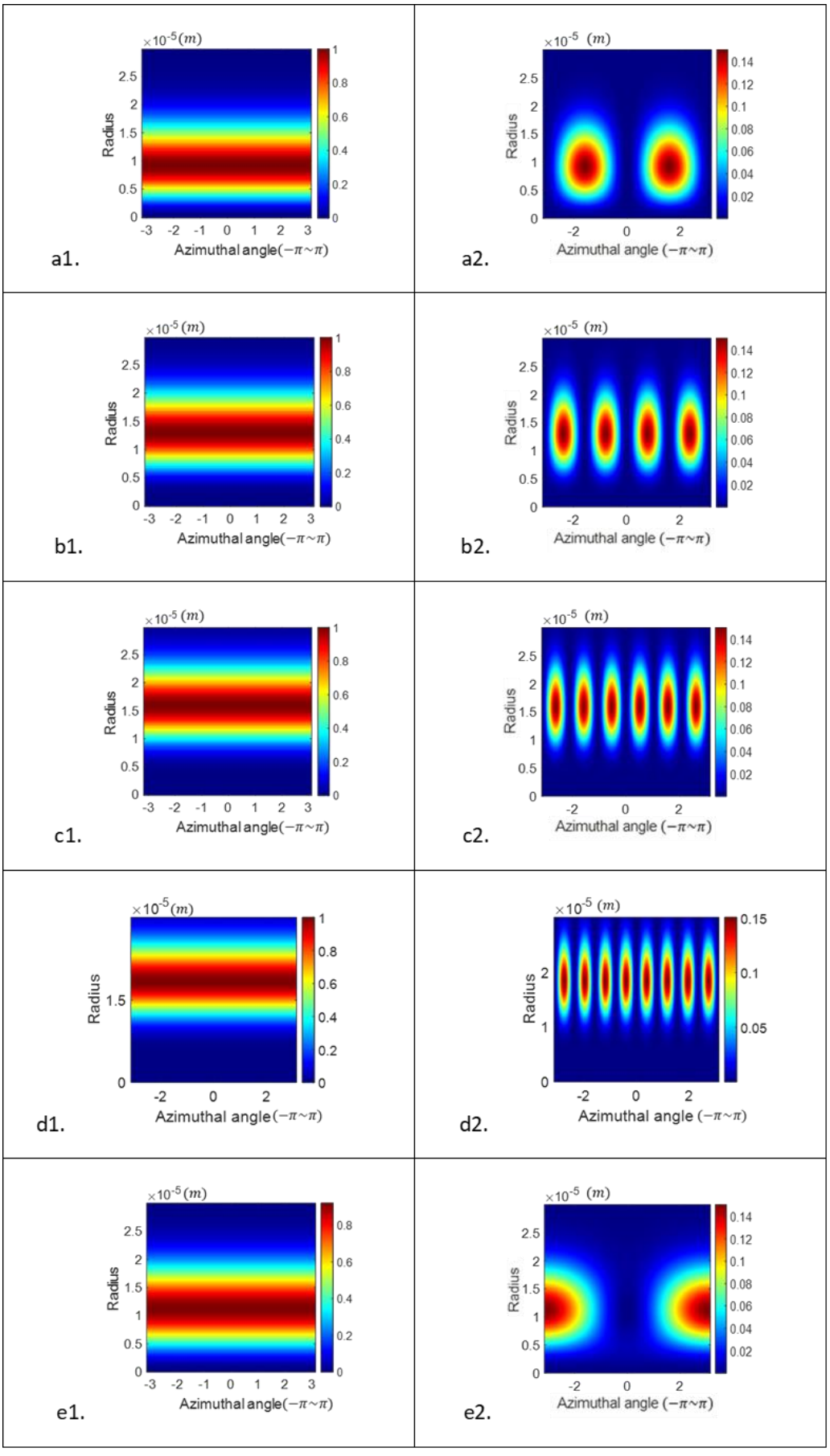
a1.
a2.
b1.
b2.
c1.
c2.
d1.
d2.
e1.
e2.
Radius
Azimuthal angle(−π~π)
Azimuthal angle (−π~π)
×10^-5 (m)

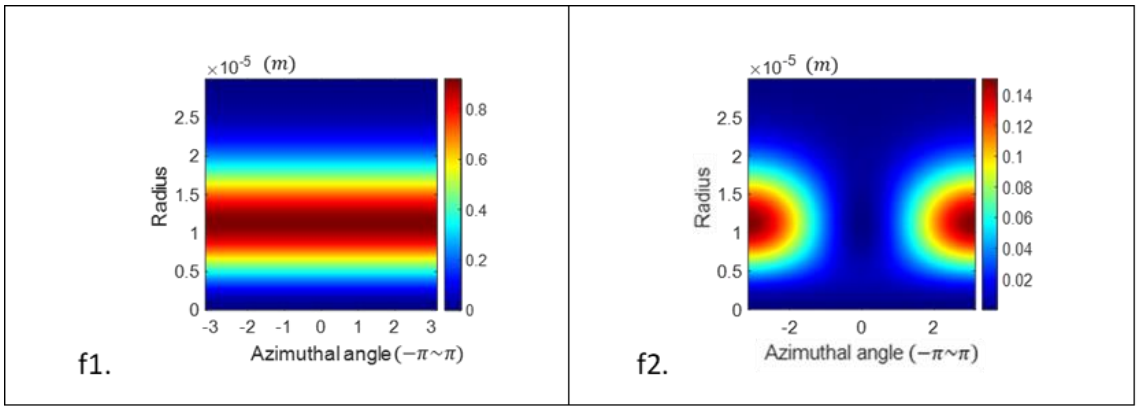

Figure 4.6 The first column shows the intensity distribution of the incident beams. From (a1) to (f1) are the radially polarised beam, three types of VBs with hybrid states of polarisation ($|\Psi^{R_{2nd}}\rangle$, $|\Psi^{R_{3rd}}\rangle$ and $|\Psi^{R_{4th}}\rangle$, respectively), the "lemon"-polarised vortex beam, and the "star"-polarised vortex beam, respectively. The second column (from (a2) to (f2)) displays the intensity distribution of the beams reflected on a glass surface when the incident angle is the Brewster angle (e.g., light shown in panel (a2) is the reflected field of the light shown in panel (a1)). These intensity distributions of incident beams arranged in the first column and reflected beams arranged in the second column are plotted in a new coordinate system: azimuth ($-\pi\sim+\pi$) and radial coordinates (0~30 μm). The colormap from dark blue to dark red indicates increasing intensity.

According to the intensity distributions shown in Figure 4.6, we observe that these beams have different beam widths. For the beams' eigenstates carrying OAM, the beam width is generally positively proportional to the modulus of the OAM. The eigenmodes' OAM of the four types of VBs (radially polarised beam and three types of VBs with hybrid states of polarisation) are $\pm1, \pm2, \pm3$, and ±4, respectively. Regarding the "lemon"- and "star"-polarised vortex beams, their eigenmodes include OAM modes with moduli 1 and 2, respectively. Therefore, the beam widths of the six types of incident beams are arranged in ascending order: radially polarised beam $<$ "lemon" $=$ "star" $<$ VB with hybrid states of polarisation ($|\Psi^{R_{2nd}}\rangle$ $<$ VB with hybrid states of polarisation ($|\Psi^{R_{3rd}}\rangle$ $<$ VB with hybrid states of polarisation ($|\Psi^{R_{4th}}\rangle$.

4.4 Discussion

In this section properties of the reflection field are explored and analysed: First, the variation of reflectivity with the incident angle is investigated. Next, the displacement of the intensity centroid of the reflected beam relative to the frame's centre is examined. Finally, the range of intensity of the reflected beam in (φ, r) coordinates is analysed.

4.4.1 Reflectance Variation across Incident Angles from 1° to 85°

The reflectance of six types of beams reflected at a glass surface has been investigated, and the results are shown in Figure 4.7. The incident angle ranges from 1° to 85°, with the reflectance trends of different incident beams plotted using various colours and markers as indicated in the legend.

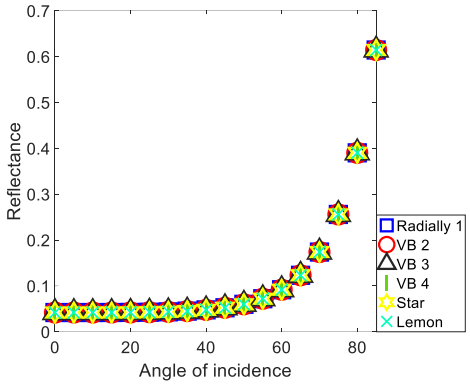

Figure 4.7 Trends of reflectance versus the incident angle. There are six kinds of beams studied: the radially polarised beam, three types of VBs with hybrid states of polarisation (denoted as "VB2" to "VB4" corresponding to $|\Psi^{R_{2nd}}\rangle$, $|\Psi^{R_{3rd}}\rangle$, and $|\Psi^{R_{4th}}\rangle$, respectively.), the "lemon"-polarised vortex beam, and the "star"-polarised vortex beams. These beams are reflected at the glass surface over an incident angle range of 1° to 85°.

In Figure 4.7, it can be observed that all curves overlap. More precisely, their trends are identical. This suggests that reflectance is independent of the type of incident beam but depends on the interface material and incident angle, as predicted by the Fresnel equations Eq. (4.18) and Eq. (4.19). Using vector beams and VVBs as the light source for LiDAR, the orientation of the reflective surface can be deduced by measuring the reflectance.

4.4.2 Shift in the Intensity Centroid of Reflected Beams across Incident Angles from 1° to 89°

Due to the Fresnel equations, different polarisation components of light exhibit varying reflectance, resulting in a noticeable variation in the intensity distribution of the reflected field with changes in the incident angle which indicates that we can find the relationship between the centroid of the intensity distribution of the reflected light field and the incident angle.

Firstly, we investigated the intensity distribution of four types of vector beams and found that their reflected light field exhibits central symmetry. Figure 4.8 illustrates the reflected field of the radially polarised beam as an example. The central symmetry of a radially polarised beam implies

that the centroid of its intensity distribution remains at the centre of the image, independent of the incident angle. Consequently, one cannot directly deduce the relationship between the centroid of the reflected beam's intensity distribution and the incident angle. To address this issue, we extracted a quarter of the reflected field's intensity distribution and determine the centroid of this quarter part. Specifically, the reflected field image comprises 1024 x 1024 pixels, but we analysed only the upper left 512 x 512 pixels. This is illustrated in Figure 4.8.

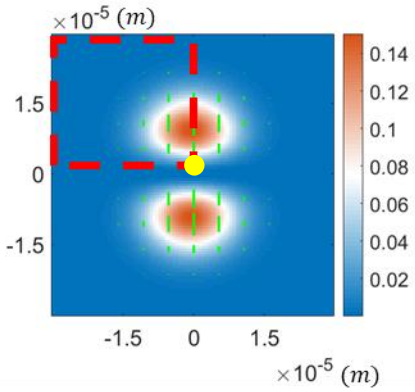

Figure 4.8 The extracted quarter part (the section framed by red dotted lines) of a reflected field, which is used to analyse the shift of the intensity centroid. The yellow point represents the centre of the original image.

The relationship between the centroid shift in the reflected light field and the incident angle is demonstrated in four graphs. For example, in group (I) of Figure 4.9, the following four images are presented: a. The relationship between pixel position in the x-direction of the centroid and the incident angle; b. The relationship between pixel position in the y-direction of the centroid and the incident angle; c. The centroid's movement across the transverse field of the reflected beam as it varies with the incident angle (colours ranging from blue to reddish brown indicate increasing incident angles); d. The variation in Euclidean distance from the centroid to the original image centre (referred to as centroid offset distance) with respect to the incident angle (colours ranging from dark green to shallow yellow indicate increasing incident angles). We observe that each incident angle corresponds to a specific coordinate of the centroid. However, near the Brewster angle, the Euclidean distance from the centroid to the image centre exhibits nearly axisymmetric characteristics. Additionally, the centroid coordinates of the intensity distribution of the reflected light field shift in the opposite direction at the Brewster angle, and the centroids of some large-angle incident reflection fields approximately overlap with those of small-angle incident fields.

I. The radially polarised beam

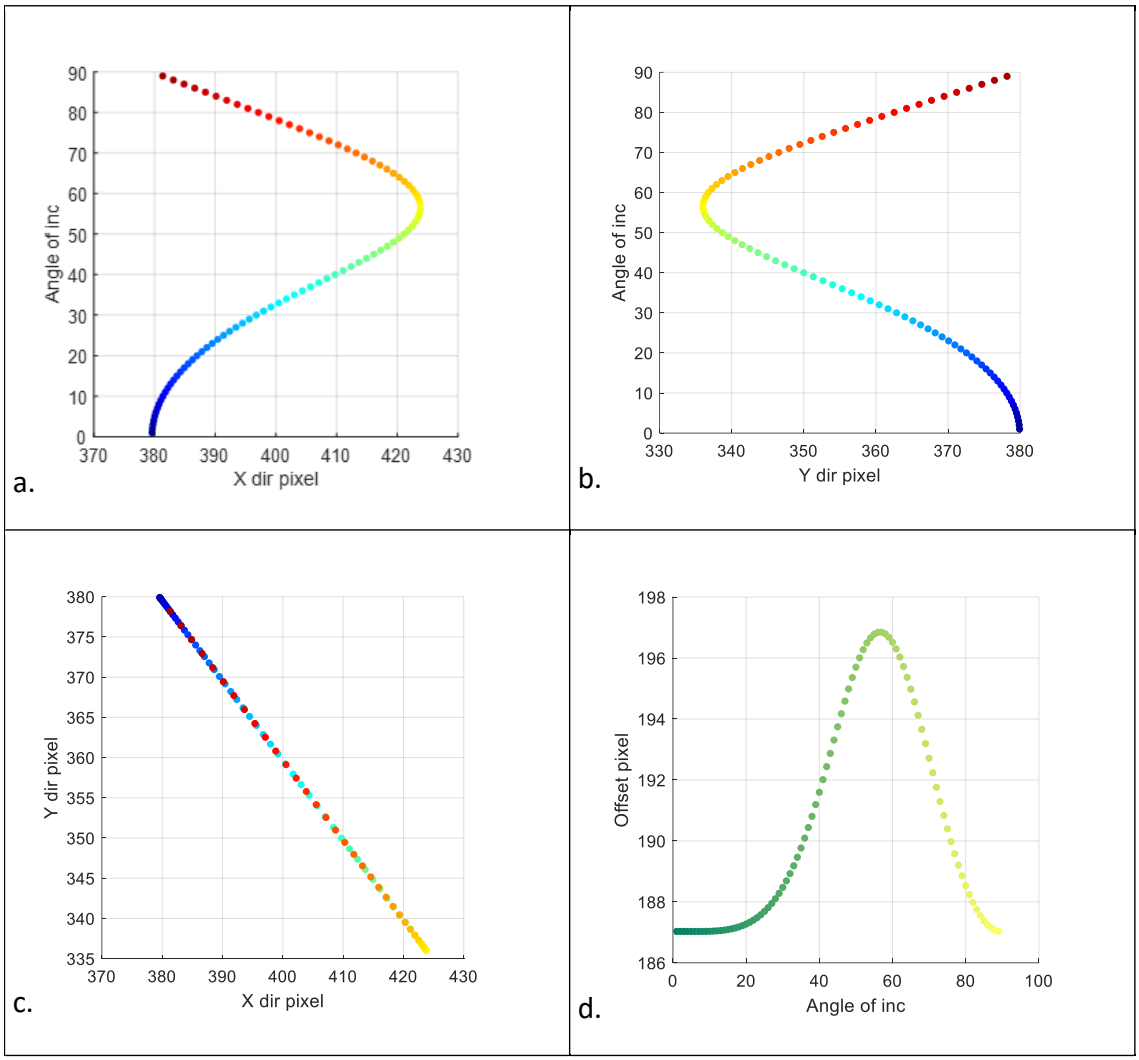

II. The vector beam with hybrid states of polarisation ($|\Psi^{R_{2nd}}\rangle$

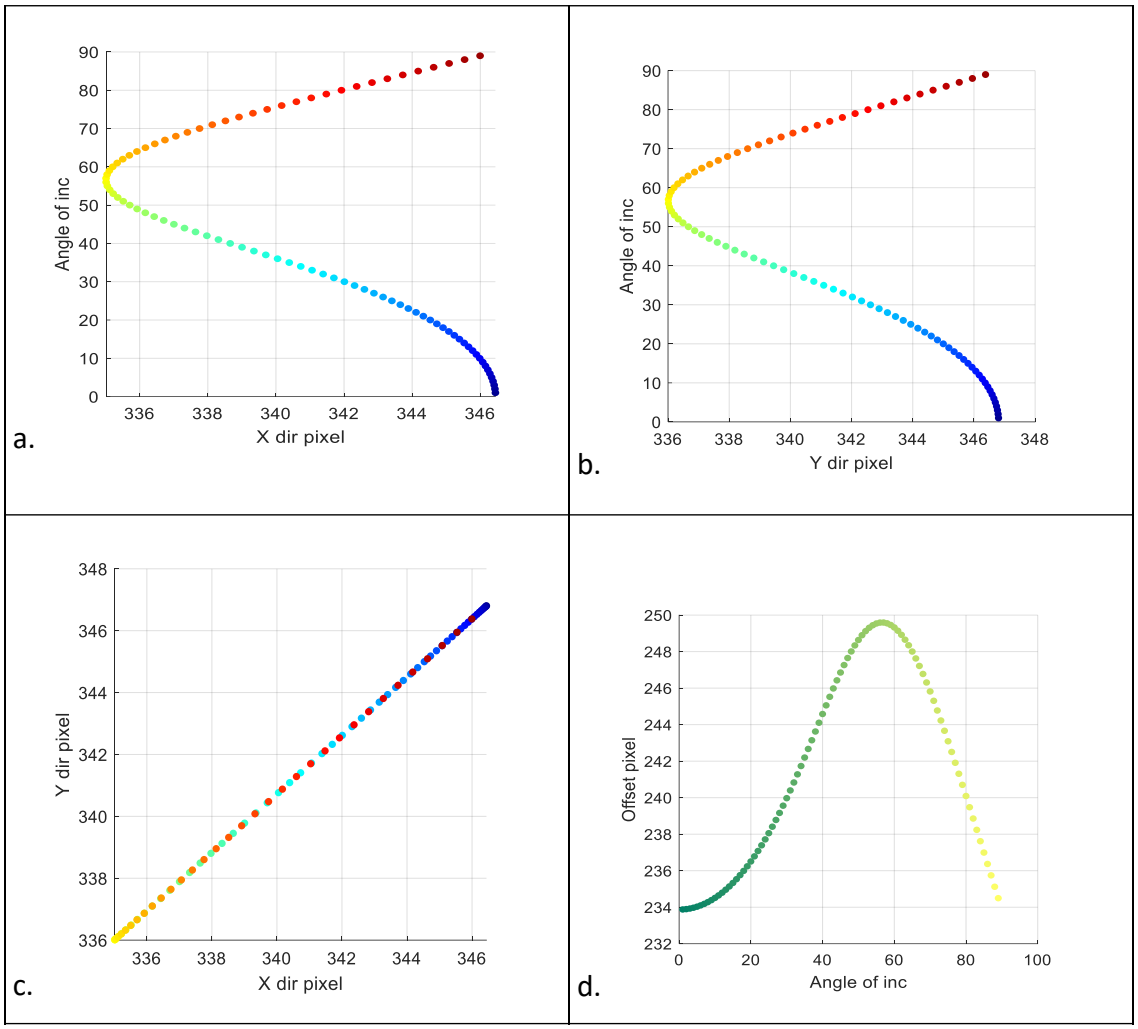

III. The vector beam with hybrid states of polarisation ($|\Psi^{R_{3rd}}\rangle$

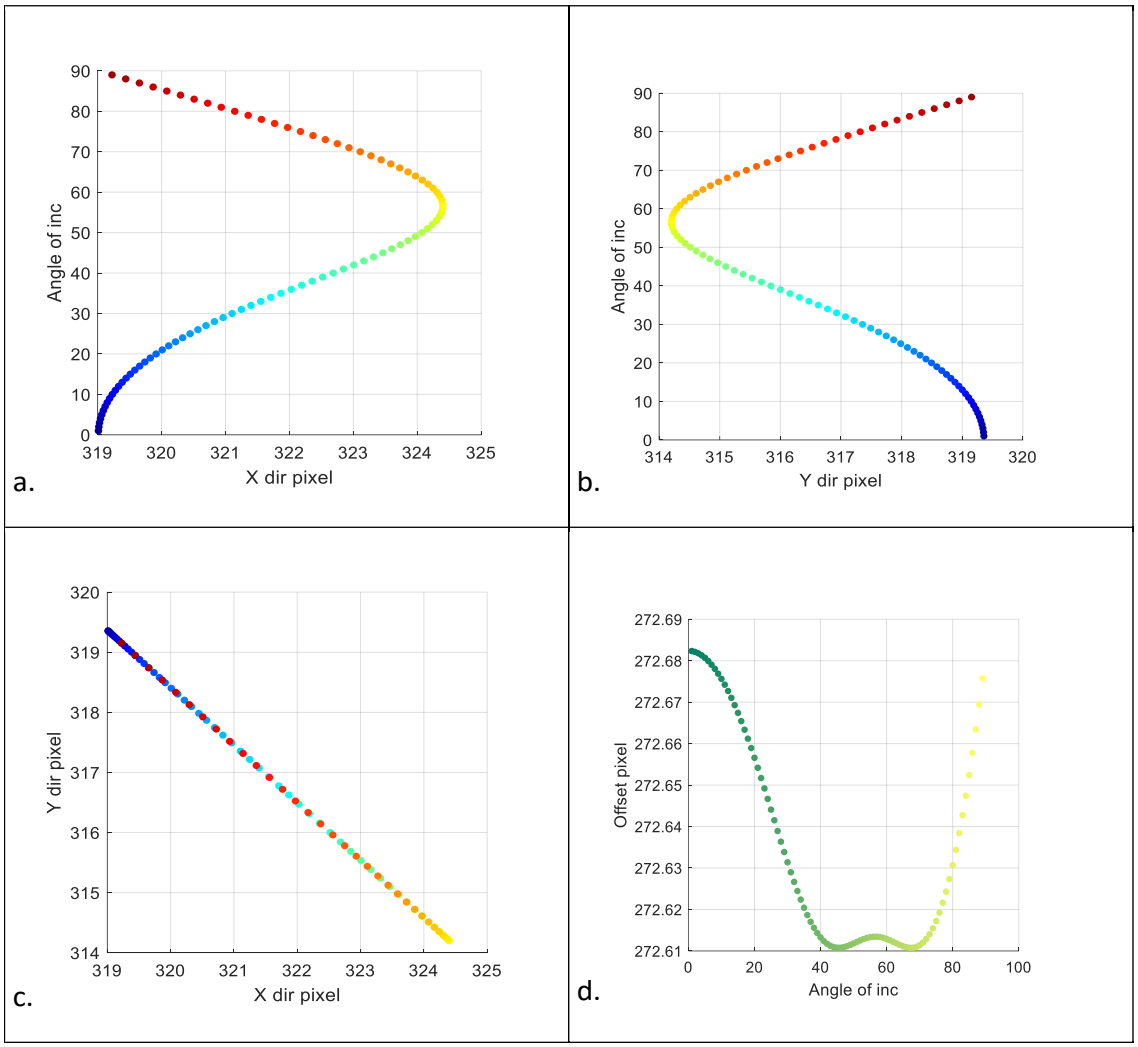

IV. The VB with mixed polarisation states ($|\Psi^{R_{4th}}\rangle$

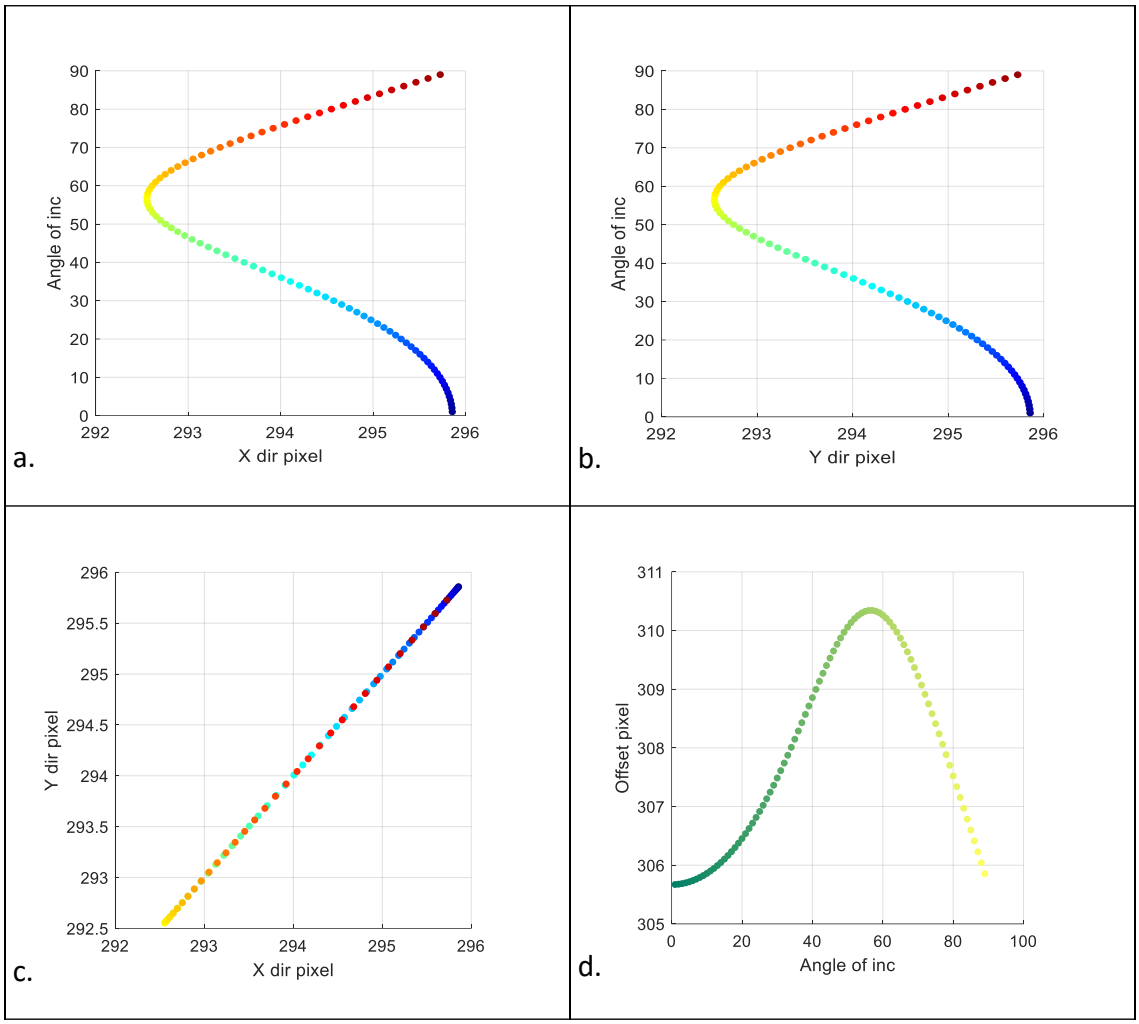

Figure 4.9 Four groups of graphs. Groups labelled “I” through “IV” represent the radially polarised beam and three types of VBs with hybrid polarisation states, respectively. Each group includes four images labelled (a) through (d): (a). the relation between pixel position in the x-direction of the centroid and the incident angle; (b). the relation between pixel position in the y-direction of the centroid and the incident angle; (c). the centroid’s motion within the transverse field of the reflected beam varying with the incident angle (colours ranging from blue to reddish brown indicate increasing incident angles (1°~89°)); (d). the variation in Euclidean distance (referred to as “offset pixel” in the diagram) from the centroid to the original image centre (depicted as a yellow point in Figure 4.8) with respect to the incident angle (colours ranging from dark green to shallow yellow indicate increasing incident angles (1°~89°)).

By comparing panels (a) and (b) of the four types of VBs in Figure 4.9, we find that the coordinate shifts of the intensity centroid of the radially polarised beam are larger. Furthermore, we can determine the order of the coordinate shifts of the intensity centroid of the reflected field in the x and y directions, from largest to smallest, as the incident angle varies: radially polarised beam >

vector beam with hybrid polarisation states ($|\Psi^{R_{2nd}}\rangle$ > vector beam with hybrid states of polarisation ($|\Psi^{R_{3rd}}\rangle$ > vector beam with hybrid states of polarisation ($|\Psi^{R_{4th}}\rangle$. Additionally, according to panels (d) of the four types of vector beams, the distribution of offset pixels is axisymmetric with respect to the Brewster angle axis. This suggests that deducing the incident angle solely from the centroid coordinates or the centroid's offset distance relative to the centre of the image is a challenge. To ascertain whether the incident angle is less than or greater than the Brewster angle, it is necessary to measure the energy of the reflected field.

Additionally, the change in the shift of the intensity centroid of the reflected field for "lemon" and "star"-polarised vortex beams is also characterised. Unlike the four vector beams, the intensity distribution of the reflected fields of these two no longer exhibits rotational symmetry relative to the centre of the image. Consequently, in the following section, there is no partial extraction analysis of the intensity distribution of the reflected field. All results are shown in Figure 4.10.

i. "Lemon"-polarised vortex beam

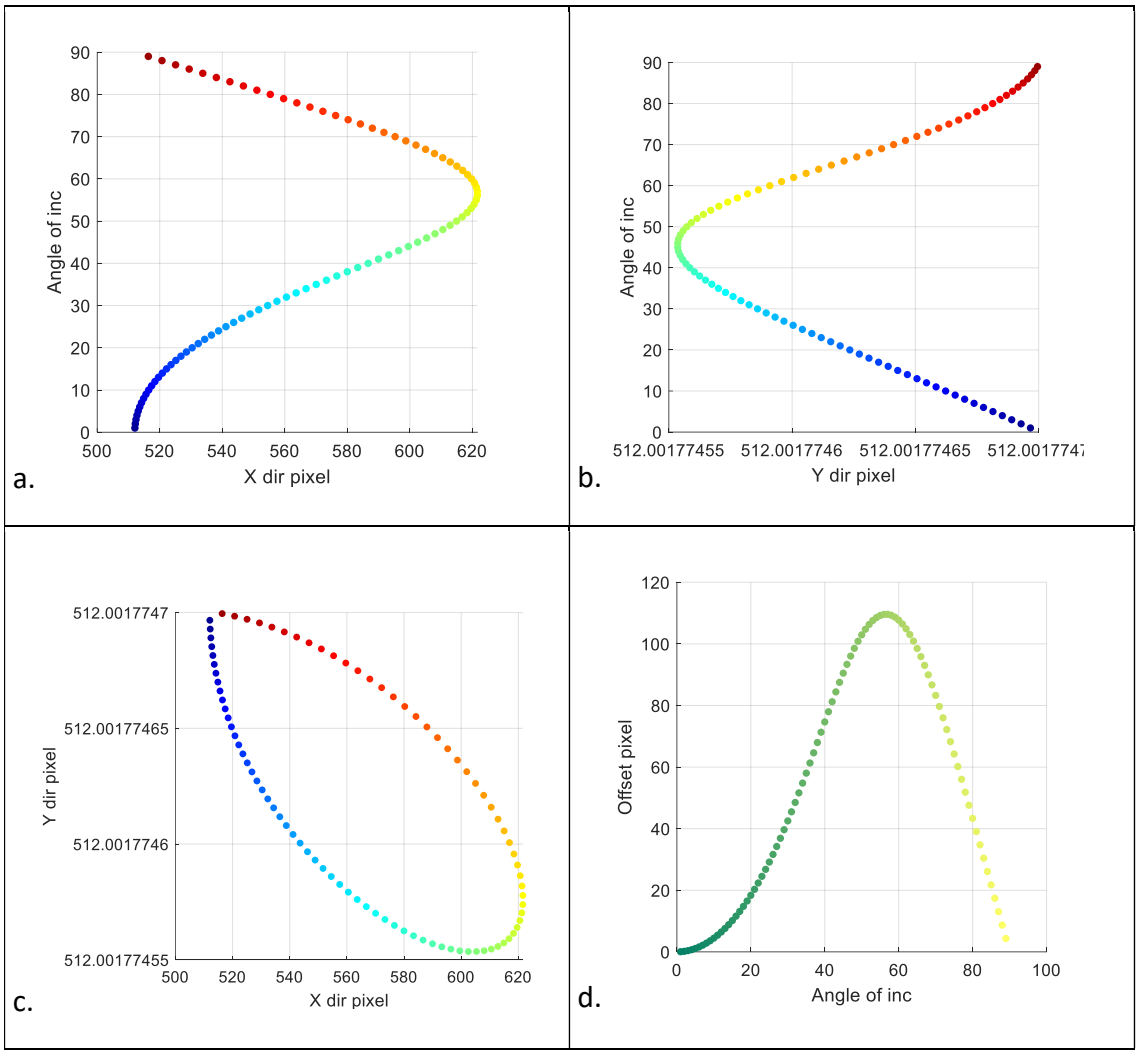

ii. "Star"-polarised vortex beam

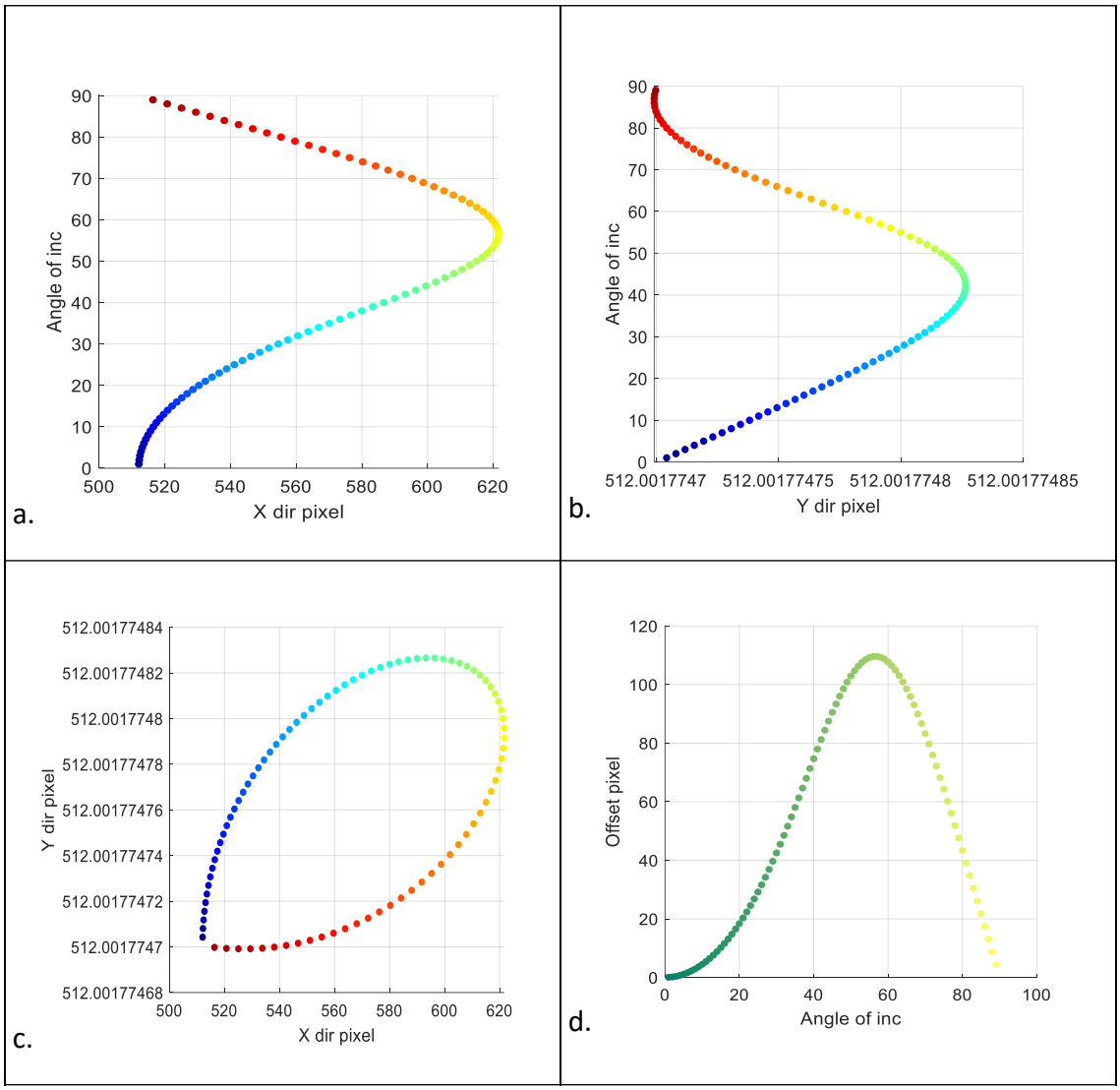

Figure 4.10 Two groups of images. Groups labelled (i) and (ii) represent “lemon”- and “star”-polarised beams, respectively. Each group includes four images labelled (a) through (d): (a) the relation between pixel position in the x-direction of the centroid and the incident angle; (b). the relation between pixel position in the y-direction of the centroid and the incident angle; (c). the centroid’s motion within the transverse field of the reflected beam varying with the incident angle (colours ranging from blue to reddish brown indicate increasing incident angles (1°~89°)); (d). the variation in Euclidean distance (referred to as “offset pixel” in the diagram) from the centroid to the image centre (depicted as a yellow point in Figure 4.8) with respect to the incident angle (colours ranging from dark green to shallow yellow indicate increasing incident angles (1°~89°)).

It can be observed that the shift of the intensity centroid of the two types of VVBs is almost the same: the centroid moves primarily in the x-direction, and according to the panels (b) of the two VVBs, we can see that the centroid remains nearly unchanged in the y-direction. Additionally, the

range of the centroid shift in the x-direction is much larger than that of the four types of vector beams. The axial symmetry shown in two panels (d) is similar to that of the four types of VBs; the distribution of offset pixels is axisymmetric with respect to the Brewster angle axis. However, unlike those four VBs, the range of the pixel coordinate shifts of the intensity centroid of the reflected field relative to the pixel coordinates of the field origin is larger. Deducing the value of the incident angle from the pixel coding coordinates of the centroid of the reflected field intensity may not be sufficient. However, in scenarios where the incident angle is smaller than the Brewster angle, or the target object undergoes small-axis rotation, the incident angle can be deduced solely from the coordinates of the centroid of the reflected field intensity. Moreover, when focusing solely on the range of the pixel coordinate shifts of the intensity centroid of the reflected field relative to the pixel coordinates of the field origin, using “lemon” and “star”-polarised vortex beams as detection signals is better.

4.4.3 Range of the Intensity of the Reflected Fields in the (φ, r) Coordinates

Although the intensity distributions of the six types of incident beams are rotationally symmetric (as shown in Figure 4.6), their intensity remains unchanged along the φ direction, and the intensity distributions of the reflected beams no longer remain unchanged along the φ direction. This inspired this study to find the relationship between the angle of incidence and intensity distribution of the reflected beam.

Therefore, we extracted the reflected beams’ intensity data for all points at coordinates r = 11.28 μm. Then the minimum value and maximum value are found to calculate range of the intensity. We examined the intensity ranges of the reflected beams for incident angles ranging from 1° to 89°. Figure 4.11 shows graphs of the relation of the angle of incidence and the intensity range.

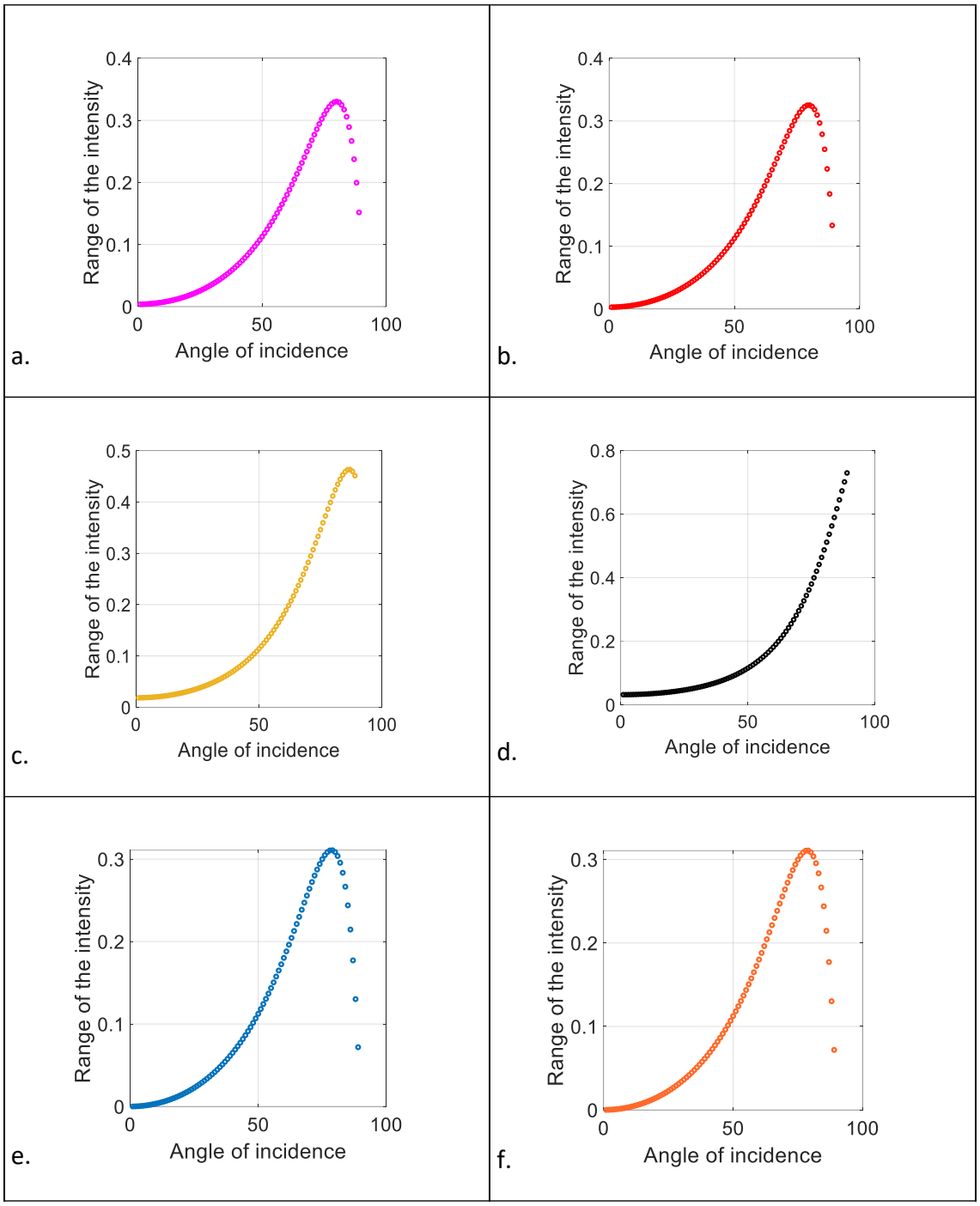

Figure 4.11 The relationship between the angle of incidence and the intensity range. The intensity data of the reflected beams (in the (φ, r) coordinates) at all points with r = 11.28 µm are extracted, and the minimum value and maximum value are determined to calculate the range. The intensity ranges of the reflected beams for incident angles ranging from 1° to 89° are examined. Panels (a–f) correspond to the radially polarised beam, three types of VBs with hybrid states of polarisation ($|\Psi^{R_{2nd}}\rangle$, $|\Psi^{R_{3rd}}\rangle$ and $|\Psi^{R_{4th}}\rangle$, respectively), "lemon"-polarised vortex beam, and "star"-polarised vortex beams, respectively.

Based on the above graphs, several characteristics can be observed:

1. Except for the vector beam with hybrid states of polarisation $|\Psi^{R_{4th}}\rangle$, the trend of the other five types of beams shows multivalued properties;

2. Range of the intensity of the vector beam with hybrid states of polarisation $|\Psi^{R_{4th}}\rangle$ is greater than that of other beams;

3. For the four types of vector beams, the higher the modulus of OAM carried by their eigenstates, the better the performance in deducing the incident angle from the intensity range;

4. The trend shown in graphs (e) and (f) of the “lemon” polarised and “star” polarised vortex beams is the same.

In experiments and practical engineering, we can use area-array CCDs and line-array CCDs to measure the intensity distribution of the light field. Line-array CCDs are more widely used in practical applications. This is because area-array CCDs are expensive, while line-array CCDs are more affordable and can be manufactured with many pixels. By using a line-array CCD in conjunction with a scanning mechanism and position feedback system, the radial intensity distribution of the light field mentioned in the text can be measured. Then, the measurement of the orientation of the reflecting surface can be achieved.

4.5 Conclusion

In this chapter, the potential of using VBs and VVBs as detection signals for LiDAR sensors to measure the orientation of reflecting surfaces is explored. We develop a computational model for these beams’ reflection. With the help of this model, the relationship between the properties of reflected optical fields and incident angles, focusing on reflectance, intensity centroid shifts, and the intensity range of the reflected beam in the azimuthal direction, is examined. The findings suggest that the “lemon”- and “star”-polarised vortex beams are good choices among the six types of beams, as their ranges of the centroid shift in the x direction are much larger. Additionally, the vector beam with hybrid states of polarisation ($|\Psi^{R_{4th}}\rangle$) stands as another good choice because its range of intensity variation correlates monotonically with the incident angle, and this range is greater than that of the other five types of beams. In summary, this work provides a new sensing scheme for LiDAR research.

Chapter 5 Spatiotemporal Optical Vortices and Optical Toroidal Pulses

This chapter studies two types of optical fields: the spatiotemporal optical vortex and the optical toroidal pulse. The structure of this chapter is divided into two parts according to these two types of optical vortices. In the first part, the method for calculating the transverse OAM, sometimes termed spatiotemporal OAM (ST-OAM), of the spatiotemporal optical vortex (STOV) is demonstrated. Previous work on this topic by two independent research groups has been published, but they arrived at different conclusions and omitted some details in their calculations. Therefore, this chapter provides a detailed calculation and analysis. In the second part, inspired by the definition of the angular momentum of light, a new physical quantity for a new type of optical pulse termed "toroidal pulse" is defined and discussed. This new quantity is temporarily referred to as "toroidal momentum". Fundamental concepts of transverse OAM and STOV are detailed in section 1.2.3. Please refer to that section before reading this chapter.

5.1 Introduction

5.1.1 Spatiotemporal Optical Vortex

Because the time dimension is introduced in the optical field leading to some intriguing optical fields such as spatiotemporal optical vortices (STOV) [48, 49,50, 51], optical Hopfions [170], EM-pulse [171], and more. These have emerged as highly popular research directions in recent years. In 2012, Konstantin Yu. Bliokh and Franco Nori expanded the concept of intrinsic OAM and optical vortices to polychromatic states in space-time [41]. Under the assumption that the polarisation states of the optical field can be neglected, the result reveals that the existence of STOV with non-longitudinal OAM arises from the necessity of relativistic invariance and can be achieved through Lorentz transformations of spatial vortex beams. Consequently, spatiotemporal OAM-carrying optical fields can naturally generate from moving sources (monochromatic) emitting stationary vortex states in their rest frames. These findings have implications in several research areas, including the optics of moving media [172], quantum communications with satellites [173], collisions involving high-energy particles with OAM [174], and the astrophysical applications of OAM in light [175,176].

Afterwards, the STOV carrying a purely transverse OAM generated experimentally was reported in two studies [177,51]. Figure 5.1 [51] shows a schematic diagram for the experimental and measurement setup.

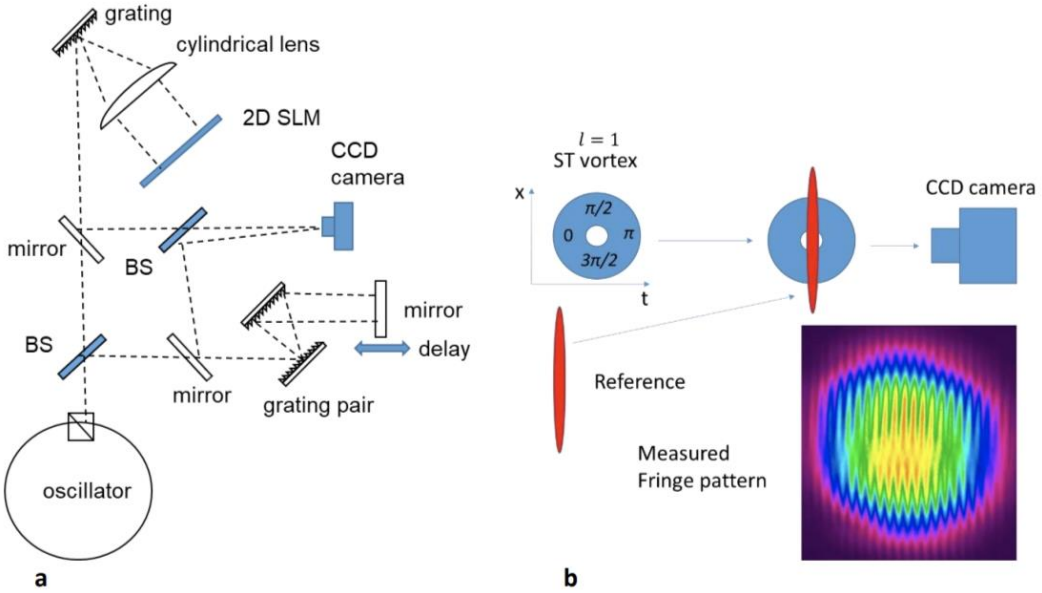

Figure 5.1 Panel (a) [51] details the experimental and measurement setup. Mode-locked pulses from a fibre oscillator are positively chirped to about 3 ps. A chirped STOV is generated by applying a spiral phase using a 2D SLM on the pulse shaper. Simultaneously, a short reference pulse (~90 fs) is produced by compressing the pulse with a pair of gratings. BS: beam splitter, SLM: spatial light modulator, CCD: charge-coupled device. Panel (b) [51] shows the diagram of the phase measurement method. Italic numbers show relative phases for the STOV with topological charge of $\ell = 1$ at different points. The STOV and the short reference pulse are then overlapped with a delay to produce a spatial fringe pattern on the CCD camera. These spatial fringe images at various delays are used to reconstruct the STOV's phase profile.

The calculation of the transverse OAM of the STOV pulse, has been a hot and controversial topic in recent years. This research is primarily represented by two groups, with Konstantin Yu. Bliokh and S. W. Hancock as the first authors. The research results from these two groups present different conclusions, leading to two rounds of debates on this disagreement. The development of the research on the calculation of the transverse OAM (denoted as L_y) is both controversial and interesting. The following table shows the timeline of this study:

Table 5.1 A table showing the timeline of the two research groups on the calculation of transverse OAM:

	Round 1	Round 2
Konstantin Yu. Bliokh	Ref. [178] published in June 2021.	1. Ref. [179] published in March 2023. 2. Ref. [180] published in June 2023.
S. W. Hancock	Ref. [181] published in November 2021.	Ref [182] published in July 2023.

Before delving into the details of the two research groups' work, some assumptions about the STOV will be introduced. Suppose the STOV is circularly symmetric and propagates along the z -axis. In addition, it is uniformly polarised in the direction of the y-axis. Its angular spectrum is shown in Figure 5.2. There are two principal axes (major axis and minor axis) shown in the figure. The ratio of the radii along the major axis and minor axis, i.e., $\gamma = r_{major}/r_{minor}$, is used to describe the ellipticity of the STOV. If $\gamma = 1$, the STOV is circularly symmetric. The phase of the plane-wave amplitudes ($\psi \propto e^{i\ell\varphi}$) is depicted by the colormap, where φ is the azimuthal angle of polar coordinates in the x-z plane. The topological charge of the phase dislocation is 4 ($\ell = 4$).

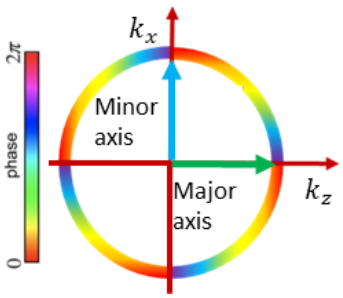

Figure 5.2 shows a schematic diagram for the angular spectrum of a circularly symmetric STOV. The ratio γ of the radii along the major axis and minor axis equals 1. The phase of the plane-wave amplitudes ($\psi \propto e^{i\ell\varphi}$) is depicted by the colormap, where φ is the azimuthal angle of polar coordinates in the k_x-k_z plane. In this figure, $\ell = 4$.

According to the two rounds of debates on the disagreement regarding the value of the transverse OAM carried by a circularly symmetric STOV, details of the two groups' work are shown in Table 5.2.

Table 5.2 A table showing the details of research on transverse OAM calculation by two groups

1) **The 1st round**
Konstantin Yu. Bliokh: In this work (Ref. [178]), for a circularly symmetric STOV in a vacuum, the transverse OAM is quantised in multiples of 1. If the STOV is elliptical, the transverse OAM is quantised in integer multiples of $\frac{\gamma+\gamma^{-1}}{2}$.
S. W. Hancock: For a symmetric STOV propagating in vacuum, the transverse OAM is quantized in multiples of $\frac{1}{2}$; In a dispersive medium, it is quantized in integer multiples of $\frac{(\gamma-\beta_2/2)}{2}$, where β_2 is the normalized group velocity dispersion of the material.
2) **The 2nd round**
Konstantin Y. Bliokh: In ref. [179], an explanation is provided for the difference in the results of the value of the transverse OAM. Konstantin considers that the transverse OAM discussed in S. W. Hancock's work [181] is the total transverse OAM, while the transverse OAM studied by Konstantin Y. Bliokh is the intrinsic part of the transverse OAM. This work provides expressions for the intrinsic (L^{int}) and extrinsic parts of the transverse OAM (L^{ext}). They are: $$L^{int} \cong \ell \frac{\gamma+\gamma^{-1}}{2}, L^{ext} \cong \frac{-\ell}{2\gamma} \quad (5.1)$$ Where ℓ is the topological charge of the phase dislocation, which is defined in the phase term of the electric field expression of the pulse: $E \propto e^{i\ell\varphi}$. Here, φ is the azimuthal angle in polar coordinates in the x-z plane. x is a component in the transverse direction, and z is the pulse's propagation direction. For a circularly symmetric pulse ($\gamma=1$), $L^{int} = \ell$. The extrinsic aspect of the OAM is due to plane waves having the same amplitude but different frequencies within the pulse spectrum, leading to varying photon densities. This results in a transverse, vortex-dependent shift of the photon centroid, even in a STOV with a uniform energy-density distribution. In addition, in ref. [180], Konstantin discussed the subluminal propagation of the light pulse. Konstantin considers that the subluminal propagation of the wave packet centroids does not contradict the propagation of signals or information transfer at the speed of light. The wave packets under consideration are solutions that are infinitely extended in both space and time.

S. W. Hancock: This work (ref [182]) claims that if any flow occurred along z-axis, it would be superluminal or subluminal above or below the vortex singularity (depending on the sign of the STOV), violating special relativity. Any valid angular momentum quantity should be conserved during propagation. Additionally, the researcher considers that we cannot treat ξ and x as equal position quantities, and the operator of the transverse OAM should be defined as:

$$L_y = -i\left(\xi\frac{\partial}{\partial x} - \beta_2 x\frac{\partial}{\partial \xi}\right) \tag{5.2}$$

Where x and β_2 represent the position along the x-axis and the normalized group velocity dispersion of the material, respectively. The symbol ξ represents the position in the direction of propagation, defined as $\xi = v_g t - z$, where v_g is the group velocity [183] of the STOV, t represents time, and z is the position of the STOV along the z -axis.

By comparing the results shown in their research, it can be found that in the first round, their contradiction is: The values of transverse OAM differ by a factor of 2 for a circular STOV pulse. After that, in the second round, Konstantin provides an explanation for the contradiction, stating that the transverse OAM calculated by him is the intrinsic part of the transverse OAM, whereas Hancock's work considers the total transverse OAM. However, Hancock does not agree with this explanation. Firstly, he considers that research cannot treat ξ and x as equal position quantities, as shown in Konstantin's work. The operator for intrinsic transverse OAM should have the form shown in Eq. (5.2).

Apart from the controversy on calculations of transverse OAM, the experimental detection results of the phase distribution of the STOV differ from its numerical results. The numerical results are shown in the works [41, 179] by Konstantin et al. There are fork-like dislocations in the phase distribution of the STOV, as shown in Figure 5.3. However, there are no fork-like distributions in the experimental results shown by Hancock et al. [177], as depicted in Figure 5.4.

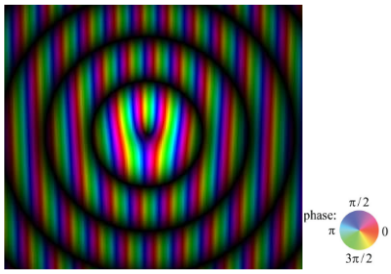

Figure 5.3 The intensity (brightness) and phase distribution (colormap) of the spatiotemporal light pulse in numerical results.

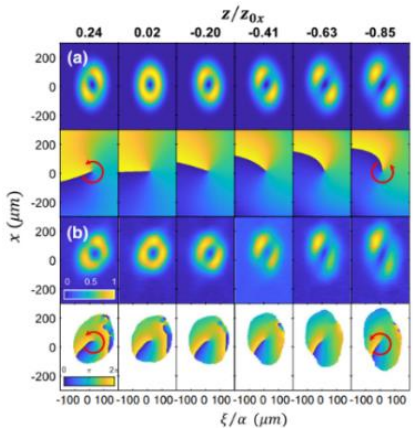

Figure 5.4 The phase distribution for the spatiotemporal light pulse in experimental results [181].

5.1.2 Toroidal Pulse

Figure 5.5 illustrates the schematic representation of an optical toroidal pulse. R_0 is the radius of the toroidal light pulse. The iso-surface of the pulse closely resembles that of a donut's surface, which is formally known in mathematics as a "torus". A torus is a three-dimensional surface formed by combining two circular motions: a primary large circle ("pulse local coordinate") centred around the main torus axis (marked "ς" in the figure), and a series of smaller circles ("local coordinate fixed to transverse OAM" or "poloidal coordinate") perpendicular to the first circle and centred at various points along the large circle.

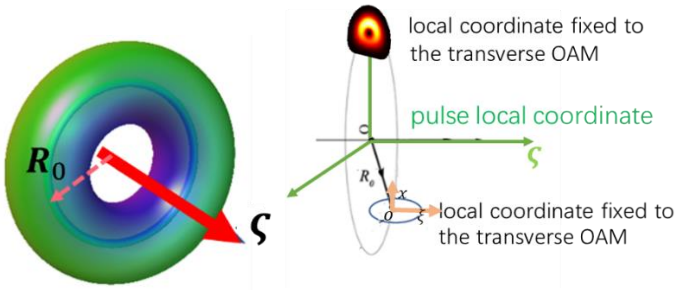

Figure 5.5 shows a schematic diagram for an optical toroidal pulse and its local coordinates; local coordinates are fixed to transverse OAM. R_0 is the radius of the toroidal light pulse represented by the pink dashed ray. And ς -axis is the main torus axis.

The generation of isolated tori in the electromagnetic field was reported independently by two research teams in 2022, marking the first-ever appearance of such findings in Nature Photonics [171, 184, 185]. In this work [184], the toroidal pulse is generated by a STOV tube (an elongated STOV). Then, by means of the conformal mapping, a toroidal light pulse can be generated. Figure 5.6 is the schematic diagram for the generation process of the toroidal pulse.

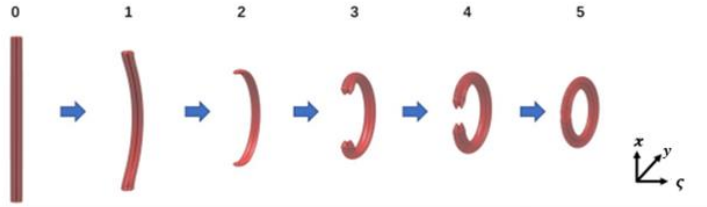

Figure 5.6 shows a schematic diagram for "bending" a STOV tube into an optical toroidal pulse [184]

By means of the conformal mapping, the formula of the toroidal pulse is:

$$\Psi^T(x,y,\varsigma) \propto e^{-\left(\frac{(R-R_0)^2+\varsigma^2}{w^2}\right)} e^{i\ell\phi} e^{-ik_0\varsigma} \iint dk_r d\Delta\omega J_\ell(k_r r)\,\widetilde{\psi}(k_r;\Delta\omega), \tag{5.3}$$

where R represents radial coordinates defined in the x-y plane in the pulse local coordinates system. R_0 is the radius of the toroidal light pulse depicted in Figure 5.5. The coordinates (r,ϕ) are the local polar coordinates fixed to transverse OAM carried by the toroidal pulse in the x,ς plane. This chapter follows the method of the work [184], using the scalar toroidal light pulse as the research object to conduct some exploratory work on the definition of a quantity temporarily named "toroidal momentum". Figure 5.7 shows the intensity and phase distribution, represented by brightness and colormap, respectively, of a toroidal light pulse generated by a STOV tube with the transverse OAM with topological charge of 1.

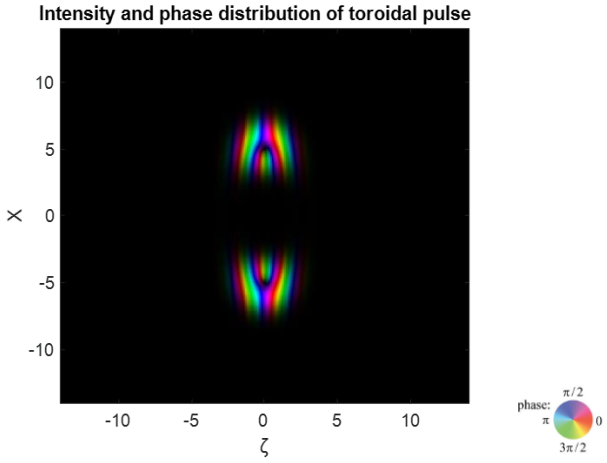

Figure 5.7 The intensity (brightness) and phase distribution (colourmap) of an optical toroidal pulse

5.2 Transverse Orbital Angular Momentum of a z-Localized Spatiotemporal Optical Vortex

Figure 5.8 is a schematic diagram for the angular spectrum of a STOV [41]. For the simplicity, the ellipticity of the distribution of the k_x and k_z has been ignored ($\gamma=1$, assuming the shape of this

distribution is a perfect circle), and this optical field has a polarisation transverse (e.g., the direction of y-axis) to the optical axis (z-axis). The colormap represents phases of the plane-wave amplitudes.

Therefore, this STOV can carry transverse OAM (represented by a red vector in the figure named "L") having a 2D spatiotemporal wave packet, which is a slowly varying envelope with a carrier term $\exp(ik_0z - i\omega_0t)$. This kind of optical field is also termed light sheets [40]. The symbol Δ is the radius of the spectrum of the light pulse shown in Figure 5.8, which characterises the monochromatic degree of the light pulse. Therefore, the parametric functions of k_x and k_z are:

$$k_x = \Delta\, sin\varphi;\ k_z = \Delta cos\varphi \tag{5.4}$$

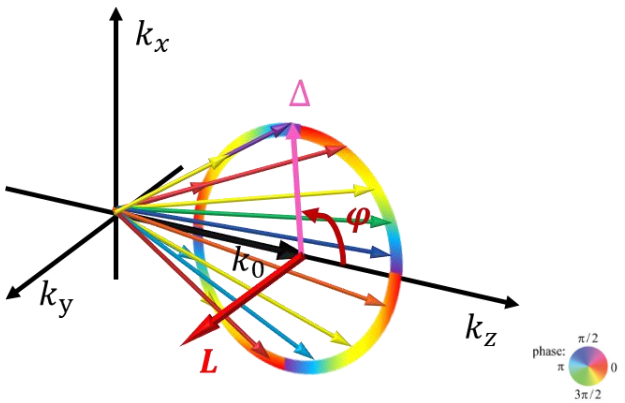

Figure 5.8 shows the angular spectrum of a STOV which is circularly symmetric and has linear polarisation states along the direction of y-axis; The colormap represents phases of the plane-wave amplitudes, i.e., $E_y \propto e^{i\ell\varphi}$, where φ is the azimuthal angle of polar coordinates in the k_x-$k_z$plane. In this figure, $\ell = 4$; k_0 is the wavenumber of the carrier term of the STOV; Δ represents the radius of the circular angular spectrum.

The dispersion relationship of this STOV in free space is:

$$k_x^2 + k_z^2 = \left(\frac{\omega}{c}\right)^2 \tag{5.5}$$

where k_x and k_z are transverse and longitudinal components of the wave vector along $\hat{x}$ and $\hat{z}$ direction, respectively. Here, ω represents the temporal frequency, and c is the speed of light in a vacuum. Geometrically, this relationship is represented by the surface of a cone, commonly known as the light cone shown in Figure 1.8 of Chapter 1. By combining the angular spectrum of the STOV shown in Figure 5.8 with the light cone defined by Eq. (5.5) shown in Figure 1.8, we can obtain a schematic diagram for the visualisation of the spectral support domain for the 2D ST wave packet on the surface of the free space light cone, as shown in Figure 5.9. The closed curve coloured in orange is the intersection of the cylinder defined by the STOV's angular spectrum and its light cone. Panel (a) shows the combination of the STOV's angular spectrum and the light cone.

Panel (b) is the spectral projection onto the (k_z, ω/c)- plane, which is a segment of a conic section. In addition, the projection of the spectrum is extracted separately for display, and it is coloured by a colormap. Panel (b) indicates that the relationship between k_z and ω/c is non-linear. This relation can be deduced by substituting the parametric functions in Eq. (5.4) into Eq. (5.5), and we have:

$$k_z = \frac{(\omega/c)^2 + (k_0)^2 - (\Delta)^2}{2k_0} \tag{5.6}$$

The non-linear relation of the k_z and ω/c indicates the dispersion of the light pulse. When the pulse's spectrum is defined, the group velocity, dispersion, and other properties are determined. Expressions of the group velocity v_g and the group velocity dispersion Γ are shown in Eq. (5.7) and (5.8):

$$v_g = \frac{d\omega}{dk} \tag{5.7}$$

$$\Gamma = \frac{d^2\omega}{d^2k} \tag{5.8}$$

The colormap represents the frequency of the corresponding component. Colours ranging from reddish-brown to purple indicate increasing values of the frequency. The dashed line represents the light-line, and the middle point of the dashed line corresponds to k_0 because this point is mapped from the centre of the angular spectrum of the STOV. Tangents of the segment of the conic section of the projection of the spectrum make an angle θ with the k_z, and it has the following formula:

$$\frac{\omega - \omega_0}{c(k_z - k_0)} = \tan\theta \tag{5.9}$$

If $\theta \in (0^\circ, 45^\circ)$, the value of the velocity is less than the velocity of light; and if $\theta \in (45^\circ, 90^\circ)$, the value of the velocity is greater than the velocity of light. Therefore, this STOV has both superluminal and subluminal light components. Additionally, because the low frequency propagates ahead of the high frequency, this STOV is a positively chirped pulse. The spectral projection onto the (k_x, ω/c)-plane shown in panel (c) is a closed curve. Panel (d) shows a top view of the schematic of the visualisation of the spectral support domain for the 2D ST wave packet on the surface of the free-space light cone.

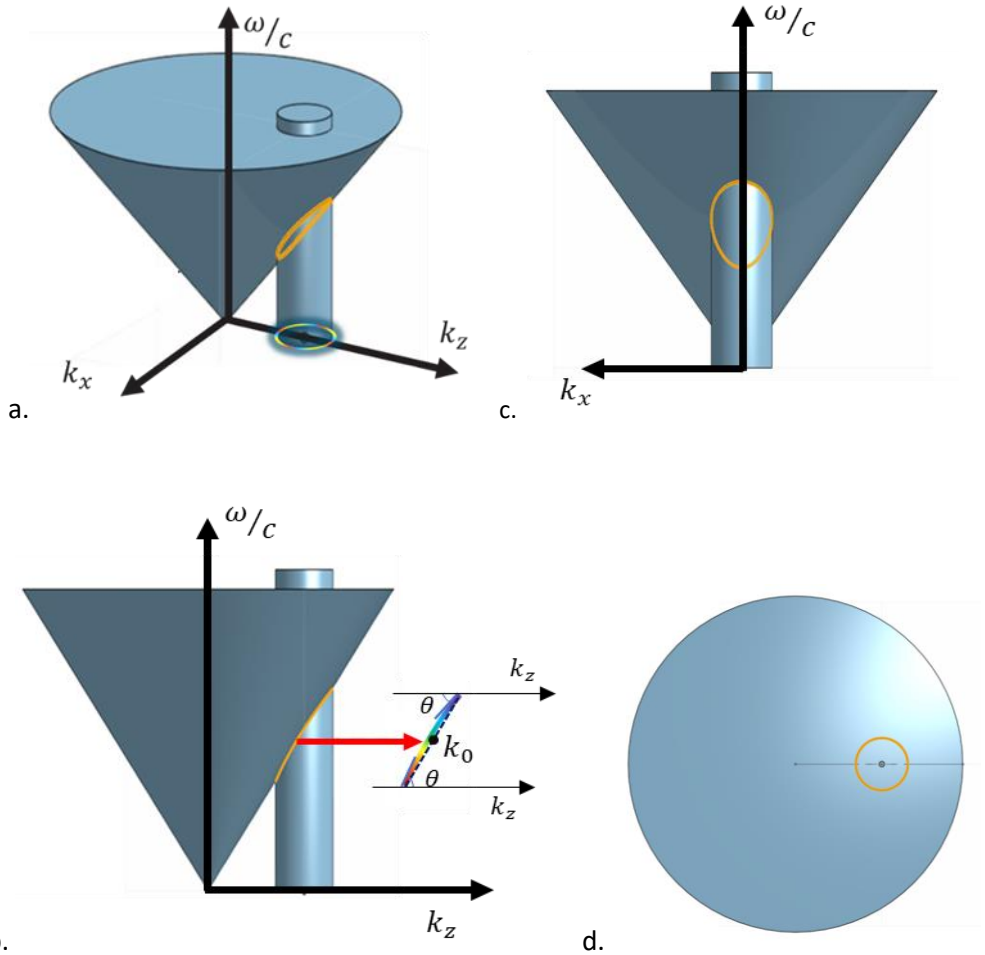

Figure 5.9 (a) A schematic diagram for the visualisation of the spectral support domain for the 2D ST wave packet on the surface of the free-space light cone. (b) The spectral projection onto the (k_z, ω/c)-plane is a segment of a conic section. The projection of the spectrum is extracted separately for display, and it is coloured by a colormap. The colormap represents the frequency of the corresponding component, and it from reddish-brown to purple indicates increasing values of the frequency. The dashed line represents the light-line, and the middle point of the dashed line corresponds to k_0 because this point is mapped from the centre of the angular spectrum of the STOV. Tangents of the segment of the conic section of the projection of the spectrum make an angle θ with the k_z. The range $\theta \in (0^\circ, 45^\circ)$ means the value of the velocity is less than the speed of light, and the range $\theta \in (45^\circ, 90^\circ)$ means the value of the velocity is greater than the speed of light. (c) The spectral projection onto the (k_x, ω/c)-plane is a closed curve. (d) It is a top view of the schematic of the visualisation of the spectral support domain for the 2D ST wave packet on the surface of the free-space light cone.

In Chapter 1 section 1.2.3, we introduced that a pulsed field can be expressed as a product of a slowly varying envelope $\Psi(x,z,t)$ and a carrier term $e^{i(k_0 z - \omega_0 t)}$, where ω_0 is a fixed temporal frequency, and $k_0 = \frac{\omega_0}{c}$ is its associated wave number. The varying envelope function of the optical field with has the angular spectrum (shown in Figure 5.10), is:

$$\Psi(x,z;t) = \iiint dk_z dk_x d\Delta\omega \tilde{\psi}(k_z,k_x;\Delta\omega) e^{ik_x x} e^{ik_z z} e^{-ik_0 z} e^{-i\Delta\omega t}, \qquad (5.10)$$

where $\Delta\omega = \omega - \omega_0$. It is easy to calculate this slowly varying envelope function in the local coordinate $((\varsigma, x; t))$, whose origin point is at the centre of the circle shown in Figure 5.10.

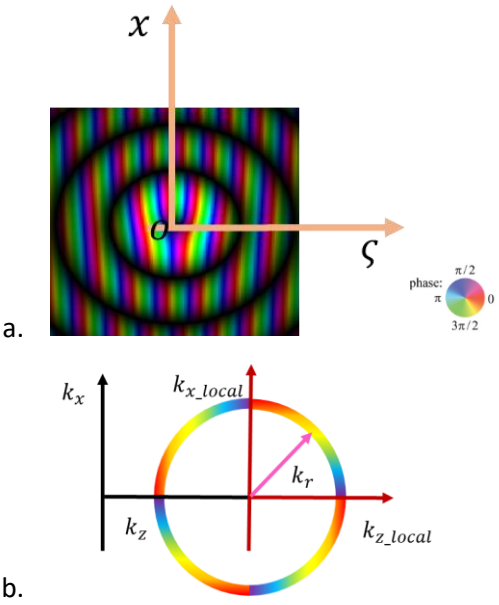

Figure 5.10 Panel (a) is the schematic diagram of the STOV carrying transverse OAM in real space. The coordinate (ς, x) is defined as the STOV's local coordinates. Panel (b) shows a schematic of the angular spectrum of STOV in local coordinate and global coordinate; The global coordinate is represented in black; the local coordinate is represented in red, and the centre of the circle is the origin of the local coordinate. The phase of the plane-wave amplitudes ($E \propto e^{i\ell\varphi}$) is depicted by the colormap, where φ is the azimuthal angle of polar coordinates in the k_x-$k_z$plane. In this figure, $\ell = 4$. k_r represents the radius of the angular spectrum.

And then, it is easy for us to find a solution in the local coordinate by means of the Bessel functions. And the Eq. (5.10) can be rewritten in the local coordinate as follows:

$$\Psi(x,\varsigma;t) = \iiint dk_{zlocal} dk_{xlocal} d\Delta\omega \tilde{\psi}(k_{zlocal},k_{xlocal};\Delta\omega) e^{ik_{xlocal}\cdot x} e^{ik_{zlocal}\cdot\varsigma} e^{-ik_0\varsigma} e^{-i\Delta\omega t} \quad (5.11)$$

The angular spectrum in Cartesian coordinate (k_z, k_x) is transferred to the polar coordinates (k_r, φ), and the corresponding spatial polar coordinate are (r, ϕ). The relations of the spatial coordinates and momentum coordinates are:

$$r = \sqrt{\varsigma^2 + x^2}, \phi = atan(\frac{x}{\varsigma})$$

$$\varsigma = rcos\phi, x = rsin\phi$$

$$k_r = \sqrt{{k_{zlocal}}^2 + {k_{xlocal}}^2}, \varphi = atan(\frac{k_{xlocal}}{k_{zlocal}})$$

$$k_{zlocal} = k_r cos\varphi, k_{xlocal} = k_r sin\varphi \tag{5.12}$$

Therefore, Eq. (5.11) can be rewritten as:

$$\Psi(r, \phi; t) = \iiint dk_r d\varphi d\Delta\omega \, k_r \, \widetilde{\psi}(k_r, \varphi; \Delta\omega) e^{ik_r r cos(\phi - \varphi)} e^{-ik_0 r cos\phi} e^{-i\Delta\omega t} \tag{5.13}$$

By means of the method of separation of variables, $\widetilde{\psi}(k_r, \varphi; \Delta\omega)$ can be expressed as:

$$\widetilde{\psi}(k_r, \varphi; \Delta\omega) = \frac{1}{2\pi} \sum_{\ell=-\infty}^{\infty} \widetilde{\psi}(k_r; \Delta\omega) \, e^{i\ell\varphi} \tag{5.14}$$

Substituting Eq. (5.14) into Eq. (5.13), we have:

$$\begin{aligned} \Psi(r, \phi; t) &= \iiint dk_r d\varphi d\Delta\omega \, k_r \frac{1}{2\pi} \sum_{\ell=-\infty}^{\infty} \widetilde{\psi}(k_r; \Delta\omega) \, e^{i\ell\varphi} e^{ik_r r cos(\phi - \varphi)} e^{-ik_0 r cos\phi} e^{-i\Delta\omega t} \\ &= \sum_{\ell=-\infty}^{\infty} e^{i\ell\phi} e^{-ik_0 r cos\phi} \iint dk_r d\Delta\omega \, k_r \, \widetilde{\psi}(k_r; \Delta\omega) J_\ell(k_r r) e^{-i\Delta\omega t} \end{aligned} \tag{5.15}$$

Panel (a) of Figure 5.11 displays the intensity (brightness) and phase distribution (colormap) of the STOV with transverse OAM $\ell = 1$. Panel (b) presents the experimental measurement result of the phase distribution for the STOV with transverse OAM $\ell = 1$ [181].

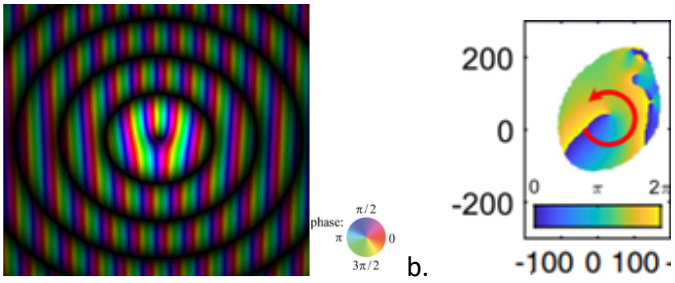

Figure 5.11 Panel (a) shows the numerical result of the intensity (brightness) and phase distribution (colormap) of the STOV with transverse OAM $\ell = 1$; Panel (b) shows the

experimental result of the phase distribution of the STOV with transverse OAM $\ell = 1$ [181].

This phase term $e^{-ik_0 r cos\phi}$ shown in Eq. (5.15) is of interest. This phase term causes the fork-like phase distribution (as shown in panel (a) of Figure 5.11), which is different from the phase distribution shown in some experimental results [51, 177]. Based on the theoretical analysis shown above, the phase term $e^{-ik_0 r cos\phi}$ should exist. I have tried to contact researchers who conducted these experimental works to show my results and ask them why there is no fork-like phase distribution displayed in their work. Many thanks to Prof. Zhan and Konstantin, who confirmed the correctness of this phase term and explained that there is currently no good method to measure that phase. Therefore, the phase distribution of the STOV shown in panel (b) of Figure 5.11 is different from the theoretical result shown in panel (a) of Figure 5.11. More specifically, in this work [51], researchers use a reference light beam with a longitudinal term the same as that of the carrier term of the STOV to interfere with the STOV, and then cameras captured the information of this coherent field as shown in Figure 5.1. This field carries the transverse information of the STOV. To obtain the dislocation phase $e^{i\ell\phi}$ in the x-z plane, researchers need to measure the transverse fields at different positions along the z direction. The measured coherent fields have vertical fringe patterns. By comparing the changes in fringe patterns of the measured field at different positions, the dislocation phase $e^{i\ell\phi}$ in the x-z plane can be obtained. However, the phase term $e^{-ik_0 r cos\phi}$, which causes the fork-like phase distribution in the x-z plane, cannot be deduced in this process.

Eq. (5.16) defines the density of the transverse OAM ($\boldsymbol{\rho}_{\mathrm{tOAM}}$) of the STOV. This transverse OAM is orthogonal to the polar coordinates (r, ϕ) in the x-z plane and is represented by a red arrow termed $'\boldsymbol{L}'$ in Figure 5.8.

$$\boldsymbol{\rho}_{\mathrm{tOAM}} = \boldsymbol{\Psi}^*_{r,\phi}\left(\frac{\partial}{\partial\phi}\right)\boldsymbol{\Psi}_{r,\phi} \tag{5.16}$$

By inserting Eq. (5.15) into Eq. (5.16), we have:

$$\boldsymbol{\rho}_{\mathrm{tOAM}} = (-rk_0 \sin\phi + \ell)\boldsymbol{\Psi}^*_{r,\phi}\boldsymbol{\Psi}_{r,\phi} \tag{5.17}$$

By integrating Eq. (5.17) we can obtain the topological charge (TC) of transverse OAM (tOAM), which is:

$$TC\ of\ tOAM = \frac{1}{2\pi\boldsymbol{\Psi}^*_{r,\phi}\boldsymbol{\Psi}_{r,\phi}}\int_0^{2\pi}\boldsymbol{\rho}_{\mathrm{tOAM}}\ d\phi = \ell \tag{5.18}$$

where ℓ is the topological charge of the transverse OAM. This result matches that of Konstantin's work for the transverse OAM of a circularly symmetric STOV. The above quantities are defined in the local coordinates. We can try to transfer Eq. (5.18) to the global reference system as shown in Figure 5.12.

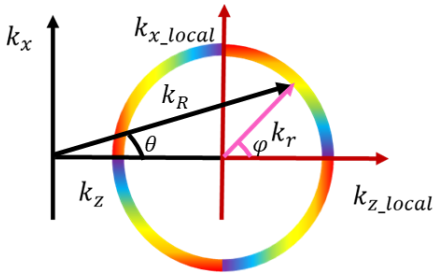

Figure 5.12 A schematic diagram of the STOV's angular spectrum represented in the polar coordinates (k_R, θ) of the global reference system.

Firstly, in momentum space, relations of components in the local coordinates (k_r, φ) and the global coordinates (k_R, θ) are shown below:

$$k_r = \sqrt{{k_{zlocal}}^2 + {k_{xlocal}}^2}, \varphi = atan\left(\frac{k_{xlocal}}{k_{zlocal}}\right),$$

$$k_{zlocal} = k_r cos\varphi, k_{xlocal} = k_r sin\varphi,$$

$$k_R = \sqrt{{k_z}^2 + {k_x}^2}, \theta = atan\left(\frac{k_x}{k_z}\right),$$

$$k_z = k_R cos\theta, k_x = k_R sin\theta = k_{xlocal},$$

$$k_r = \sqrt{(k_R cos\theta - k_0)^2 + k_R (sin\theta)^2}, \varphi = atan\left(\frac{k_R sin\theta}{(k_R cos\theta - k_0)}\right) \tag{5.19}$$

Furthermore, in real space, we have following relations of components in the local coordinates (ς, x) and the global coordinates (z, x):

$$z = \varsigma + v_g t;\ x = x, \tag{5.20}$$

where v_g is the group velocity of the STOV as shown in Eq. (5.7). The spatial components in the global reference system are:

$$z = Rcos\Theta, x = Rsin\Theta = rsin\phi, r = \sqrt{\varsigma^2 + x^2} = \sqrt{R^2 - 2zv_g t + (v_g t)^2} \tag{5.21}$$

$$\phi = atan\left(\frac{x}{\varsigma}\right) = atan\left(\frac{x}{z - v_g t}\right) = arcsin\left(\frac{R}{r} sin\theta\right). \tag{5.22}$$

The area element is:

$$dS = k_r dk_r d\varphi = \sqrt{(k_R cos\theta - k_0)^2 + k_R sin\theta^2}\, dk_r d\varphi$$

$$= \sqrt{(k_R cos\theta - k_0)^2 + k_R sin\theta^2}\; det\frac{\partial(k_r, \varphi)}{\partial(k_R, \theta)}\, dk_R d\theta \tag{5.23}$$

Substituting the above equations (Eq. (5.19) to Eq. (5.23)) into Eq. (5.15), we have:

$$\Psi(x, z; t) = \sum_{\ell=-\infty}^{\infty} \begin{matrix} e^{i\ell\cdot \arcsin\left(\frac{R}{r}sin\Theta\right)} e^{-ik_0\sqrt{R^2 - 2zv_g t + (v_g t)^2}\cos\left(\arcsin\left(\frac{R}{r}sin\Theta\right)\right)} \\ \iint det\frac{\partial(k_r,\varphi)}{\partial(k_R,\theta)}\, dk_R d\theta\, \widetilde{\psi}(k_r;\omega) J_\ell(k_r r) e^{-i\omega t} e^{i\omega_0 t} \end{matrix} \tag{5.24}$$

5.3 Exploring Toroidal Momentum in Toroidal Pulses

5.3.1 The Definition of Toroidal Momentum

"Toroidal momentum" is a quantity that has not been previously defined. It is newly introduced in this work, inspired by angular momenta. Figure 5.13 is a schematic diagram illustrating how the inspiration from angular momentum in this work led to the development of the concept defined as toroidal momentum.

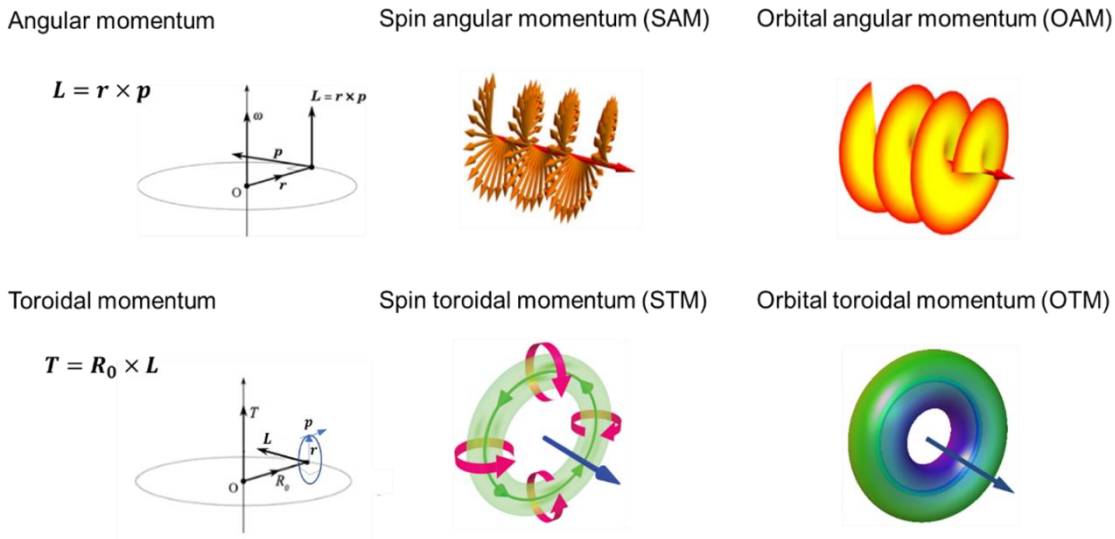

Figure 5.13 shows schematic diagrams for the angular momentum and toroidal momentum. The schematic diagrams for spin angular momentum and orbital angular momentum in this figure is based on this reference [15].

This section is studied under the assumption that the optical field has linearly polarisation states along the along one transverse direction (i.e., the y-direction). Therefore, the case termed "Spin toroidal momentum" is not studied in this chapter. To provide a clearer demonstration of the

analogy process between OAM and toroidal momentum, I created Table 5.3 to provide a more specific explanation of the process of defining toroidal momentum.

Table 5.3 Equations for angular momentum and toroidal momentum

Mechanical	**Quantum**	**Expression**
$\boldsymbol{L} = \boldsymbol{x} \times \boldsymbol{p}$	Longitudinal OAM flux density, ρ_z Quantum number (ℓ_z) of the longitudinal OAM	$\rho_z(r,\varphi) = \boldsymbol{\Psi}^*(\boldsymbol{x} \times i\boldsymbol{\nabla}_{\boldsymbol{x}})\boldsymbol{\Psi} = \boldsymbol{\Psi}^*(r,\varphi)\frac{\partial}{\partial\varphi}\boldsymbol{\Psi}(r,\varphi)$, where $\boldsymbol{x}$ represents the position operator. $\ell_z = \frac{\iint \rho_z(r,\varphi) r dr d\varphi}{\iint \boldsymbol{\Psi}^*\boldsymbol{\Psi} r dr d\varphi}$
$\boldsymbol{T} = R_0 \times \boldsymbol{L}$	Toroidal momentum flux density, $\rho_{\mathrm{tOAM}}^{\Psi}$ Quantum number (t) of the toroidal momentum	$\rho_{\mathrm{tOAM}}^{\Psi}(r,\phi) = R_0 \times \boldsymbol{\Psi}_{r,\phi}^*(\frac{\partial}{\partial\phi})\boldsymbol{\Psi}_{r,\phi}$ $t = R_0 \times \frac{\iint \rho_{\mathrm{tOAM}}^{\Psi}(r,\phi) r dr d\varphi}{\iint \boldsymbol{\Psi}_{r,\phi}^* \boldsymbol{\Psi}_{r,\phi} r dr d\varphi}$

5.3.2 Research on the Relationship Between Radius, Transverse OAM of Optical Toroidal Pulse, and Its Toroidal Momentum

In Table (5.3), the definition of toroidal momentum is

$$\boldsymbol{T} = R_0 \times \boldsymbol{L} \tag{5.25}$$

And according to Eq. (5.25), we can find that, once the value of the $\boldsymbol{L}$ (transverse OAM) is defined, the magnitude of the toroidal momentum $\boldsymbol{T}$ changes proportionally with the variation of the geometric parameter R_0 (the radius of the toroidal pulse) of the scalar toroidal pulse. Therefore, the theoretical value can be computed. Figure 5.14 shows the calculation results of theoretical value of the toroidal momentum for scalar toroidal pulses with 6 different setting value of the R_0. The parameter l_s represents the value of the transverse OAM carried by toroidal pulses.

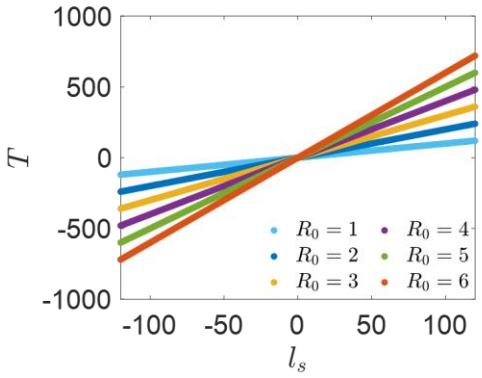

Figure 5.14 Theoretical value of toroidal momentum calculated by Eq. (5.25).

Based on equation shown in Table 5.3 and Eq. (5.3), the numerical simulation of toroidal momentum was carried out using MATLAB. The results are shown in Figure 5.15 below:

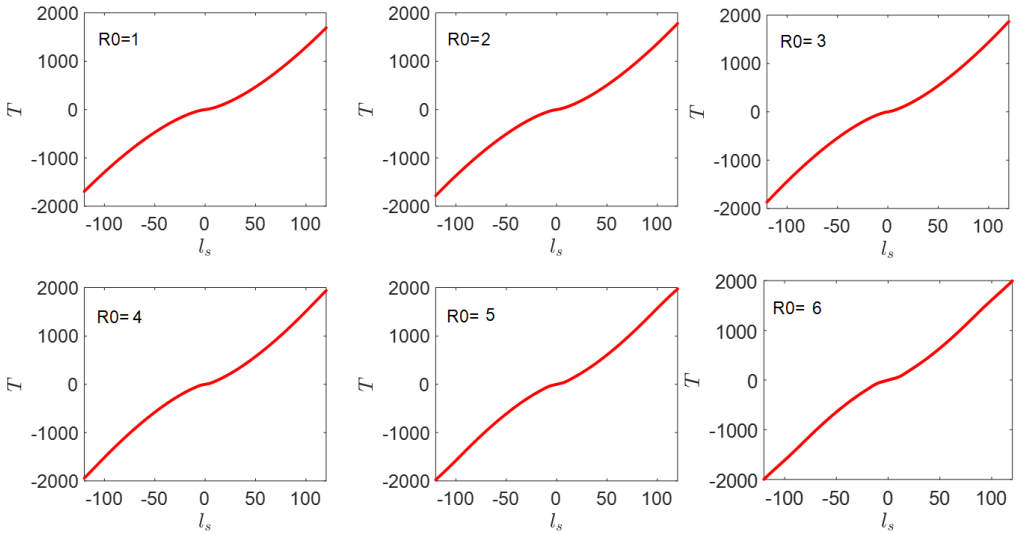

Figure 5.15 The simulation results of the value of toroidal momentum.

To better compare simulation results with theoretical values, the simulated and theoretical values of toroidal momentum for toroidal light pulses with the same radius are plotted on the same graph shown in Figure 5.16.

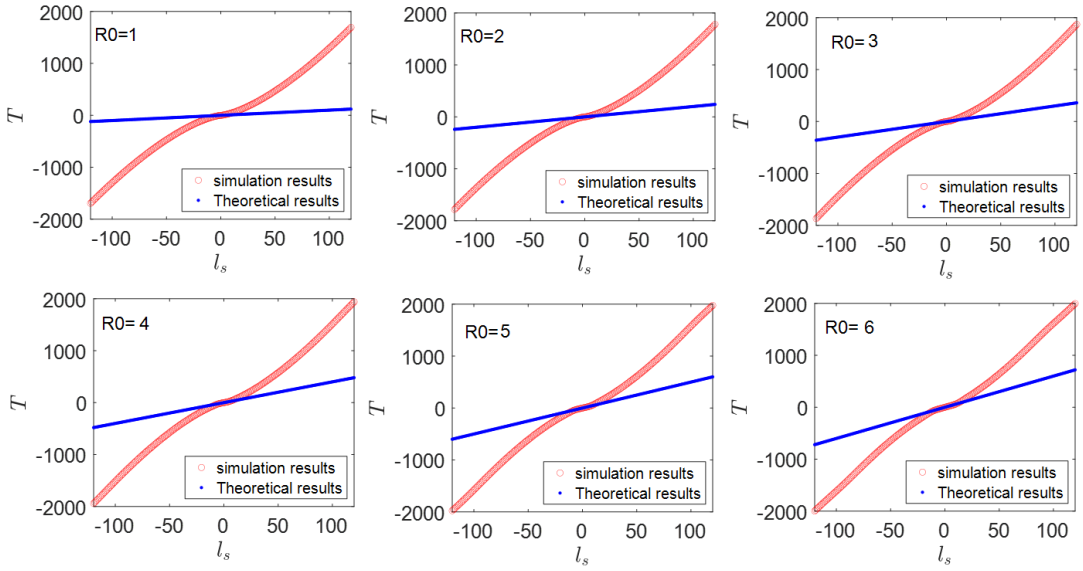

Figure 5.16 Comparison of the calculated and theoretical values of toroidal momentum with different R_0.

To further illustrate the relationship between theoretical values and simulation results under varying radii of the toroidal pulse, I also computed the case for $R_0 = 30$. The result is shown in Figure 5.17:

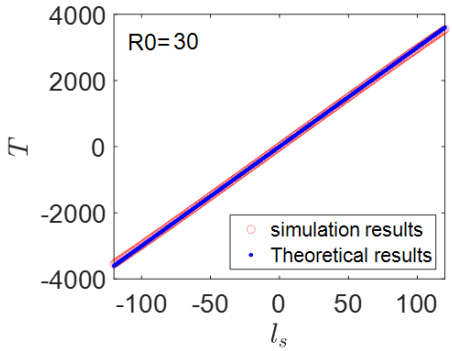

Figure 5.17 The calculated and theoretical values of the toroidal momentum for a pulse with the radius of $R_0 = 30$.

By comparing the results shown in Figure 5.16 and 5.17, we can find that the larger radii of the toroidal pulse, the better alignment of the theoretical values and simulation results. To identify the reason behind the better alignment of theoretical values with simulation results only within a specific interval centred around transverse OAM's value $l = 0$, I studied the density distribution of toroidal momentum on the x-z plane under the condition that the radii of toroidal pulses is a variable and the topological charge of the transverse OAM carried by these pulses is a constant of 1. The results are shown in Figure 5.18. "TC" is the abbreviation of "topological charge" which

represents the value of the transverse OAM. "R_0" represents the radius of the toroidal pulse.

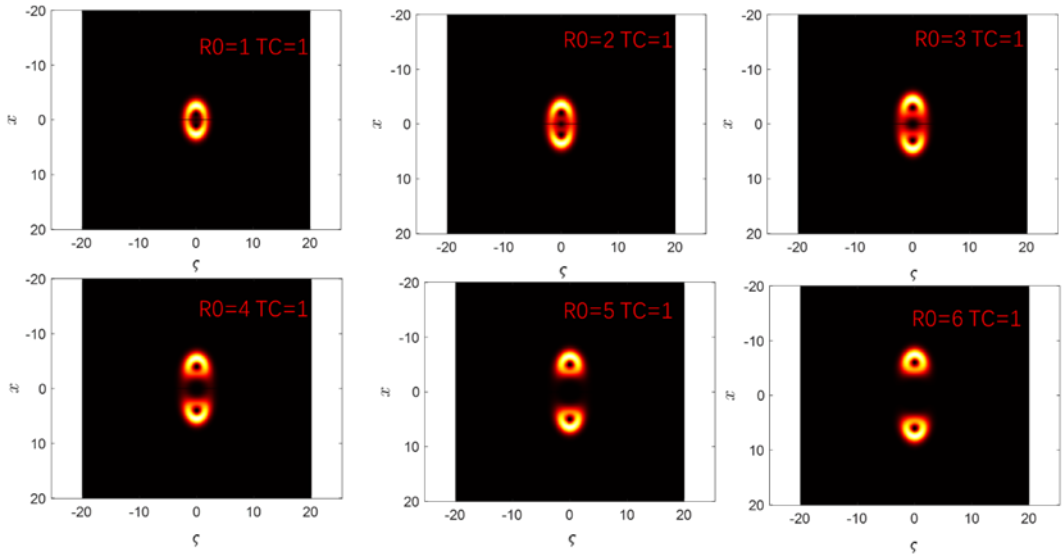

Figure 5.18 The toroidal momentum density distribution.

From the above results, we can observe that a scalar toroidal pulse with a certain radius R_0 can only carry up to a corresponding maximum transverse OAM. The maximum of the transverse OAM for several pulses with R_0 from 1 to 7 is shown in Figure 5.18. Additionally, two supplementary cases are presented in this figure: one example for an ill-defined toroidal pulse with R_0 and TC values of (1, 25) and another example for a well-defined toroidal pulse with R_0 and TC values of (10, 5). To clearly show the phase distribution of transverse OAM, in Figure 5.19, another phase term (propagation phase term $e^{-ik_0\varsigma}$) has been ignored.

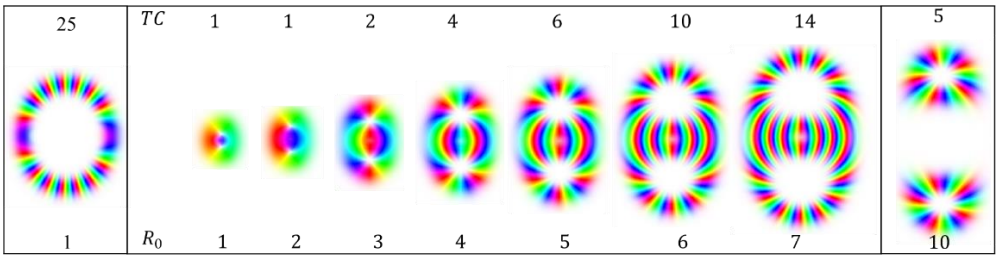

Figure 5.19 The maximum TC that can be carried by scalar toroidal pulses with different R_0; Two supplementary cases are placed first and last (one example of an ill-defined toroidal pulse, and another of a well-defined toroidal pulse).

In fact, we cannot classify the pulse shown in Figure 5.20 as a "toroidal" light pulse. This type of pulse is not stable in real space. Therefore, a light pulse with a specific R_0 cannot be considered toroidal anymore when the transverse OAM exceeds its corresponding limit. The following schematic in Figure 5.21 illustrates the deformation process of the toroidal light pulse [186]:

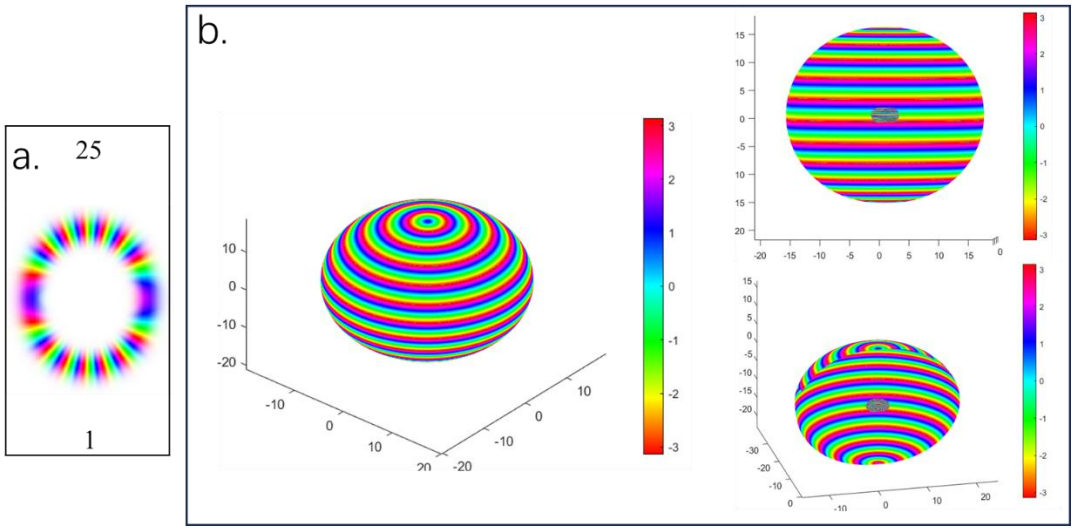

Figure 5.20 Schematic of the toroidal pulse with $TC = 25$ and $R_0 = 1$. (a). The phase distribution in the x-z plane. (b). The iso-surface coloured by phase distribution of the "toroidal" pulse in 3D space.

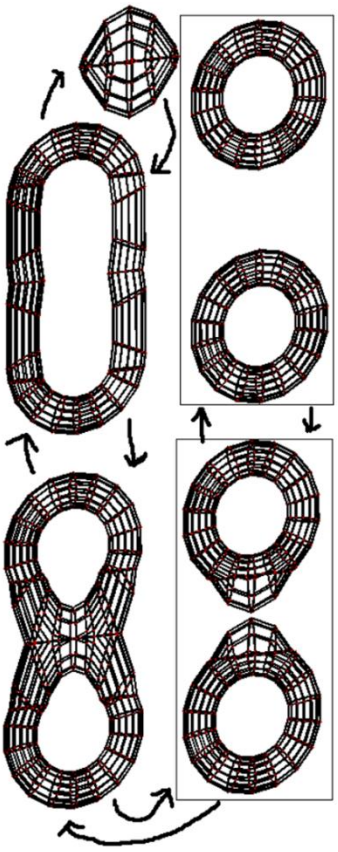

Figure 5.21 shows a schematic of the deformation process of a toroidal light pulse. This toroidal pulse has a constant value of radius (R_0) but carries a significantly large transverse OAM [186].

5.4 Conclusion

In summary, this chapter introduced two main studies, each of which provided valuable insights into optical pulses. Firstly, this chapter uses the light cone theory and momentum spectrum of STOV to explain the process of calculating its transverse OAM, and detailed envelope function of the STOV is also provided. Two controversies regarding STOV are discussed: the calculation of transverse OAM, and the phase distribution of STOV in the x-z plane. The calculation result of STOV's transverse OAM is found to be consistent with previous findings [179], with a detailed calculation process provided. Additionally, discrepancies between numerical calculations and experimental observations of the phase distribution in the x-z plane of STOV are discussed. Secondly, inspired by angular momentum, we introduce a new quantity which is temporarily referred to as "toroidal momentum". Exploring these light pulses not only enhances our understanding of the physical world but also opens up exciting new research directions in optical sensing.

Chapter 6 Conclusion and Outlook

This thesis investigates two types of optical vortices: the monochromatic vortex beam under paraxial approximation and spatiotemporal vortices, along with their related research in engineering.

Chapter 1 presents fundamental concepts and the structure of the thesis.

Chapter 2 introduces the concept of the total angular momentum-conserving Poincaré sphere (TAM-C PS). By linking poles of different TAM-C PSs, two categories of TAM-C PS braid clusters are created. These clusters provide a framework for representing and characterising beams, guiding the generation of targeted VVB. TAM-C PS offers a balanced compromise between generality and application, encompassing various Poincaré spheres. This approach intuitively represents relationships between different spheres, aids in describing optical field evolution, and calculates geometric phases, contributing valuable insights to optics. Two potential directions for further exploration include: The evolution of the light field state under angular momentum conservation is an intriguing topic worth further research. The meta-surface J-plate is an optical state converter that couples arbitrary spin and optical angular momentum states into a compact plane [187], with trade-offs between arbitrary transformations of angular momentum and conversion efficiency. The work in this chapter sheds light on the energy-angular momentum relationship during optical field transformations. Building on TAM-C PS, two braid clusters are introduced, combining group theory with Poincaré spheres to describe physical phenomena. Exploring braid clusters and the relationship between group theory and optical angular momentum is a field worthy of in-depth research.

Chapter 3 presents a method for analysing the value of OAM in scalar vortex beams and TAM in VVBs. These approaches help our collaborators analyse vortex beams from meta-surface integrated micro-rings during design and simulation, avoiding early physical fabrication and saving time, effort, and money. Additionally, this work can aid in optical sensing, such as detecting signals from noise and deducing object information based on OAM mode changes. However, the current method is limited to analysing longitudinal OAM modes of monochromatic beams under paraxial approximation (more precisely, LG beams). Future research can focus on characterising OAM modes of non-paraxial vortex beams, potentially involving decomposition into Bessel beams and angular spectrum analysis. If considering the vector nature of the unknown vortex beam, the angular momenta cannot be directly divided into spin and OAM parts, requiring further research to develop a general method for analysing angular momenta in such beams.

Chapter 4 explores using vector beams and VVB as detection signals for LiDAR sensors to measure the orientation of reflecting surfaces. Using the Fresnel equation, coordinate transformations, and angular spectrum analysis, a reflection computation model for vector beams and VVB is developed. Relations between properties of reflected vector beams and VVB and incident angles are examined, including reflectance and intensity centroid shifts. Results show that measuring reflectance and centroid shifts can deduce the incident angle, with hybrid polarisation vector beams ($|\Psi^{R_{4th}}\rangle$) being optimal. This study offers a new sensing scheme for LiDAR research. Due to insufficient equipment and time constraints, experimental work on this part has not yet been carried out, but it can be pursued in the future. Additionally, with the aid of this experimental system, we can further research a LiDAR based on the detection principle of the rotational Doppler effect. This LiDAR can detect the angular momentum of the object being observed. Detecting this physical quantity can further enrich the capabilities of LiDAR in assessing the motion and orientation of target objects. Inspired by the meta-surface integrated micro-ring laser, we can explore its application in LiDAR systems in the future. Such a LiDAR system would have advantages such as small size, low cost, portability, and the ability to produce a variety of laser beam types. Besides, future research can focus on improving signal-to-noise ratio, processing reflected signals to extract effective information, examining a greater variety type of VVB as detection signals, and investigating the relationship between incident angle and other properties of reflected fields, such as polarisation distribution and singularity points.

Chapter 5 explains the process of calculating transverse OAM of STOV using light cone theory and the angular spectrum, providing a detailed envelope function and phase distribution in the z-x plane, resolving two controversies in the field. The results align with theoretical and experimental findings. Additionally, it introduces the concept of “toroidal momentum” in optical toroidal pulses. These insights enhance our understanding and application of optical pulses in optical sensing. Conclusions about the transverse OAM presented in this article are consistent with those of a previous researcher. However, the current discussion on this issue has not yet been finalized. So, giving a conclusion that can convince everyone is a worthwhile research direction. The theoretical system of spatiotemporal optical vortex as well as the transverse angular momentum has not been fully established yet. Therefore, this will also become a worthwhile research direction. Besides, the spatiotemporal optical vortex being researched is scalar optical vortex. The vector spatiotemporal optical vortex has not been well researched yet. In vector spatiotemporal optical vortex, we can study the interaction of transverse spin and transverse OAM. As to the optical toroidal pulse research, in the future, we can do relevant experiments for verification of the toroidal momentum. Currently, research on toroidal pulses is in its early stages, and studies on their propagation characteristics and interactions with matter have not yet been published. In

the future, we can investigate the refraction and reflection of toroidal pulses at different interfaces or explore the physical processes that occur when they interact with various material interfaces. Additionally, due to the connection between toroidal pulse and Hopf fibre bundles, it is bound to be a hot physics frontier in the future. The angular momentum characteristics, spatiotemporal characteristics, propagation characteristics, and so on of toroidal pulse are very worthy of attention and research directions.

Bibliography

1 D'Ambrosio, V., Carvacho, G., Graffitti, F., Vitelli, C., Piccirillo, B., Marrucci, L., & Sciarrino, F. (2016). Entangled vector vortex beams. *Physical Review A*, *94*(3), 030304.

2 Al-Amri, M. D., Andrews, D. L., & Babiker, M. (Eds.). (2021). *Structured Light for Optical Communication*. Elsevier.

3 Barnett, S. M. (2001). Optical angular-momentum flux. Journal of Optics B: Quantum and Semiclassical Optics, 4(2), S7.

4 Yue, F., Wen, D., Xin, J., Gerardot, B. D., Li, J., & Chen, X. (2016). Vector vortex beam generation with a single plasmonic metasurface. *ACS photonics*, *3*(9), 1558-1563.

5 Fu, S., Gao, C. (2023). Vector Beams and Vectorial Vortex Beams. In: Optical Vortex Beams. Advances in Optics and Optoelectronics. Springer, Singapore. https://doi.org/10.1007/978-981-99-1810-2_7

6 Li, Z., Kim, M. H., Wang, C., Han, Z., Shrestha, S., Overvig, A. C., ... & Yu, N. (2017). Controlling propagation and coupling of waveguide modes using phase-gradient metasurfaces. Nature nanotechnology, 12(7), 675-683.

7 Pi, H. (2022). Microring resonators for vortex beam emission and their all-optical wavelength tuning.

8 He, H., Friese, M. E. J., Heckenberg, N. R., & Rubinsztein-Dunlop, H. (1995). Direct observation of transfer of angular momentum to absorptive particles from a laser beam with a phase singularity. Physical review letters, 75(5), 826.

9 Padgett, M., & Bowman, R. (2011). Tweezers with a twist. Nature photonics, 5(6), 343-348.

10 Barreiro, J. T., Wei, T. C., & Kwiat, P. G. (2008). Beating the channel capacity limit for linear photonic superdense coding. Nature physics, 4(4), 282-286.

11 Xie, G., Song, H., Zhao, Z., Milione, G., Ren, Y., Liu, C., ... & Willner, A. E. (2017). Using a complex optical orbital-angular-momentum spectrum to measure object parameters. Optics letters, 42(21), 4482-4485.

12 Xie, Z., Lei, T., Si, G., Du, L., Lin, J., Min, C., & Yuan, X. (2017). On-chip spin-controlled orbital angular momentum directional coupling. Journal of Physics D: Applied Physics, 51(1), 014002.

13 Jhajj, N., Larkin, I., Rosenthal, E. W., Zahedpour, S., Wahlstrand, J. K., & Milchberg, H. M. (2016). Spatiotemporal optical vortices. Physical Review X, 6(3), 031037.

14 Chen, W., Liu, Y., & Lu, Y. Q. (2023). Spatiotemporal Optical Vortices: Toward Tailoring Orbital Angular Momentum of Light in Full Space-Time. *ACS Photonics*.

15 Shen, Y., Wang, X., Xie, Z., Min, C., Fu, X., Liu, Q., ... & Yuan, X. (2019). Optical vortices 30 years on: OAM manipulation from topological charge to multiple singularities. Light: Science & Applications, 8(1), 90.

16 Poynting, J. H. (1909). The wave motion of a revolving shaft, and a suggestion as to the angular momentum in a beam of circularly polarised light. Proceedings of the Royal Society of London. Series A, Containing Papers of a Mathematical and Physical Character, 82(557), 560-567.

17 Beth, R. A. (1936). Mechanical detection and measurement of the angular momentum of light. Physical Review, 50(2), 115.

18 Allen, L., Beijersbergen, M. W., Spreeuw, R. J. C., & Woerdman, J. P. (1992). Orbital angular momentum of light and the transformation of Laguerre-Gaussian laser modes. Physical review A, 45(11), 8185.

19 He, H., Friese, M. E. J., Heckenberg, N. R., & Rubinsztein-Dunlop, H. (1995). Direct observation of transfer of angular momentum to absorptive particles from a laser beam with a phase singularity. Physical review letters, 75(5), 826.

20 Molina-Terriza, G., Torres, J. P., & Torner, L. (2007). Twisted photons. Nature physics, 3(5), 305-310.

21 File: Sam v1.png. (2022, August 3). Wikimedia Commons. Retrieved 03:33, June 21, 2024 from https://commons.wikimedia.org/w/index.php?title=File:Sam_v1.png&oldid=680179565.

22 Bliokh, K. Y., & Nori, F. (2015). Transverse and longitudinal angular momenta of light. Physics Reports, 592, 1-38.

23 Wikipedia, “Orbital angular momentum of light” 2019. [Online]. Available: https://en.wikipedia.org/wiki/Orbital_angular_momentum_of_light.

24 Garcés-Chávez, V., McGloin, D., Padgett, M. J., Dultz, W., Schmitzer, H., & Dholakia, K. (2003). Observation of the transfer of the local angular momentum density of a multiringed light beam to an optically trapped particle. Physical review letters, 91(9), 093602-093602.

25 Zhao, Y., Edgar, J. S., Jeffries, G. D., McGloin, D., & Chiu, D. T. (2007). Spin-to-orbital angular momentum conversion in a strongly focused optical beam. Physical review letters, 99(7), 073901.

26 Landau, L. D., Lifshi͡ts, E. M., & Lifshi͡ts, E. M. (1960). Mechanics (Vol. 1). CUP Archive.

27 M. Abraham, Prinzipien der Dynamik des Elektrons, Ann. Phys. 10, 105 (1903),

28 K. F. Riley, M. P. Hobson and S. J. Bence Mathematical Methods for Physics and Engineering. Cambridge University Press 2002

29 Cohen-Tannoudji, C., Dupont-Roc, J., & Grynberg, G. (1997). Photons and atoms-introduction to quantum electrodynamics (p. 486).

30 Lax, M., Louisell, W. H., & McKnight, W. B. (1975). From Maxwell to paraxial wave optics. Physical Review A, 11(4), 1365.

31 Haus, H. A. (1984). Waves and fields in optoelectronics. (No Title).

32 Andrews, D. L., & Babiker, M. (Eds.). (2012). The angular momentum of light. Cambridge University Press.

33 Ulanowski, Z. (2001). Optical tweezers-principles and applications. In Proc. Roy. Microsc. Soc.

34 Rosales-Guzmán, C., Ndagano, B., & Forbes, A. (2018). A review of complex vector light fields and their applications. Journal of Optics, 20(12), 123001.

35 D. G. Hall. (1996). “Vector-beam solutions of Maxwell’s wave equation,” Opt. Lett. 21, 9–11

36 Galvez, E. J., Khadka, S., Schubert, W. H., & Nomoto, S. (2012). Poincaré-beam patterns produced by nonseparable superpositions of Laguerre–Gauss and polarization modes of light. Applied optics, 51(15), 2925-2934.

37 R. Paschotta. (2008). Field Guide to Laser Pulse Generation, SPIE Press, Bellingham, WA.

38 lecture10.pdf (brown.edu)

39 Shen, Y., Papasimakis, N. & Zheludev, N.I. (2024). Nondiffracting supertoroidal pulses and optical “Kármán vortex streets”. Nat Commun 15, 4863.

40 Yessenov, M., Free, J., Chen, Z., Johnson, E. G., Lavery, M. P., Alonso, M. A., & Abouraddy, A. F. (2022). Space-time wave packets localized in all dimensions. Nature Communications, 13(1), 4573.

41 Bliokh, K. Y., & Nori, F. (2012). Spatiotemporal vortex beams and angular momentum. Physical Review A, 86(3), 033824.

42 Bliokh, K. Y., & Nori, F. (2012). Relativistic hall effect. Physical Review Letters, 108(12), 120403.

43 Yang, Y., Ren, Y. X., Chen, M., Arita, Y., & Rosales-Guzmán, C. (2021). Optical trapping with structured light: a review. Advanced Photonics, 3(3), 034001-034001.

44 Goffin, A., Larkin, I., Tartaro, A., Schweinsberg, A., Valenzuela, A., Rosenthal, E. W., & Milchberg, H. M. (2023). Optical guiding in 50-meter-scale air waveguides. Physical Review X, 13(1), 011006.

45 Jhajj, N., Larkin, I., Rosenthal, E. W., Zahedpour, S., Wahlstrand, J. K., & Milchberg, H. M. (2016). Spatiotemporal optical vortices. Physical Review X, 6(3), 031037.

46 Gui, G., Brooks, N. J., Kapteyn, H. C., Murnane, M. M., & Liao, C. T. (2021). Second-harmonic generation and the conservation of spatiotemporal orbital angular momentum of light. Nature Photonics, 15(8), 608-613.

47 Gui, G., Brooks, N. J., Wang, B., Kapteyn, H. C., Murnane, M. M., & Liao, C. T. (2022). Single-frame characterization of ultrafast pulses with spatiotemporal orbital angular momentum. ACS photonics, 9(8), 2802-2808.

48 Hancock, S. W., Zahedpour, S., Goffin, A., & Milchberg, H. M. (2019). Free-space propagation of spatiotemporal optical vortices. Optica, 6(12), 1547-1553.

49 Wang, H., Guo, C., Jin, W., Song, A. Y., & Fan, S. (2021). Engineering arbitrarily oriented spatiotemporal optical vortices using transmission nodal lines. Optica, 8(7), 966-971.

50 Zang, Y., Mirando, A., & Chong, A. (2022). Spatiotemporal optical vortices with arbitrary orbital angular momentum orientation by astigmatic mode converters. Nanophotonics, 11(4), 745-752.

51 Chong, A., Wan, C., Chen, J., & Zhan, Q. (2020). Generation of spatiotemporal optical vortices with controllable transverse orbital angular momentum. Nature Photonics, 14(6), 350-354.

52 R. Paschotta, article on "Optical Power Meters" in the RP Photonics Encyclopedia, retrieved 2024-06-23, https://doi.org/10.61835/5sh

53 Bernd, D., Henriette, M., & Gross, H. (Eds.). (2012). Handbook of optical systems, volume 5: Metrology of optical components and systems. John Wiley & Sons.

54 Quan, C., Tay, C. J., Shang, H. M., & Bryanston-Cross, P. J. (1995). Contour measurement by fibre optic fringe projection and Fourier transform analysis. Optics Communications, 118(5-6), 479-483.

55 Sweta Sinha, Christine Jeyaseelan, Gunjan Singh, Tanya Munjal, Debarati Paul, Chapter 8 - Spectroscopy—Principle, types, and applications, Basic Biotechniques for Bioprocess and Bioentrepreneurship, Academic Press, 2023, Pages 145-164

56 Jung, H., Sim, S., & Lee, H. (2023). Biometric authentication security enhancement under quantum dot light-emitting diode display via fingerprint imaging and temperature sensing. Scientific Reports, 13(1), 794.

57 Gupta, H., Arumuru, V., & Jha, R. (2020). Industrial fluid flow measurement using optical fiber sensors: A review. IEEE Sensors Journal, 21(6), 7130-7144.

58 Wissmeyer, G., Pleitez, M. A., Rosenthal, A., & Ntziachristos, V. (2018). Looking at sound: optoacoustics with all-optical ultrasound detection. Light: Science & Applications, 7(1), 53.

59 Cho, H., Seo, Y. W., Kumar, B. V., & Rajkumar, R. R. (2014, May). A multi-sensor fusion system for moving object detection and tracking in urban driving environments. In 2014 IEEE International Conference on Robotics and Automation (ICRA) (pp. 1836-1843). IEEE.

60 Chen, Z., Daly, U., Boldin, A., Alsaigh, R., & Lavery, M. P. (2022, December). Sensing and Communications in Turbulent Environments with Structured Light. In Applications of Lasers for Sensing and Free Space Communications (pp. LsW5C-3). Optica Publishing Group.

61 Halina Rubinsztein-Dunlop et al (2017), J. Opt. 19, 013001

62 Lum, D. J. (2020). Ultrafast time-of-flight 3D LiDAR. Nature Photonics, 14(1), 2-4.

63 Tang, L., Hu, Z., Teng, D., & Liu, L. (2023). Integrated high precision time-of-flight depth sensing and optical communication based on Hamiltonian coding. Optics Communications, 539, 129484.

64 Lange, R.; Seitz, P. Solid-state time-of-flight range camera. IEEE J. Quantum Electron. 2001, 37, 390–397.

65 Hansard, M.; Lee, S.; Choi, O.; Horaud, R.P. Time-of-Flight Cameras: Principles, Methods and Applications; Springer Science & Business Media: Berlin, 2012.

66 Wang, W. M., Grattan, K. T. V., Palmer, A. W., & Boyle, W. J. O. (1994). Self-mixing interference inside a single-mode diode laser for optical sensing applications. Journal of lightwave technology, 12(9), 1577-1587.

67 Taimre, T., Nikolić, M., Bertling, K., Lim, Y. L., Bosch, T., & Rakić, A. D. (2015). Laser feedback interferometry: a tutorial on the self-mixing effect for coherent sensing. Advances in Optics and Photonics, 7(3), 570-631.

68 Hao, H., Guo, D., Wang, M., Xia, W., & Ni, X. (2014). Micro-displace sensor based on self-mixing interference of the fiber laser with phase modulation. Photonic sensors, 4, 379-384.

69 Kolb, A.; Barth, E.; Koch, R.; Larsen, R. Time-of-flight cameras in computer graphics. Comput. Gr. Forum, 2010, 29, 141–159.

70 Sarbolandi, H.; Plack, M.; Kolb, A. Pulse Based Time-of-Flight Range Sensing, Sensors, 2018, 18, 1679.

71 Lange, R.; Seitz, P. Solid-state time-of-flight range camera. IEEE J. Quantum Electron. 2001, 37, 390–397.

72 Hansard, M.; Lee, S.; Choi, O.; Horaud, R.P. Time-of-Flight Cameras: Principles, Methods and Applications; Springer Science & Business Media: Berlin, 2012.

73 Uttam, D.; Culshaw, B. Precision time domain reflectometry in optical fiber systems using a frequency modulated continuous wave ranging technique, J. Lightw. Technol, 1985, 3, 971–977.

74 Wojtkiewicz, A.; Misiurewicz, J.; Nalecz, M.; Jedrzejewski, K.; Kulpa, K. Two-dimensional signal processing in FMCW radars. In Proceeding of the XXth National Conference on Circuit Theory and Electronic Networks; University of Mining and Metallurgy: Kolobrzeg, Poland, 1997; pp. 475–480.

75 Yoshida, S. (2023). Fundamentals of Optical Waves and Lasers. Springer; pp. 35-66.

76 Bliokh, K. Y., Rodríguez-Fortuño, F. J., Nori, F., & Zayats, A. V. (2015). Spin–orbit interactions of light. Nature Photonics, 9(12), 796-808.

77 Liu, S., Guo, Z., Li, P., Wei, B., & Zhao, J. (2020). Tightly autofocusing beams: an effective enhancement of longitudinally polarized fields. Optics Letters, 45(2), 575-578.

78. Kimura, W. D., Kim, G. H., Romea, R. D., Steinhauer, L. C., Pogorelsky, I. V., Kusche, K. P., ... & Liu, Y. (1995). Laser acceleration of relativistic electrons using the inverse Cherenkov effect. Physical review letters, 74(4), 546.

79. Fang, L., Wan, Z., Forbes, A., & Wang, J. (2021). Vectorial doppler metrology. Nature Communications, 12(1), 4186.

80. Bouhelier, A., Beversluis, M., Hartschuh, A., & Novotny, L. (2003). Near-field second-harmonic generation induced by local field enhancement. Physical review letters, 90(1), 013903.

81. Töppel, F., Aiello, A., Marquardt, C., Giacobino, E., & Leuchs, G. (2014). Classical entanglement in polarization metrology. New Journal of Physics, 16(7), 073019.

82. Rubinsztein-Dunlop, H., Forbes, A., Berry, M. V., Dennis, M. R., Andrews, D. L., Mansuripur, M., ... & Weiner, A. M. (2016). Roadmap on structured light. Journal of Optics, 19(1), 013001.

83. Ritsch-Marte, M. (2017). Orbital angular momentum light in microscopy. Philosophical Transactions of the Royal Society A: Mathematical, Physical and Engineering Sciences, 375(2087), 20150437.

84. Jesacher, A., Fürhapter, S., Bernet, S., & Ritsch-Marte, M. (2004). Size selective trapping with optical “cogwheel” tweezers. Optics express, 12(17), 4129-4135.

85. Yang, Y., Ren, Y. X., Chen, M., Arita, Y., & Rosales-Guzmán, C. (2021). Optical trapping with structured light: a review. Advanced Photonics, 3(3), 034001-034001.

86. Goyal, S. K., Roux, F. S., Forbes, A., & Konrad, T. (2013). Implementing quantum walks using orbital angular momentum of classical light. Physical review letters, 110(26), 263602.

87 File: Poincare-sphere arrows. svg. (2020, November 20). Wikimedia Commons. Retrieved 03:53, January 29, 2024 from https://commons.wikimedia.org/w/index.php?title=File:Poincare-sphere_arrows.svg&oldid=513693184.

88. Poincaré, H. (1889). Théorie mathématique de la lumière II.: Nouvelles études sur la diffraction.--Théorie de la dispersion de Helmholtz. Leçons professées pendant le premier semestre 1891-1892 (Vol. 1). G. Carré.

89 Malykin, G. B. (1997). Use of the poincare sphere in polarization optics and classical and quantum mechanics. review. Radiophysics and quantum electronics, 40(3), 175-195.

90. Milione, G., Sztul, H. I., Nolan, D. A., & Alfano, R. R. (2011). Higher-order Poincaré sphere, Stokes parameters, and the angular momentum of light. Physical review letters, 107(5), 053601.

91. Yi, X., Liu, Y., Ling, X., Zhou, X., Ke, Y., Luo, H., ... & Fan, D. (2015). Hybrid-order Poincaré sphere. Physical Review A, 91(2), 023801.

92 Wild, W. J., & Giles, C. L. (1982). Goos-Hänchen shifts from absorbing media. Physical Review A, 25(4), 2099.

93. Allen, L., Padgett, M. J., & Babiker, M. (1999). IV The orbital angular momentum of light. In Progress in optics (Vol. 39, pp. 291-372). Elsevier.

94 Barnett, S.M. and Allen, L. Orbital angular momentum and nonparaxial light beams. Optics communications 1994, 110(5-6), pp.670-678.

95 Zhao, Y., Edgar, J. S., Jeffries, G. D., McGloin, D., & Chiu, D. T. (2007). Spin-to-orbital angular momentum conversion in a strongly focused optical beam. Physical review letters, 99(7), 073901.

96 Yao, A. M., & Padgett, M. J. (2011). Orbital angular momentum: origins, behavior and applications. Advances in optics and photonics, 3(2), 161-204.

97. Shao, Z., Zhu, J., Chen, Y., Zhang, Y., & Yu, S. (2018). Spin-orbit interaction of light induced by transverse spin angular momentum engineering. Nature communications, 9(1), 926.

98. Dirac PA. The principles of quantum mechanics. Oxford university press; 1981.

99 Born, M., & Wolf, E. Principles of optics: electromagnetic theory of propagation, interference and diffraction of light. Elsevier, 2013.

100. Landau, L. D. (Ed.). (2013). The classical theory of fields (Vol. 2). Elsevier.

101. Berry, M. V. (1984). Quantal phase factors accompanying adiabatic changes. Proceedings of the Royal Society of London. A. Mathematical and Physical Sciences, 392(1802), 45-57.

102 Berry, M. V. (1987). The adiabatic phase and Pancharatnam's phase for polarized light. Journal of Modern Optics, 34(11), 1401-1407.

103 Mair, A., Vaziri, A., Weihs, G., & Zeilinger, A. (2001). Entanglement of the orbital angular momentum states of photons. *Nature*, *412*(6844), 313-316.

104 Genevet, P., Lin, J., Kats, M. A., & Capasso, F. (2012). Holographic detection of the orbital angular momentum of light with plasmonic photodiodes. *Nature communications*, *3*(1), 1278.

105 Khonina, S. N., Kotlyar, V. V., Skidanov, R. V., Soifer, V. A., Laakkonen, P., & Turunen, J. (2000). Gauss–Laguerre modes with different indices in prescribed diffraction orders of a diffractive phase element. *Optics communications*, *175*(4-6), 301-308.

106 Padgett, M., Arlt, J., Simpson, N., & Allen, L. (1996). An experiment to observe the intensity and phase structure of Laguerre–Gaussian laser modes. *American Journal of Physics*, *64*(1), 77-82.

107 Fu, S., Zhai, Y., Zhang, J., Liu, X., Song, R., Zhou, H., & Gao, C. (2020). Universal orbital angular momentum spectrum analyzer for beams. *PhotoniX*, *1*, 1-12.

108 Berkhout, G. C., & Beijersbergen, M. W. (2008). Method for probing the orbital angular momentum of optical vortices in electromagnetic waves from astronomical objects. *Physical review letters*, *101*(10), 100801.

109 Lavery, M. P., Barnett, S. M., Speirits, F. C., & Padgett, M. J. (2014). Observation of the rotational Doppler shift of a white-light, orbital-angular-momentum-carrying beam backscattered from a rotating body. *Optica*, *1*(1), 1-4.

110 Courtial, J., Robertson, D. A., Dholakia, K., Allen, L., & Padgett, M. J. (1998). Rotational frequency shift of a light beam. *Physical review letters*, *81*(22), 4828.

111 Molina-Terriza, G., Torres, J. P., & Torner, L. (2001). Management of the angular momentum of light: preparation of photons in multidimensional vector states of angular momentum. *Physical review letters*, *88*(1), 013601.

112 Leach, J., Padgett, M. J., Barnett, S. M., Franke-Arnold, S., & Courtial, J. (2002). Measuring the orbital angular momentum of a single photon. *Physical review letters*, *88*(25), 257901.

113 Berkhout, G. C., Lavery, M. P., Courtial, J., Beijersbergen, M. W., & Padgett, M. J. (2010). Efficient sorting of orbital angular momentum states of light. *Physical review letters*, *105*(15), 153601.

114 Lavery, M. P., Robertson, D. J., Berkhout, G. C., Love, G. D., Padgett, M. J., & Courtial, J. (2012). Refractive elements for the measurement of the orbital angular momentum of a single photon. *Optics express*, *20*(3), 2110-2115.

115 Ruffato, G., Capaldo, P., Massari, M., Mafakheri, E., & Romanato, F. (2019). Total angular momentum sorting in the telecom infrared with silicon Pancharatnam-Berry transformation optics. *Optics express*, *27*(11), 15750-15764.

116 Wei, S., Earl, S. K., Lin, J., Kou, S. S., & Yuan, X. C. (2020). Active sorting of orbital angular momentum states of light with a cascaded tunable resonator. *Light: Science & Applications*, *9*(1), 10.

117 Yao, E., Franke-Arnold, S., Courtial, J., Barnett, S., & Padgett, M. (2006). Fourier relationship between angular position and optical orbital angular momentum. *Optics Express*, *14*(20), 9071-9076.

118 O'neil, A. T., MacVicar, I., Allen, L., & Padgett, M. J. (2002). Intrinsic and extrinsic nature of the orbital angular momentum of a light beam. *Physical review letters*, *88*(5), 053601.

119 Vallone, G. (2017). Role of beam waist in Laguerre–Gauss expansion of vortex beams. *Optics letters*, *42*(6), 1097-1100.

120 D'Errico, A., D'Amelio, R., Piccirillo, B., Cardano, F., & Marrucci, L. (2017). Measuring the complex orbital angular momentum spectrum and spatial mode decomposition of structured light beams. *Optica*, *4*(11), 1350-1357.

121 Xiao, Y., Tang, X., Wan, C., Qin, Y., Peng, H., Hu, C., & Qin, B. (2019). Laguerre-Gaussian mode expansion for arbitrary optical fields using a subspace projection method. *Optics letters*, *44*(7), 1615-1618.

122 Ma, J., Wei, D., Wang, L., Zhang, Y., & Xiao, M. (2021). High-quality reconstruction of an optical image by an efficient Laguerre-Gaussian mode decomposition method. *Osa Continuum*, *4*(5), 1396-1403.

123 Zhu, J., Cai, X., Chen, Y., & Yu, S. (2013). Theoretical model for angular grating-based integrated optical vortex beam emitters. Optics letters, 38(8), 1343-1345.

124 Li, Z., Kim, M. H., Wang, C., Han, Z., Shrestha, S., Overvig, A. C., ... & Yu, N. (2017). Controlling propagation and coupling of waveguide modes using phase-gradient metasurfaces. *Nature nanotechnology*, *12*(7), 675-683.

125 Guo, X., Ding, Y., Chen, X., Duan, Y., & Ni, X. (2020). Molding free-space light with guided wave–driven metasurfaces. *Science advances*, *6*(29), eabb4142.

126 Schulz, S. A., Machula, T., Karimi, E., & Boyd, R. W. (2013). Integrated multi vector vortex beam generator. Optics Express, 21(13), 16130-16141.

127 Ding, F., Pors, A., & Bozhevolnyi, S. I. (2017). Gradient metasurfaces: a review of fundamentals and applications. *Reports on Progress in Physics*, *81*(2), 026401.

128 Chen, S., Huang, J., Yin, S., Milosevic, M. M., Pi, H., Yan, J., ... & Fang, X. (2023). Metasurfaces integrated with a single-mode waveguide array for off-chip wavefront shaping. *Optics Express*, *31*(10), 15876-15887.

129 Hsieh, P. Y., Fang, S. L., Lin, Y. S., Huang, W. H., Shieh, J. M., Yu, P., & Chang, Y. C. (2022). Integrated metasurfaces on silicon photonics for emission shaping and holographic projection. *Nanophotonics*, *11*(21), 4687-4695.

130 Yuan, G., Cao, S., Zhang, P., Peng, F., Peng, Z., & Wang, Z. (2019). Achieving wide-range photonics applications based on a compact grating-assisted silicon micro-ring resonator. *Optik*, *183*, 887-896.

131 Pi, H., Rahman, T., Boden, S. A., Ma, T., Yan, J., & Fang, X. (2020). Integrated vortex beam emitter in the THz frequency range: Design and simulation. *APL Photonics*, *5*(7).

132 Pi, H., Yu, W., Yan, J., & Fang, X. (2022). Coherent generation of arbitrary first-order Poincaré sphere beams on an Si chip. *Optics Express*, *30*(5), 7342-7355.

133 Lu, X., Wang, M., Zhou, F., Heuck, M., Zhu, W., Aksyuk, V. A., ... & Srinivasan, K. (2023). Highly-twisted states of light from a high quality factor photonic crystal ring. Nature Communications, 14(1), 1119.

134 P. Miao, Z. Zhang, J. Sun, W. Walasik, S. Longhi, N. M. Litchinitser, L. Feng, Orbital angular momentum microlaser. Science 353, 464–467 (2016).

135 Cai, X., Wang, J., Strain, M. J., Johnson-Morris, B., Zhu, J., Sorel, M., ... & Yu, S. (2012). Integrated compact optical vortex beam emitters. Science, 338(6105), 363-366.

136 Franke-Arnold, S., Barnett, S. M., Yao, E., Leach, J., Courtial, J., & Padgett, M. (2004). Uncertainty principle for angular position and angular momentum. New Journal of Physics, 6(1), 103.

137 Zhang, J., Huang, S. J., Zhu, F. Q., Shao, W., & Chen, M. S. (2017). Dimensional properties of Laguerre–Gaussian vortex beams. Applied optics, 56(12), 3556-3561.

138 Phillips, R. L., & Andrews, L. C. (1983). Spot size and divergence for Laguerre Gaussian beams of any order. *Applied optics*, *22*(5), 643-644.

139 Elsayed, H., & Shaker, A. From Stationary to Mobile: Unleashing the Full Potential of Terrestrial LiDAR through Sensor Integration. Canadian Journal of Remote Sensing, 2023, 49(1), 2285778.

140 Guo, Q., Su, Y., & Hu, T. LiDAR principles, processing and applications in forest ecology. Academic Press, 2023.

141 Wang, R. 3D building modeling using images and LiDAR: A review. International Journal of Image and Data Fusion, 2013, 4(4), 273-292.

142 Li, Y., Zhao, L., Chen, Y., Zhang, N., Fan, H., & Zhang, Z. 3D LiDAR and multi-technology collaboration for preservation of built heritage in China: A review. International Journal of Applied Earth Observation and Geoinformation, 2023, 116, 103156.

143 Li, Y., & Ibanez-Guzman, J. Lidar for autonomous driving: The principles, challenges, and trends for automotive lidar and perception systems. IEEE Signal Processing Magazine, 2020, 37(4), 50-61.

144 Di Stefano, F., Chiappini, S., Gorreja, A., Balestra, M., & Pierdicca, R. Mobile 3D scan LiDAR: a literature review. Geomatics, Natural Hazards and Risk, 2021, 12, 2387 - 2429.

145 Berezhnyy, I. A combined diffraction and geometrical optics approach for lidar overlap function computation. Optics and lasers in Engineering, 2009, 47(7-8), 855-859.

146 Nape, I., Singh, K., Klug, A. et al. Revealing the invariance of vectorial structured light in complex media. Nat. Photon., 2022, 16, 538–546.

147 Yu, W.; Pi, H.; Taylor, M.; Yan, J. Geometric Representation of Vector Vortex Beams: The Total Angular Momentum-Conserving Poincaré Sphere and Its Braid Clusters. Photonics 2023, 10, 1276.

148 Cvijetic, N., Milione, G., Ip, E., & Wang, T. Detecting lateral motion using light's orbital angular momentum. Scientific reports, 2015, 5(1), 15422.

149 Fang, L., Wan, Z., Forbes, A., & Wang, J. Vectorial doppler metrology. Nature Communications, 2021, 12(1), 4186.

150 Fu, S., Guo, C., Liu, G., Li, Y., Yin, H., Li, Z., & Chen, Z. Spin-orbit optical Hall effect. Physical Review Letters, 2019, 123(24), 243904.

151 Lokesh Ahlawat, Kamal Kishor, Ravindra Kumar Sinha, Photonic spin Hall effect-based ultra-sensitive refractive index sensor for haemoglobin sensing applications, Optics & Laser Technology, 2024, Volume 170.

152 Mazanov, M.; Sugic, D.; Alonso, M.A.; Nori, F.; Bliokh, K.Y. Transverse shifts and time delays of spatiotemporal vortex pulses reflected and refracted at a planar interface. Nanophotonics 2022, 11, 737–744.

153 Hosten, O., & Kwiat, P. Observation of the spin Hall effect of light via weak measurements. Science, 2008, 319(5864), 787-790.

154 Bliokh, K. Y., & Bliokh, Y. P. Polarization, transverse shifts, and angular momentum conservation laws in partial reflection and refraction of an electromagnetic wave packet. Physical Review E, 2007, 75(6), 066609.

155 Li, H. Y., Wu, Z. S., Shang, Q. C., Bai, L., & Li, Z. J. Reflection and transmission of Laguerre Gaussian beam from uniaxial anisotropic multilayered media. Chinese Physics B, 2017, 26(3), 034204.

156 Zhen, W., Wang, X. L., Ding, J., & Wang, H. T. Controlling the symmetry of the photonic spin Hall effect by an optical vortex pair. Physical Review A, 2023, 108(2), 023514.

157 Jun Ou, Yuesong Jiang, Jiahua Zhang, and Yuntao He, "Reflection of Laguerre–Gaussian beams carrying orbital angular momentum: a full Taylor expanded solution," J. Opt. Soc. Am. A, 2013, 30, 2561-2571

158 Andrews, D. L., & Babiker, M. (Eds.). The angular momentum of light. Cambridge University Press, 2012.

159 Bliokh, K.Y., & Bliokh, Y.P. Polarization, transverse shifts, and angular momentum conservation laws in partial reflection and refraction of an electromagnetic wave packet. Physical review. E, Statistical, nonlinear, and soft matter physics, 2006, 75 6 Pt 2, 066609.

160 Goodman, J. W. Introduction to Fourier optics. Roberts and Company publishers, 2005.

161 R. Paschotta, article on "Fourier Optics" in the RP Photonics Encyclopedia, retrieved 2024-05-21

162 Zhang, J., Huang, S. J., Zhu, F. Q., Shao, W., & Chen, M. S. Dimensional properties of Laguerre–Gaussian vortex beams. Applied optics, 2017, 56(12), 3556-3561.

163 D. G. Hall. (1996). “Vector-beam solutions of Maxwell’s wave equation,” Opt. Lett. 21, 9–11

164 Enrique J. Galvez, Shreeya Khadka, William H. Schubert, and Sean Nomoto, "Poincaré-beam patterns produced by nonseparable superpositions of Laguerre–Gauss and polarization modes of light," Applied optics, 2012, 51, 2925-2934

165 Fu, S., Gao, C. (2023). Vector Beams and Vectorial Vortex Beams. In: Optical Vortex Beams. Advances in Optics and Optoelectronics. Springer, Singapore. https://doi.org/10.1007/978-981-99-1810-2_7

166 Milione, G., Sztul, H. I., Nolan, D. A., & Alfano, R. R. Higher-order Poincaré sphere, Stokes parameters, and the angular momentum of light. Physical review letters, 2011, 107(5), 053601

167 Filippo Cardano, Ebrahim Karimi, Lorenzo Marrucci, Corrado de Lisio, and Enrico Santamato, Generation and dynamics of optical beams with polarization singularities, Opt. Express, 2013, 21, 8815-8820

168 Carmelo Rosales-Guzmán et al, A review of complex vector light fields and their applications, J. Opt., 2018, 20, 123001

169 R. Paschotta, article on "Brewster's Angle" in the RP Photonics Encyclopedia, retrieved 2024-05-21

170 Wan, C., Shen, Y., Chong, A., & Zhan, Q. (2022). Scalar optical hopfions. eLight, 2(1), 1-7.

171 Zdagkas, A., McDonnell, C., Deng, J., Shen, Y., Li, G., Ellenbogen, T., ... & Zheludev, N. I. (2022). Observation of toroidal pulses of light. Nature Photonics, 16(7), 523-528.

172 Leach, J., Wright, A. J., Götte, J. B., Girkin, J. M., Allen, L., Franke-Arnold, S., ... & Padgett, M. J. (2008). “Aether drag” and moving images. Physical review letters, 100(15), 153902.

173 Villoresi, P., Jennewein, T., Tamburini, F., Aspelmeyer, M., Bonato, C., Ursin, R., ... & Barbieri, C. (2008). Experimental verification of the feasibility of a quantum channel between space and Earth. New Journal of Physics, 10(3), 033038.

174 Ivanov, I. P. (2011). Colliding particles carrying nonzero orbital angular momentum. Physical Review D, 83(9), 093001.

175 Thidé, B., Then, H., Sjöholm, J., Palmer, K., Bergman, J., Carozzi, T. D., ... & Khamitova, R. (2007). Utilization of photon orbital angular momentum in the low-frequency radio domain. Physical review letters, 99(8), 087701.

176 Berkhout, G. C., & Beijersbergen, M. W. (2008). Method for probing the orbital angular momentum of optical vortices in electromagnetic waves from astronomical objects. Physical review letters, 101(10), 100801.

177 S. W. Hancock, S. Zahedpour, A. Goffin, and H. M. Milchberg (2019). Free-space propagation of spatiotemporal optical vortices. Optica 6, 1547-1553

178 Bliokh, K. Y. (2021). Spatiotemporal vortex pulses: angular momenta and spin-orbit interaction. Physical Review Letters, 126(24), 243601.

179 Bliokh, K. Y. (2023). Orbital angular momentum of optical, acoustic, and quantum-mechanical spatiotemporal vortex pulses. Physical Review A, 107(3), L031501.

180 Bliokh, K. Y. (2023). Photon centroids and their subluminal propagation. arXiv preprint arXiv:2306.00490.

181 Hancock, S. W., Zahedpour, S., & Milchberg, H. M. (2021). Mode structure and orbital angular momentum of spatiotemporal optical vortex pulses. Physical Review Letters, 127(19), 193901.

182 Hancock, S. W., Zahedpour, S., Goffin, A., & Milchberg, H. M. (2023). Spatiotemporal torquing of light. arXiv preprint arXiv:2307.01019.

183 Petrov, N.I. (2019). Speed of structured light pulses in free space. Sci Rep 9, 18332.

184 Wan, C., Cao, Q., Chen, J., Chong, A., & Zhan, Q. (2022). Toroidal vortices of light. Nature Photonics, 16(7), 519-522.

185 Cardano, F., & Marrucci, L. (2022). Smoke rings of light. Nature Photonics, 16(7), 476-477.

186 https://wxyhly.github.io/archives/homotopy/

187 Devlin, R. C., Ambrosio, A., Rubin, N. A., Mueller, J. B., & Capasso, F. (2017). Arbitrary spin-to–orbital angular momentum conversion of light. Science, 358(6365), 896-901.

References that have not been cited in this doctoral thesis but are informative to the author

1 Milione, G., Evans, S., Nolan, D. A., & Alfano, R. R. (2012). Higher order Pancharatnam-Berry phase and the angular momentum of light. *Physical Review Letters*, *108*(19), 190401.

2 Fang, L., & Wang, J. (2017). Optical angular momentum derivation and evolution from vector field superposition. Optics Express, 25(19), 23364-23375.

3 Bekshaev, A., Bliokh, K. Y., & Soskin, M. (2011). Internal flows and energy circulation in light beams. *Journal of Optics*, *13*(5), 053001.

4 Yin, X., Zhao, Z., Hao, P., & Li, J. (2023). Spin-orbit interactions of a circularly polarized vortex beam in paraxial propagation. *Optics Express*, *31*(2), 1832-1843.

5 Zhu, J., Chen, Y., Zhang, Y., Cai, X., & Yu, S. (2014). Spin and orbital angular momentum and their conversion in cylindrical vector vortices. *Optics letters*, *39*(15), 4435-4438.

6 Coumbe, D. N. (2018). A note on conformal symmetry. *arXiv preprint arXiv:1808.09800*.

7 Gutiérrez-Vega, J. C. (2020). The field of values of Jones matrices: classification and special cases. *Proceedings of the Royal Society A*, *476*(2242), 20200361.

8 Gutiérrez-Cuevas, R., Wadood, S. A., Vamivakas, A. N., & Alonso, M. A. (2020). Modal Majorana sphere and hidden symmetries of structured-Gaussian beams. *Physical Review Letters*, *125*(12), 123903.

9 Abramochkin, E., & Volostnikov, V. (1993). Spiral-type beams. *Optics Communications*, *102*(3-4), 336-350.

10 Rosales-Guzmán, C., Ndagano, B., & Forbes, A. (2018). A review of complex vector light fields and their applications. *Journal of Optics*, *20*(12), 123001.

11 Moreno, I., Davis, J. A., Ruiz, I., & Cottrell, D. M. (2010). Decomposition of radially and azimuthally polarized beams using a circular-polarization and vortex-sensing diffraction grating. *Optics Express*, *18*(7), 7173-7183.

12 Berry, M. V. (2009). Optical currents. *Journal of Optics A: Pure and Applied Optics*, *11*(9), 094001.

13 Berry, M. V. (1998, August). Paraxial beams of spinning light. In *International conference on singular optics* (Vol. 3487, pp. 6-11). SPIE.

14 Dennis, M. R., & Alonso, M. A. (2017). Swings and roundabouts: optical Poincaré spheres for polarization and Gaussian beams. *Philosophical Transactions of the Royal Society A: Mathematical, Physical and Engineering Sciences*, *375*(2087), 20150441.

15 Esarey, E., Sprangle, P., Pilloff, M., & Krall, J. (1995). Theory and group velocity of ultrashort, tightly focused laser pulses. *JOSA B*, *12*(9), 1695-1703.

16 Landau, L. D., & Lifshitz, E. M. (2013). *Course of theoretical physics*. Elsevier.

17 Weiner, A. M. (2011). Ultrafast optical pulse shaping: A tutorial review. *Optics Communications*, *284*(15), 3669-3692.

18 Zee, A. (2016). *Group theory in a nutshell for physicists* (Vol. 17). Princeton University Press.

19 Griffiths, D. J. (2005). Introduction to electrodynamics.

20 Weston, V. H. (1958). Toroidal wave functions. *Quarterly of Applied Mathematics*, *16*(3), 237-257.